A

Ph.D. Thesis

entitled

Linear and non-linear optical properties of nanoparticles dispersed novel glasses

Submitted in the partial fulfilment for the award of degree of

Doctor of Philosophy (Ph.D.)

by

Shivani
(Reg. no: 901612017)

THAPAR INSTITUTE
OF ENGINEERING & TECHNOLOGY
(Deemed to be University)

under the supervision of

Dr. O.P. Pandey
(Senior Professor)

Thapar Institute of Engineering &
Technology, Patiala

Dr. Gopi Sharma
(Associate Professor)

Kanya Maha Vidyalaya,
Jalandhar

School of Physics and Materials Science

Thapar Institute of Engineering & technology
Patiala (Punjab)-147004

(December, 2019)

Dedicated To My
Loving Family

DECLARATION

I hereby certify that the present work in thesis ***'Linear and non-linear optical properties of nanoparticles dispersed novel glasses'*** in the partial fulfilment of the requirement for the award of the degree of **DOCTOR OF PHILOSOPHY (Ph.D.)** in School of Physics and Materials Science, Thapar Institute of Engineering and Technology, Patiala is an authentic record of my own work carried out under the supervision of **Dr. O.P. Pandey** and **Dr. Gopi Sharma**. The matter embodied in this thesis has not been submitted in part or full to any other institute/university for the award of any degree

Shivani

Shivani

This is to certify that the above statement made by the candidate is true to the best of my knowledge.

Date:

O. P

Dr. O.P. Pandey
(Senior Professor and Head)
School of Physics and Material Science
Thapar Institute of Engineering & Technology
Patiala (Punjab)-147004

Dr. Gopi Sharma
(Associate Professor)
Department of Physics
Kanya Maha Vidyalaya
Jalandhar (Punjab)-144004

Acknowledgements

This thesis has been kept on track and been seen through to completion with the support and encouragement of numerous people including my supervisors, colleagues, friends and various institutions. I have had the great luck to work and collaborate with a lot of inspiring, competent, and nice people who contributed in many ways to the success of this study. It is a pleasant task to use this space to thank them.

At this moment of accomplishment, first of all I am indebted to my supervisors, **Dr. O. P. Pandey** and **Dr. Gopi Sharma**, under whose guidance, I successfully overcame many difficulties and learned a lot. Their understanding, encouragement and personal attention have provided good and smooth basis for my Ph.D. work. I can see the good shape of my thesis because of their help and suggestions in formatting the entire thesis. **Dr. O. P. Pandey** provided decisive and energetic support during the course of my work and clearing the path towards thesis completion in his solution-oriented way. His unflinching courage and conviction will always inspire me, and I hope to continue to work with his noble thoughts. **Dr. Gopi Sharma** steered me through this journey with his invaluable advice, positive criticism, stimulating discussions and consistent encouragement. She took care to shine light of knowledge, when I was groping in the dark of ignorance. If I will stand proud of my achievements then undeniably both are the main creditor. It had been my privilege to be under their tutelage.

The road to my Ph.D started with the financial assistance from Project under **Science and Engineering Research Board (SB/S2/LOP-019/2013)**, Department of Science and Technology, New Delhi.

I owe my humble gratitude and sincere thanks to **Dr. Venu Gopal Achanta**, Department of Condensed Matter Physics, Tata Institute of Research and Technology, Mumbai for his proper and erudite guidance and support. His helpful suggestions and comments has provided precious guidance leading to the completion of research work. I am also thankful to **Dr. Shriganesh S. Prabhu,** Department of Condensed Matter Physics, Tata Institute of Research and Technology, Mumbai for needful help during the various stages of my work. I thank **Mr. Gajendra Mulay, Mr. Nilesh Kulkarni and Mr. Rudheer Bapat** for offering their helping hand in instrumentation during my stay at TIFR, Mumbai.

I am profoundly obliged to **Dr. (Mrs.) Atima Sharma,** Principal, Kanya Maha Vidyalaya, Jalandhar, for his constant encouragement and needful help during the various stages of my work. I am also very thankful to **Mrs. Parminder Kaur Cheema,** Head Department of Physics, Kanya Maha Vidyalaya, Jalandhar for their whole-hearted support and blessings.

It is my privilege to thank **Prof. Prakash Gopalan** (Director) Thapar Institute of Engineering and Technology, Patiala for providing me resources in the institution and needful help during the various stages of my work. I thank my URB Committee members, **Dr. Kulvir Singh, Dr. Soumendu Jana** and **Dr. Haripada Bhunia** for their helpful suggestions and comments during my progress report presentations. All the faculties and staff of SPMS are acknowledged who never turned me down whenever I approached for any help.

I cannot forget the support provided by my senior **Dr. Aayush Gupta,** while compiling the thesis. Though he was busy in his own research work but never says no to me.

Of course one's lab mates are always the basic support structure. It gives me heart felt pleasure in reckoning the contribution of my very good friends and my lab mates **Dr. Rameez Ahamd Mir, Piyush Shrama, Ruby Priya, Damandeep Kaur, Sandeep Kaur, Sanjay Upadhyay** and **Puneet Sharma**. With them I laughed, shared my dreams and unwound my worries. Thanks for standing by me, no matter what may come.

A journey is easier when you travel together. Interdependence is certainly more valuable than independence. Words fail to express my appreciation for my husband **Mr. Naveen Bansal**, for his support and generous care. He was always beside me during the happy and hard moments to push me and motivate me. During the inevitable ups and downs of my life, he often reminded me life's true priorities, which helped me a lot to work for hours tirelessly.

Thank you doesn't seem sufficient for my father-in-law **Mr. Kamal Kumar Bansal** and mother-in-law **Mrs. Aruna Bansal**, but it is said with appreciation and respect to both of them for their support, encouragement, care, understanding and creation of a pleasant atmosphere for me.

Last but not least, I would like to pay high regards to my father (**Mr. Ashwani Kumar)**, mother **(Mrs. Prem Lata)**, my grandmother (**Smt. Leela Devi)** and brother **(Mr. Varun Singla)** for their sincere encouragement and inspiration throughout my research work and lifting me uphill this phase of life. I owe everything to them.

Above all, thanks to the **almighty** beneath the blue sky for bestowing me with his precious blessings!

Shivani

Index

List of Publications

From Ph.D. work:

1. **Shivani Singla,** Venu Gopal Achanta, Om Prakash Pandey, Gopi Sharma, Influence of the size of gold nanoparticles dispersed in glass matrix on optical properties, **Ceramics International** 46, 9907-9912 (2020).
2. **Shivani Singla,** Venu Gopal Achanta, Om Prakash Pandey, Gopi Sharma, Effect of different stabilizers on dispersion of gold nanoparticles in bismuth borosilicate glass and their intensity dependent nonlinear behaviour, **Optical Material** 96, 109334 (2019).
3. **Shivani Singla**, Shriganesh S Prabhu, Om Prakash Pandey, Gopi Sharma**,** Study on the nature of distribution of gold nanoparticles inside the $30Bi_2O_3:70B_2O_3$ glass and its impact on optical behaviour, **Journal of Materials Science: Material in Electronics** 30, 13939–13947 (2019).
4. **Shivani Singla**, Om Prakash Pandey, Gopi Sharma, Z-scan study of nonlinear absorption in gold doped borosilicate glass: effect of Dy^{3+}, **Journal of Non-Crystalline Solids** 521, 119481 (2019).
5. **Shivani Singla**, Venu Gopal Achanta, Nancy Mahendru, Shriganesh S. Prabhu, Mauro Falconieri, Gopi Sharma, High refractive index gold nanoparticle doped Bi_2O_3-B_2O_3 glasses for THz frequencies, **Optical Material** 72, 91–97 (2017).

Other publications:

6. Rameez Ahmad Mir, **Shivani Singla**, Om Prakash Pandey, Hetero carbon structures derived from waste plastics as an efficient electrocatalyst for water splitting and high-performance capacitors, **Physica E: Low-dimensional Systems and Nanostructures** 124, 114284 (2020).
7. **Shivani Singla**, Ruby Priya, Sandeep Kaur , Om Prakash Pandey, Blue light excited novel Eu doped $CaGd_2ZnO_5$ nanophosphors: Structural and photoluminescent properties, **Optik** 216, 164830 (2020).
8. Ruby Priya, Astha Negi, **Shivani Singla**, Om Prakash Pandey, Luminescent studies of Eu doped $ZnAl_2O_4$ spinels synthesized by low-temperature combustion route, **Optik** 204, 164173 (2020).
9. Nancy Mahendru, Govind Parsad Kothiyal, **Shivani Singla**, Mauro Falconier, Gopi Sharma, Photoluminescence and structural characterization of RE doped sodium

alumino scilicate oxyfluoride glass and nano glass-ceramics as a function of γ-irradiation dose, **Physica Status Solidi b**, 256, 1900029 (2019).

10. Neetu Chopra, Sandeep Kaur, Manpreet Kaur, **Shivani Singla**, Ritika Marwaha, Gopi Sharma, and Manmohan Singh Heers, Optical, Physical and Structural Properties of Er^{3+} Doped Low-Phonon Energy Vitreous Matrix: ZnO-B_2O_3-TeO_2, **Physical Status Solidi A**, 215, 1700934 (2018).

List of Conferences

1. **Shivani Singla**, Venu Gopal Achanta, S. Sri Ganesh Parbhu, Om Prakash Pandey, Gopi Sharma, *Gold nanoparticles doped borate glasses for optical devises*, National symposium on nanostructured materials: structure, properties and applications (NSNM-2019) held at KMV college Jalandhar on 22-23 February, 2019.
2. **Shivani Singla**, Venu Gopal Achanta, Om Prakash Pandey, Neetu Chopra, Gopi Sharma, *Z-scan measurement of nonlinear absorption coefficient of Gold nanoparticles doped Bismuth Borosilicate glasses for sensing devices*, International symposium on functional materials: energy and biomedical applications (ISFM-2018) held at Chandigarh on 13-15 April, 2018.
3. **Shivani Singla**, Venu Gopal Achanta, Om Prakash Pandey, Neetu Chopra, Gopi Sharma, *Structural and optical properties of sodium borosilicate glasses containing gold nanoparticles*, National Conference on Emerging Scenario in Basic and Applied Sciences for Sustainable Development 2018 held at DAV college Bathinda on 5 April 2018.
4. **Shivani Singla**, Venu Gopal Achanta, Om Prakash Pandey, Neetu Chopra, Gopi Sharma, *Variation in the properties (structural, optical and thermal) of glass with change in the size of gold nanoparticles embedded in the glass*, National Conference on Material Science Application in Energy & Environment 2018 held at DAV college Jalandhar on 17 March, 2018.
5. **Shivani Singla**, Sandeep Kaur, Neetu Chopra, Venu Gopal Achanta, Gopi Sharma, *Effect of preparation method on the morphology of AuNPs inside* $30Bi_2O_3:70B_2O_3$ *glass*, International Conference on Advances in Glass Science and Technology 2017 held at CGCRI Kolkata on 23-25 January, 2017.
6. **Shivani Singla**, Venu Gopal Achanta, Gopi Sharma, *Optical Characterization of Au Nanoparticles Doped Bismuth Borate Glass*, National Conference on Functional Glasses/ Glass-Ceramics and Ceramics held at VNIT Nagpur on 10-12 December, 2016.

List of Figures

Chapter-1

Chapter- 3

Chapter- 4

Chapter- 5

Chapter- 6

Chapter- 7

List of Tables

Chapter-6

Chapter-7

Chapter-8

Preface

Constant efforts are being made by the researchers to develop a suitable and efficient material to be used for optical applications. Composite materials formed by the incorporation of metal nanoparticles in glass are the most preferred as they exhibit striking third order nonlinearity and ultrafast time response. Moreover, remarkable modification in optical behavior can be achieved by controlling amount, size and shape of the nanoparticles. In addition to this, the local environment around the nanoparticles plays a crucial role which is an intrinsic function of glass composition. In most of the traditional methods, used for the production of such nanocomposites, metallic salts are first introduced in the glass matrix and get transformed to nanoparticles as a result of pulsed laser beam exposure or heat treatment. This post treatment eventually induces crystallization of glass with associated scattering of light and hence, resulting in reduced optical quality of material. In the present work, direct incorporation of metallic nanoparticles in the glass matrix has been studied in detail which could be an effective solution for above-mentioned limitations. The entire work is organized in following eight chapters:

Chapter 1 gives a brief description and background of basic phenomena leading to the origin of ultrafast nonlinear response in glass nanocomposites (GNCs). Various fabrication routs followed to prepare such GNCs are discussed along with their real-time limitation to summarize the importance and need of direct incorporation of metallic nanoparticles. Moreover, the basic structure of borate glasses along with their features leading to enhanced nonlinear behavior is discussed in detail. Further, the motive behind using the gold nanoparticles (AuNPs) as filler in the GNCs is given in detail. In the last, importance of rare earth to stabilize metal nanoparticles (AuNPs) with enhanced optical efficiency is discussed.

Chapter 2 summarizes the available literature concerning to nonlinear optical behavior of glass and glass nanocomposites. Influence of fabrication route, type of metal nanoparticle and the glass composition on optical behavior is compared for different glass systems. Enhanced luminescence in vicinity of rare earth is also presented here. Large value of figure of merit, fast response time and high nonlinear susceptibility of glasses makes them promising candidates for opto-electronic devices. Based on literature, the last section of this chapter reviews the gaps in study so far along with the proposed objectives of the thesis.

Chapter 3 describes the details of experimental procedure followed to achieve the proposed objectives. The detailed methodology adopted for the preparation of AuNPs dispersed GNCs via direct incorporation of as prepared nanoparticles is given in this chapter. Also, adopted characterization techniques such as X-ray diffraction (XRD), Fourier transform infrared (FTIR) spectroscopy, Field emission scanning electron microscopy (FESEM), High resolution transmission electron microscopy (HRTEM), Differential thermal analysis (DTA), Density measurements, UV-Vis spectroscopy and Z-scan for structural, morphological, thermal and optical properties, respectively have been discussed briefly.

Chapter 4 deals with the optimization of fabrication methods to achieve a homogeneous distribution of AuNPs in the glass matrix through direct incorporation. For this purpose, AuNPs dispersed glasses are prepared via three different methods; (i) drop casting method, (ii) sandwich method and (iii) melt quenching at room temperature. XRD confirms the amorphous nature of glass even after the addition of AuNPs whereas basic structure of glass is composed of BO_3 and BO_4 units as illustrated from FTIR. FESEM micrographs reveals that the morphology of AuNPs inside the glass is highly dependent on the method of their incorporation. It is also depicted that melt quenching at room temperature method results in uniform distribution of AuNPs and hence used for further sample preparation. Uniform dispersion of AuNPs in glass matrix resulted a high refractive index and large nonlinear optical properties which makes them interesting for plasmonic devices.

Chapter 5 focuses on the effect of size and amount of AuNPs along with glass composition on various properties. This chapter is divided into three subsections; (i) the effect of amount of AuNPs, (ii) effect of size of AuNPs, and (iii) effect of variation of Bi-content in the glass. Glasses remains amorphous with variation in any of the above mentioned parameter. FTIR confirms the formation of non-bridging oxygens with the inclusion of AuNPs and increase in bismuth content inside the glass. FESEM results revealed the loss of AuNPs due to evaporation and coagulation. Shielding effect of bonds by nanoparticles results in modification in thermal parameters as observed from DTA results. Increase in bismuth content reduces the glass transition temperature that results in enhanced coagulation. Nonlinear behavior increases with increase in amount of gold and bismuth in the glass whereas it saturates for 40 nm as average particle size.

Chapter 6 provides an effective solution to reduce the loss of nanoparticles via evaporation and oxidation occurring during melting because of the high temperature step involved in their preparation. The use of refectory material (SiO_2) helps in preventing the loss of AuNPs. Here, the higher concentration of AuNPs as a result of the protection from oxidation at high temperature is evidenced from the observed FESEM micrographs along with compromised agglomeration of AuNPs in order to reduce the surface stresses (Ostwald ripening). Moreover, the reduction in glass transition temperature also supported the coagulation of AuNPs. Prepared SiO_2 contained GNC samples possess sufficiently high nonlinear refractive index and low absorption as observed from Z-scan.

Chapter 7 presents the comparison of stabilizing action of Eu_2O_3, EuF_3 and KSCN on AuNPs. The systematic investigation of glasses containing these stabilizing agents for the optical, structural, thermal and nonlinear optical properties of the synthesized samples has been done. Eu_2O_3 acting as capping agent on AuNPs seems to be the best stabilizing substance among these three as a result of reduced coagulation of AuNPs as observed in FESEM and HRTEM micrographs. Addition of EuF_3 and KSCN could not prevent sufficient coagulation and thermal loss of AuNPs, respectively. The nonlinear refractive index is found to be very high for the prepared glass system.

Chapter 8 describes the conclusion drawn from above studies and scope for future work. It gives the comparative structural and thermal characteristics of AuNPs dispersed borate glass samples. The influence of fabrication conditions, AuNPs (amount and size), matrix composition and stabilizing agent on the optical efficiency is compared. Based on the observed results, mono-dispersed (~40 nm) AuNPs in amorphous matrix with high thermal stability and better nonlinear response enables the borate glasses a suitable candidate for fiber drawing, optical switching and optical limiting applications. At the end, possible future scope to enrich the study is presented.

CHAPTER 1 INTRODUCTION

Overview

The requirement of faster and efficient opto-electronic devices has led to design the platform for functional materials. In this category, materials exhibiting nonlinear optical property and ultrafast time response are more suitable for designing variety of opto-electronic components. In the race of efficiency and ultrafast response, glasses containing nanoparticles are a step ahead because of their exceptional properties as compared to other composite materials. Further these properties are intrinsic function of fabrication route and materials used for fabrication of glasses. Moreover, the distribution of nanoparticles in glassy matrix influence the non-linear characteristic to greater extent. Several investigations are being carried out to produce efficient materials but still control on distribution, size, stability and morphology of nanoparticles inside the glass is an unsolved issue.

In the present chapter a brief discussion on nonlinear behaviour and the issues faced to commercialize the glass with an appropriate solution which include the effect of fabrication route, choice of suitable nanoparticle and composition is given. In addition, the role of rare earths to stabilize the nanoparticles is also illustrated in brief.

1.1. Motivation

A significant development in scientific technology and industry in last few decades demands for efficient and faster electronic components. The requirement of faster components possibly can be fulfilled by the replacement of electronic with opto-electronic components such as optical switches, sensors, actuators, transducers, amplifiers etc. Nonlinear optical (NLO) response of material first observed by Frankel *et al.* in 1961 is the key property for these opto-electronic components [1]. Material with large third order nonlinear (TON) susceptibility ($\chi^{(3)}$) are being investigated not to only have better understating of fundamentals of light matter interaction but also adds new functionalities to the material that carries importance from application point of view. Refractive index tuning and light controlled phase in a material can be achieved with TON behaviour of the material that is helpful in realization of future applications in real time holography, optical computing, phase coagulators and optical correlators [2,3].

Form practical application point of view, larger 'figure of merit' (F) for TON is desired and is given by [4]:

$$F = n_2/2\beta\lambda, \tag{1.1}$$

where n_2 is nonlinear refractive index, β is coefficient of nonlinear absorption and λ is wavelength. A material with combination of relatively large n_2, small β and low propagation losses are highly desirable.

The challenge in development of NLO material is simultaneous control on primarily NLO behaviour i.e. NLO susceptibilities or coefficients. Secondly on optical clarity, stability, fabrication, process ability etc. is equally important. This practise requires the knowledge of fundamentals of nonlinearity, impact of structural and morphological changes on the optical properties.

1.2. Brief introduction to nonlinear optics

Interaction of light with matter results in nonlinear response that could not be observed normally because of moderate electric field of ordinary light sources and weak nonlinear susceptibility of matter. Invention of laser, facilitated with high light intensities that further supported the investigation of impact of structure on nonlinear optical behaviour in several time regime, specifically in femtosecond and attosecond regimes [5]. Fundamentally, the experimental conditions that are challenging to achieve by any other means, can easily be attained in existence of NLO response of the material.

Polarization quantifies the light matter interaction. External electric field (**E**) of light induces polarization inside the matter that can be represented as:

$$\mathbf{P} = \varepsilon_o(\chi^{(1)}\mathbf{E} + \chi^{(2)}\mathbf{E}^2 + \chi^{(3)}\mathbf{E}^3 \ldots\ldots\ldots) \qquad (1.2)$$

where, ε_o is electrical permittivity in vacuum (8.86×10^{-12} As/Vm) and $\chi^{(1)}$, $\chi^{(2)}$, $\chi^{(3)}$ are first, second and third order susceptibilities, respectively. The linear optical properties (dispersion, refraction, absorption etc.) are determined by the first term whereas the higher terms are responsible for the nonlinear effects. A set of nonlinear equations are obtained after substituting the Eq. (1.2) in Maxwell's equations that contains higher power terms of wave field strength. The higher terms results in several wave mixing phenomenon. More specifically, the radiations re-emitted by the dipole contains different frequency terms from the original that results in several effects collectively known as nonlinear effects.

Mainly, quadratic and cubic terms of polarization gives rise to interesting NLO effects. Wave mixing, electro-optic modulation, second harmonic generation etc. effects arises from quadratic term ($\chi^{(2)}$) while third harmonic generation, phase conjugation, enhanced Raman scattering and optical bistability arise in response of cubic term ($\chi^{(3)}$). Moreover, odd ordered terms ($\chi^{(1)}$ and $\chi^{(3)}$) are nonzero in centrosymmetric media (material with inversion symmetry) while the even term ($\chi^{(2)}$) are zero. Gases, liquids and amorphous solids falls into this category where $\chi^{(3)}$ is the lowest nonlinear term present. As the refractive index and polarization are related terms, TON can be intended in terms of change in refractive index and absorption as follows:

$$n(I) = n_o + n_2 I \qquad (1.3)$$

$$\alpha(I) = \alpha_o + \alpha_2 I \qquad (1.4)$$

where n_o is linear index of refraction, α_o is linear absorption coefficient and I is light intensity. n_2 and α_2 are nonlinear refractive index and nonlinear coefficient of absorption that are related to real and imaginary part of $\chi^{(3)}$, respectively according to the relation [6]:

$$n_2 = \frac{3}{4\epsilon_o n_o^2 c} Re\chi^{(3)} \qquad (1.5)$$

$$a_2 = \frac{3\omega}{2\epsilon_o n_o^2 c^2} Im\chi^{(3)} \qquad (1.6)$$

TON ($\chi^{(3)}$) can be estimated with the help of several theoretical models available in literature [7,8].

Many materials (polymer composites, single crystals etc.) have been fabricated and characterised for large nonlinearity so as to be implemented for various optical applications. However, the main motive for real application is to produce stable material with high and ultra-fast nonlinear response. Glass being centrosymmetric, containing metal nanoparticles could be a good candidate for this.

1.3. Glasses and its composites: materials for TON

Glass is a super cooled liquid without any regular structure. Glasses are materials of considerable interest because of their unique properties like hardness, good tensile strength, optical transparency and excellent stability towards corrosion [9–12]. Limited nonlinear response of glasses restricts its applications in optoelectronic devices. Whereas their efficiency can be enhanced by making glass composite after adding suitable filler having dimensions less than 100 nm [13–15].

Roman were the first to show interest and study the properties of metallic nanoparticles incorporated in glass. Although, the lack of knowledge of surface science, the application of these colourful metallic particles was restricted to use them as colorants for glass window in Cathedrals, to colour ornaments, aesthetic items, enamel pottery and ceramic etc. In 400AD, accidentally a complex optical effect was observed in ‘Lycurgus Cup’ known as dichorism [16]. Because of dichorism, this cup manufactured from Soda lime glass containing minimal amount of gold and silver nanoparticles shows change in colour as a function of position of light. Opaque green and ruby red colour are seen in reflected and transmitted light, respectively. After investigation, it is concluded that the presence of small nanocrystals is the only reason behind this phenomena [16,17]. Modern characterization techniques like transmission electron microscopy scanning electron microscopy etc. have helped in understanding the behaviour of such materials and further motivated their development that have become an emerging area of research these days.

The incredible properties of glass over other dielectrics like chemical stability, high durability, low cost fabrication in any shape, high transparency, ability to modify several properties by simply changing the basic composition etc. make them as the best encapsulating host matrix to be used. Addition of small number of metallic nanoparticles drastically modify the properties of traditional glass and a new class of material called glass nanocomposites

(GNCs) comes into picture. Such metal GNCs finds applications in solid state lasers, memory devices, optical switches, sensors and wave guides [14,18–20].

1.4. Properties of GNCs

Existence of the following properties put the GNCs a step forward in the race of NLO materials.

(i) Surface plasmon resonances: Surface plasmon resonance (SPR) is well known unusual optical property possessed by materials in nano range. Interestingly, when the size reduction below electron mean free path is achieved, an intense absorption in near UV region is observed. This is a result of coherent oscillations of conduction band electrons that takes place when the electromagnetic field of incident light interacts with the nanomaterials. These oscillations lead to the formation of electron cloud which is responsible for the phenomena known as SPR [21,22]. Systematic representation of phenomena of generation of SPR for a spherical particle is displayed in Fig. 1.1. The position of SPR band is an intricate function of host material, shape, size, surrounding environment and morphology of the nanoparticles [23,24]. In addition, large and localised electric field is produced around the metal nanoparticles inside a dielectric medium that leads to various interesting phenomena like non-linear optical behaviour, surface enhanced Raman scattering and many more.

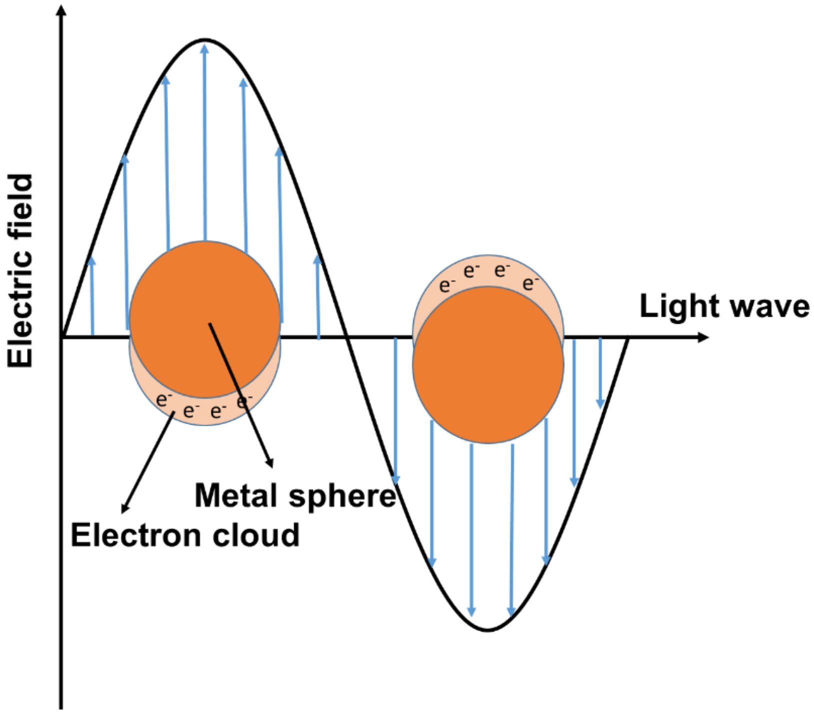

Figure 1.1: Systematic representation of surface plasmon resonances in spherical metallic nanoparticle.

(ii) Ultrafast time response: Ultrafast nonlinear response of glass composites containing nanoparticles (2-30nm) as compared to other materials attracts many researchers for their application in several emerging fields of optics. Among enormous fabricated materials glass nanocomposites are reported to have shortest time response of several pico- to femto-seconds. The time response is shorter than the commercially used laser pulse durations and make them an appropriate material to be used for many nonlinear applications as reported by Vogel [25].

The nonlinear optical properties of GNCs are a function of (i) fabrication route chosen, (ii) size, shape, material and distribution of metal nanoparticles and (iii) type of host material. GNCs facilitates to tune the NLO property by simply choosing the appropriate condition.

1.5. Fabrication of GNCs

It is a well-studied and well known fact that the properties like optical, structural and electrical of any material are highly dependent on the route of fabrication. Same is the case with glass nanocomposites. From the last few decades, the advancement in science and technology has led to development of, several different methods to incorporate/produce metallic nanoparticles inside the vitreous material. Brief details of the method along with its merits and demerits is discussed below.

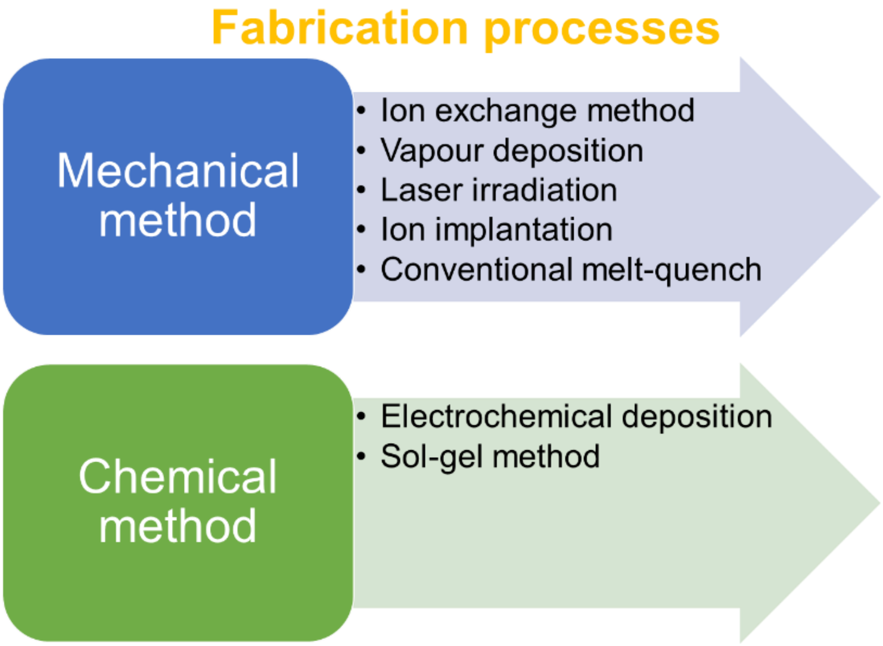

Figure 1.2: Chart of fabrication methods used effectively.

Almeida *et al.* in 2012 [26] have successfully generated copper nanoparticles inside the glassy matrix using a **femtosecond laser** operating at a repetition rate of 1 kHz, followed by subsequent heat treatment. Despite of providing the control over three dimensional arrangement of metallic nanoparticles inside the dielectric this technique also leads to crystallization in the glass. These crystals act as scattering centres when such materials are used for optical applications. Also the presence of crystals reduces the response time. Irradiation of high intensity often damages the glass.

In the same year, Simo *et al.* [27] produced the silver nanoparticles inside soda-lime silicate glass using **ions exchange method** which is suitable in various facets. Especially, (i) introduction of efficiently high concentration of metallic ions, (ii) undamaged glass matrix (as damaging of the material is observed after long exposure of femtosecond laser), (iii) separation between ion-insertion and growth process and (iv) easy up scaling assists the mass production.

Rozra *et al.* in 2013 [28] used **vapour deposition** which comes out to be a favourable technique for synthesising nanocomposite under a dry conditions. Moreover, the relatively easiness of operation, less requirements for the sample fabrication, comparatively higher production levels of material and facility of automatic operation make it more efficient to use.

Sm^{3+} doped glass B_2O_3–PbO–Bi_2O_3–GeO_2 embedded with gold nanoparticles is synthesised by Herrera *et al.* in 2016 [29] using Au^+ **ions implantation** followed by annealing below the glass transition temperature. Crystallization of a very thin layer of glass along with the generation of metallic gold nanoparticles in the Sm-doped glass at the implanted surface takes place.

However, in the methods mentioned above (ion exchange, physical vapour deposition and ion implantation), the produced nanoparticles lies just near the surface of the substrate only i.e. within the range of few micrometres and not in the bulk which reduces their optical efficiency. Apart from this, the necessary equipment required to carry out the vapour depositions and ion implantation are expensive.

Whereas **sol-gel method** is found to be promising one. Huang *et al.* [30] studied the sodium borosilicate glass codoped with gold and nickel nanoparticles fabricated through sol-gel route. Higher purity, processing at lower temperature and potentially higher homogeneity are few merits that attract glass scientists. Although inability of this procedure to provide the control over the nanoparticle distribution inside the glass is its main demerit.

Among the above mentioned methods, the **conventional melt quench technique** to synthesise glasses followed by subsequent heat treatment is widely used [31–33]. Metallic salts are used as a precursor for the formation of nanoparticles in the glass having at least one component that could reduce itself. In the reducing environment, the metallic ions gets reduced to atoms and finally coagulates to form nanoparticles. Whereas this method requires lots of labour and time. Also, the heat treatment generates several defects in the matrix that reduces the optical efficiency and response time of the glass. Therefore, the requirement of a new technique to have non-defective distribution of nano particles method is highly required.

One of the solution to the above problems is the direct incorporation of ready-made metallic nanoparticles while preparing the glass using melt quench technique. Using ready-made nanoparticles will not require the heat treatment step in reducing environment. In addition this method is highly economical, requires less efforts, no specific equipment and is easy to handle. The issue faced with this method is low concentration of nanoparticles because of vaporisation and low solubility that can be easily resolved by selecting the appropriate host composition and suitable metal nanoparticles.

1.6. Selection of host matrix

Among chalcogenide, halide and oxide glasses which are considered suitable for optical applications, oxide glasses are most commonly used. Oxide glasses are promising host materials to examine the effect of chemical environment on optical, thermal, chemical and mechanical properties because of their excellent flexibility of size and shape. In several studies the improvement in optical properties have been reported by varying the chemical composition of host matrix [34–36]. In addition to this, the modification in glass matrix by varying the constituents has led to many fold increment in properties to make them suitable for opto-electronics as fibres, amplifiers, filters, memories and so forth [37–41]. Borate glasses seek more attention among various oxide glasses due to relatively low two photon absorption that makes these glasses active candidate for optical switching devices. Linear and nonlinear parameters of different oxide glasses are given in Table 1.1.

The glassy systems with rich B_2O_3 content are known as borates that shows high tendency of glass formation. Even at slowest cooling rate, borates have least tendency to crystallize. Structure and arrangement of atoms controls the properties of any substance. Therefore the basic understanding of structure to have insight of the behaviour of material is highly required.

Table 1.1: Linear and nonlinear refractive index (n_2), nonlinear absorption coefficient (β) and wavelength (λ) along with reference for different oxide glasses.

Glass	**Linear index**	**n_2 (m^2/W)**	**β (m/W)**	**λ (nm)**	**Reference**
Silicate					
SiO_2	-	2.2×10^{-20}	$<0.01 \times 10^{-14}$	800	[42]
$60Bi_2O_3$–$30B_2O_3$–$10SiO_2$	-	4.8×10^{-18}	2.4×10^{-11}	800	[43]
ZBS0	2.23	4.7×10^{-18}	1.78×10^{-11}	532	[44]
NBS	-	1.67×10^{-16}	7.02×10^{-11}	800	[45]
BK–10	-	1.7×10^{-20}	0.55×10^{-17}	355	[46]
Tellurite					
TeO_2-BaO	2.1	2.8×10^{-19}	$<0.1 \times 10^{-14}$	810	[47]
TeO_2-Nb_2O_5	2.1	2.7×10^{-19}	$<0.1 \times 10^{-14}$	810	[47]
TeO_2-ZnO-Na_2O-PBO	2.1	1.4×10^{-19}	$<0.1 \times 10^{-14}$	810	[47]
BBT3	2.21	8.8×10^{-18}	–	800	[48]
TeO_2–ZnO–Na_2O	1.99	1.9×10^{-19}	$<0.1 \times 10^{-14}$	800	[49]
TeO_2–ZnO–Na_2O-BaO	1.96	1.5×10^{-19}	$<0.1 \times 10^{-14}$	800	[49]
Germinate					
GB	-	1.7×10^{-19}	0.09×10^{-14}	580	[50]
PGO	-	10×10^{-17}	$<60 \times 10^{-14}$	800	[51]
Borate					
NB-0	1.62	1.32×10^{-17}	13.5×10^{-12}	800	[52]
BZH7	-	1.3×10^{-19}	$<0.01 \times 10^{-14}$	800	[53]
BZH2	-	2.9×10^{-19}	$<0.01 \times 10^{-14}$	800	[53]
$Li_2B_4O_7$	-	4.7×10^{-10}	–	532	[54]
BBW0	2.03	0.78×10^{-18}	0.34×10^{-14}	780	[55]
10BaO-40ZnO-$50B_2O_3$	1.32	0.11×10^{-20}	0.57×10^{-14}	532	[56]
10CaO–$35Bi_2O_3$–$55B_2O_3$	-	1.6×10^{-16}	-	532	[57]

Fig. 1.3 displays the two dimensional vitreous structure of B_2O_3 glass. All borate glasses contains random network of corner linked BO_3 trigonal units, though in crystalline compound, boron exists in both triangular and trigonal units. The oxygen atoms that are shared between two trigonal units are bridging oxygens (BO) while those not shared are non-bridging oxygens (NBOs). From X-ray and neutron diffraction studies, it is observed experimentally that the average B-O bond length is 1.38 Å and the B-O-B bond angle is 131 Å in a trigonal unit. This broader bond angle does not allow the existence of long range order. Also it is evidenced from the Raman spectra that, boroxol rings that contain 3 BO_3 units arranged in hexagonal manner is the major constituent of vitreous structure. According to very recent studies, fraction of boron

present in the boroxol ring is 0.75 that precisely depend on the sample preparation and thermal history [58].

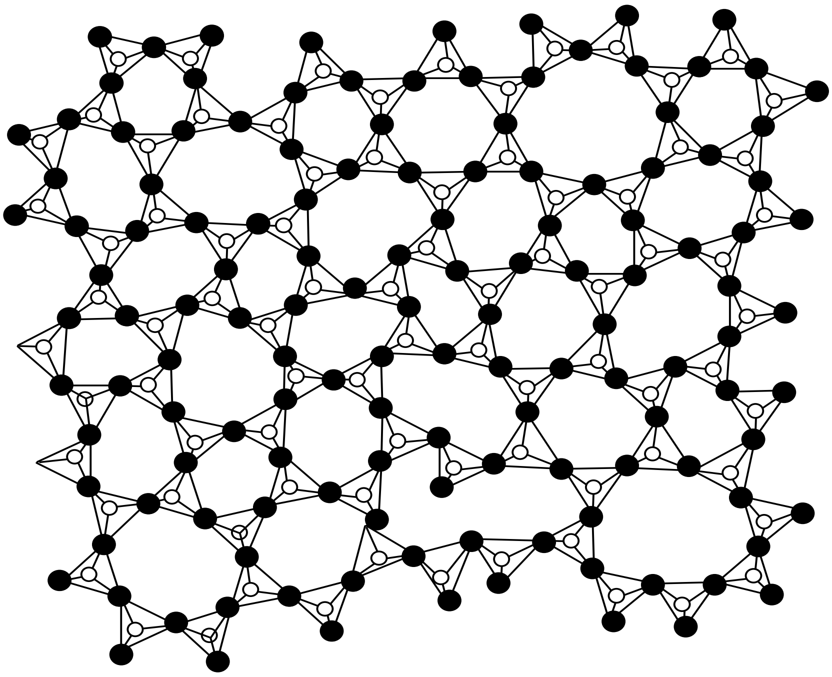

Figure 1.3: Vitreous structure of borate. Here empty sphere represents the boron atom where the solid sphere represents the oxygen atoms linked with boron [59].

In presence of a modifier, either NBO are formed as shown in (i) or these 3-coordination state of B in trigonal BO_3 units (B_3) gets transformed to 4-coordination state in tetrahedral BO_4 units (B_4) as shown in (ii).

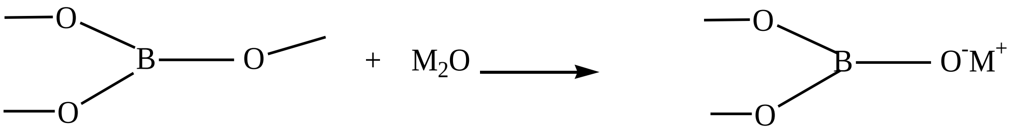

(1.7)

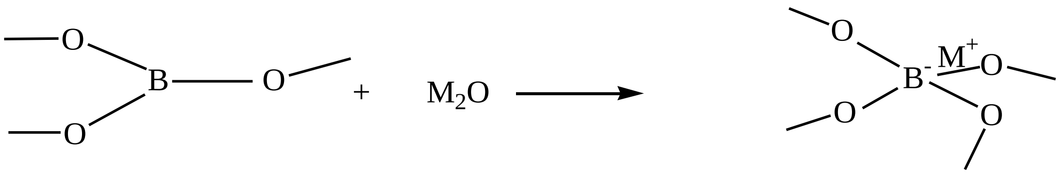

(1.8)

Since the octet of B is not complete in BO_3 unit, however, in the presence of oxide ion it can accept 2 e^-s to form BO_4^- tetrahedral unit in which all the oxygen atoms remain bridging. The addition of alkali oxide as a modifier changes the several properties of the glass until a critical concentration of tetrahedral coordinated boron is reached. Beyond this concentration, the reversal in the property trend is observed. This phenomena is known as boron anomaly and is not observed in silicate glasses. Krogh-moe [60,61] proposed the existence of different type of borate species (shown in Fig 1.4) in borate glass. The presence of these species influences the property trends.

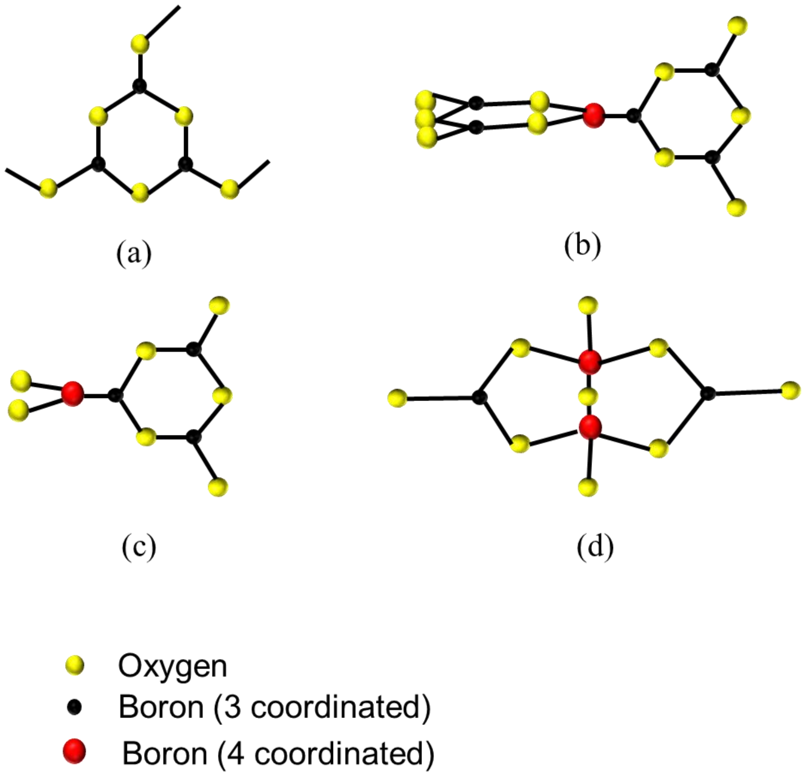

Figure 1.4: Different structural units of borates proposed by Krogh.

Borates have remarkably high melting temperature and this high temperature can modify the properties of nanoparticles while fabrication. Addition of Bi_2O_3 can reduce the melting point, average phonon energy and improves the chemical durability and rare earth solubility. The high polarizability of bismuth oxide make these glasses highly suitable as efficient for thermal and mechanical sensors, superconducting materials and high refractive index materials [44,62]. Furthermore, these glasses are reported to have large TON in visible to near infrared wavelength regions [63].

Reduction in size of the metal to the nanometre range also affects its physical properties like melting point [64]. The production of glass takes place at very high temperatures during which the metallic NPs could get evaporated. In order to tackle with the problem of evaporation of nanoparticles while fabricating the glass, SiO_2 is used as a refractory material that protects the nanoparticles from high temperature [65]. In addition to this they add new functionalities to glass. Lastly, the choice of nanoparticles that could withstand in above mentioned conditions is equally important.

1.7. Gold and rare earth element(s) nanoparticles as a filler material

Recently, metal nanoparticles have attracted considerable research interest among huge class of nanomaterials due to their unique optical properties. In particular, Au, Ag and Cu nanoparticles have been mostly studied due to the existence of an intense and well-defined surface plasmon resonance in the visible region [66–68]. Although many properties and applications of Ag and Au nanoparticles are very alike, but Ag nanoparticles doped materials have been studied extensively as compared to Au because of its lower cost. Gold nanoparticles (AuNPs) exhibit lower electronegativity (1.8) as compared to silver (1.9) and copper (1.9), enhanced luminescent behaviour in NIR region of spectrum and the ability to show higher order nonlinear susceptibility that make them practically of more importance that require detailed study [69,70]. Last but not the least, the faster time response of the order of femtosecond makes the materials containing gold highly suitable for ultrafast optical applications [71]. Table 1.2. provides the comparison of several optical properties of different nanoparticles.

Table 1.2: Several nanoparticles, along with their system, $\chi^{(3)}$ values, response time at mentioned wavelength and the references.

Nanoparticle	**System**	**$\chi^{(3)}$ (esu)**	**Response time (ps)**	**λ (nm)**	**References**
Au(15nm)	Silica	10^{-9}	1.5-1.8	550	[72]
Cu(2nm)	Al_2O_3	10^{-7}	5-450	600	[73]
Ag(3nm)	Glass	10^{-10}	2	774	[74]
CdSSe	SiO_2	10^{-9}	25	532	[75]
SnO_2(10nm)	Silica	10^{-12}	-	1064	[76]

For the direct incorporation of metal nanoparticle, Au nanoparticles seems to be highly suitable because of its high melting temperature and inert nature among the three metals. For the direct incorporation of ready-made metallic nanoparticles while fabricating the glass using conventional melt quench technique, the metallic nanoparticles are mixed along with all the raw components of the glass and then placed in the furnace kept at appropriate temperature range for melting. While melting the glass, nanoparticles also undergo high heat step along with the other precursors that would result into melting or evaporation of the nanoparticles. The high melting point of gold helps to get an escape from high heat and remains in the glass itself. Another reason is the ability of AuNPs to couple with rare earth elements inside the glass that results into enhanced luminescence effects [77]. Most of the commercial lasers are being operated in NIR region. Silver and copper based materials have been studied extensively, whereas the introduction of AuNPs enhances the nonlinearity in NIR region which is the requirement of the hour.

From the above discussion, the motive behind using the AuNPs as filler in the glass nanocomposite is clear. But still several challenges (Ostwald's repining, evaporation etc.) are faced while incorporation nanoparticles in glass. Following discussed solution could be the best way to overcome these challenges.

Ostwald ripening is the phenomena in which the smaller metallic nanoparticles combine to form bigger ones in order to overcome the extra stresses on the surface and leads to loss of their identity [27]. Use of suitable stabilizer is will help to overcome this difficulty. Rare earths and negatively charged species that could form a covering around the nanoparticles protect them from coagulation [32]. Inclusion of metal nanoparticles along with lanthanides in the glass matrix is interesting as they are found to improve the linear and nonlinear optical behaviour of glasses [78–80]. Local electric fields produced by the energy transfer between rare earth (RE) and metallic nanoparticles in turn act on RE atoms and modify the luminescent properties [24,81]. As the localized surface plasmon resonance (LSPR) of nanoparticles depend on the host material, size, shape and morphology of metal nanoparticles, the luminescent properties can be modulated by LSPR mediation [14,82,83].

The development of new method that are comparatively reliable and economical for the incorporation of metallic nanoparticles are required. The main focus of present study is the direct incorporation of metallic nanoparticle without any heat treatment in order to enhance the efficiency of the material. Step by step efforts are made to address the problem of fabrication, appropriate concentration of nano particles, selection of size, evaporation and coagulation of nanoparticles has been resolved. Considerable efforts have been made to understand and improve the nonlinear behaviour of the material.

References:

1 P. A. Franken, A. E. Hill, C. Peters, G. Weinreich and Yeil, *Phys. Rev.*, 1961, **7**, 118–120.

2 Y. R. Shen, The Principles od Nonlinear Optics, *Wiley*, New York, 1984.

3 H. B. Liao, R. F. Xiao, H. Wang, K. S. Wong, G. K. L. Wong, H. B. Liao, R. F. Xiao, H. Wang, K. S. Wong and G. K. L. Wong, *Appl. Phys. Lett.*, 2012, **1817**, 1–4.

4 K. Tanaka, in *Springer Handbook of Electronic and Photonic Materials*, eds. S. Kasap and P. Capper, Springer International Publishing, Cham, 2017, p. 1.

5 A. H. Zewail, *Angew. Chemie - Int. Ed.*, 2000, **39**, 2586–2631.

6 Y. Asahara, *Ceram. Int.*, 1997, **23**, 375–382.

7 R. W. Boyd, Nonlinear Optics, *Acad. Press*, 2003.

8 M.G. Kuzyk, C.W. Dirk, Characterization Techniques and Tabulations for Organic Nonlinear Materials, *Markel Dekker*, 1998, 655–692.

9 S. Soo, *Mater. Res. Bull.*, 2014, **51**, 336–344.

10 S. Sindhu, S. Sanghi, A. Agarwal, V. P. Seth and N. Kishore, *Mater. Chem. Phys.*, 2005, **90**, 83–89.

11 K. Singh, H. Singh, G. Sharma, L. Gerward, A. Khanna, R. Kumar, R. Nathuram and H. Singh, *Radiat. Phys. Chem.*, 2005, **72**, 225–228.

12 M. Peng, D. Chen, J. Qiu, X. Jiang and C. Zhu, *Opt. Mater. (Amst).*, 2007, **29**, 556–561.

13 Y. Teng, B. Qian, N. Jiang, Y. Liu, F. Luo, S. Ye, J. Zhou, B. Zhu, H. Zeng and J. Qiu, *Chem. Phys. Lett.*, 2010, **485**, 91–94.

14 C. B. De Araujo, D. Silvério, T. Alexandre, A. De Assumpção, L. Reyes, P. Kassab and D. Mariano, *Sci. World J.*, 2013, **385193**, 1–13.

15 A. M. Noorazlan, H. M. Kamari, S. O. Baki and D. W. Mohamad, *J. Nanomater.*, 2015, **952308**, 1–9.

16 Kharisov BI, Kharissova OV, Ortiz-Mendez U. *Handbook of less-common nanostructures*. Boca Raton, FL: CRC Press 2012; pp. 862.

17 I. Freestone, N. Meeks, M. Sax and C. Higgitt, *Gold Bull.*, 2007, **40**, 270–277.

18 G. M. Herrera, A. C. Padilla and S. P. Hernandez-rivera, *Nanomaterials*, 2013, **3**, 158–172.

19 G. Schmid and B. Corain, *Eur. J. Inorg. Chem.*, 2003, **2003**, 3081–3098.

20 Y. Watanabe, G. Namikawa, T. Onuki, K. Nishio and T. Tsuchiya, *Appl. Phys. Lett.*, 2001, **78**, 2125–2127.

21 G. L. Nealon, B. Donnio, R. Greget and J. Kappler, *Nanoscale*, 2012, **4**, 5244–5258.

22 R. C. Fernández-Hernández, R. Gleason-Villagran, C. Torres-Torres, L. Rodríguez-Fernández, A. Crespo-Sosa, J. C. Cheang-Wong, A. López-Suárez, R. Rangel-Rojo, A. Oliver and J. A. Reyes-Esqueda, *J. Opt. (United Kingdom)*, 2012, **14**, 125203.

23 B. Karmakar, T. Som, S. P. Singh and M. Nath, *Trans. Indian Ceram. Soc.*, 2010, **69**, 171–186.

24 L. Reyes, P. Kassab, M. Eiji, C. Taveira, D. Mariano and J. Roberto, *Opt. Mater. (Amst).*, 2011, **33**, 1948–1951.

25 E. M. Vogel, *J. Am. Ceram. Soc.*, 1989, **72**, 719–724.

26 J. M. P. Almeida, L. De Boni, W. Avansi, C. Ribeiro, E. Longo, A. C. Hernandes and C. R. Mendonca, *Opt. Express*, 2012, **20**, 15106.

27 A. Simo, J. Polte, N. Pfander, U. Vainio, F. Emmerling and K. Rademann, *J. Am. Chem. Soc.*, 2012, **134**, 18824–18833.

28 J. Rozra, I. Saini, S. Aggarwal and A. Sharma, *Adv. Mater. Lett.*, 2013, **4**, 598–604.

29 N. M. B. A. Herrera, S. Buchner, R.V. Camerini, C. Jacinto, *Opt. Mater. (Amst).*, 2016, **52**, 230–236.

30 Y. Huang, W. Xiang, S. Lin, R. Cao, Y. Zhang, J. Zhong and X. Liang, *J. Non. Cryst. Solids*, 2017, **459**, 142–149.

31 A. Awang, S. K. Ghoshal, M. R. Sahar, R. Arifin and F. Nawaz, *J. Lumin.*, 2014, **149**, 138–143.

32 S. K. Ghoshal, A. Awang, M. R. Sahar and R. Ari, *J. Lumin.*, 2015, **159**, 265–273.

33 H. Kim, D. Zhou, R. Wang, Q. Jiao, Z. Yang and Z. Song, *Ceram. Int.*, 2015, **41**, 2648–2653.

34 S. Mohan, K. Singh, G. Sharma and L. Gerward, *Opt. Mater. (Amst).*, 2008, **70**, 1173–1179.

35 S. Naidu, *J. Mod. Phys.*, 2011, **2**, 1062–1066.

36 Y. Q. Zhang, Z. M. Yang, G. F. Yang, Z. D. Deng and Z. H. Jiang, *J. Phys. Chem. Solids*, 2005,

66, 1281–1286.

37 O. M. Efimov, L. B. Glebov, K. A. Richardson, E. Van Stryland, T. Cardinal, S. H. Park, M. Couzi and J. L. Bruneel, *Opt. Mater. (Amst).*, 2001, **17**, 379–386.

38 M. Kaempfe, T. Rainer, K. Berg, G. Seifert and H. Graener, *Appl. Phys. Lett.*, 1999, **74**, 1200–1202.

39 M. Watanabe, S. Juodkazis, H.-B. Sun, S. Matsuo and H. Misawa, *Appl. Phys. Lett.*, 2000, **77**, 13–15.

40 H.-B. Sun, S. Juodkazis, M. Watanabe, S. Matsuo, H. Misawa and J. Nishii, *J. Phys. Chem. B*, 2000, **104**, 3450–3455.

41 D. Huang, F. Liao, S. Molesa, D. Redinger and V. Subramanian, *J. Electrochem. Soc.*, 2003, **150**, G412–G417.

42 A. J. Taylor, T. S. Clement and G. Rodriguez, *Opt. Lett.*, 1996, **21**, 1812.

43 T. Xu, F. Chen, X. Shen, S. Dai, Q. Nie and X. Wang, *Mater. Res. Bull.*, 2010, **45**, 1501–1505.

44 R. Bala, A. Agarwal, S. Sanghi and N. Singh, *Opt. Mater. (Amst).*, 2013, **36**, 352–356.

45 C. Zhang, W. Xiang, H. Luo, H. Liu, X. Liang, X. Ma, L. Pei, Z. Chen, J. Li, H. Gao and L. Ma, *J. Alloys Compd.*, 2014, **602**, 221–227.

46 G. Jagannath, B. Eraiah, A. Gaddam, H. Fernandes, D. Brazete, K. Jayanthi, K. N. Krishnakanth, S. Venugopal Rao, J. M. F. Ferreira, K. Annapurna and A. R. Allu, *J. Phys. Chem. C*, 2019, **123**, 5591–5602.

47 R. F. Souza, M. A. R. C. Alencar, J. M. Hickmann, R. Kobayashi, L. R. P. Kassab, R. F. Souza and R. Kobayashi, *Appl. Phys. Lett.*, 2006, **89**, 171917.

48 X. Tiefeng, C. Feifei, D. Shixun, N. Qiuhua, S. Xiang and W. Xunsi, *Phys. B Condens. Matter*, 2009, **404**, 2012–2015.

49 F. E. P. Dos Santos, F. C. Fávero, A. S. L. Gomes, J. Xing, Q. Chen, M. Fokine and I. C. S. Carvalho, *J. Appl. Phys.*, 2009, **105**, 1–4.

50 J. M. P. Almeida, D. S. Da Silva, L. R. P. Kassab, S. C. Zilio, C. R. Mendonça and L. De Boni, *Opt. Mater. (Amst).*, 2014, **36**, 829–832.

51 C. B. De Araújo, T. R. Oliveira, E. L. Falcão-Filho, D. M. Silva and L. R. P. Kassab, *J. Lumin.*, 2013, **133**, 180–183.

52 G. Jagannath, B. Eraiah, K. NagaKrishnakanth and S. Venugopal Rao, *J. Non. Cryst. Solids*, 2018, **482**, 160–169.

53 A. S. L. Gomes, E. L. Falcão Filho, C. B. De Araújo, D. Rativa, R. E. De Araujo, K. Sakaguchi, F. P. Mezzapesa, I. C. S. Carvalho and P. G. Kazansky, *J. Appl. Phys.*, 2007, **101**, 033115.

54 V. T. Adamiv, I. M. Bolesta, Y. V. Burak, R. V. Gamernyk, I. D. Karbovnyk, I. I. Kolych, M. G. Kovalchuk, O. O. Kushnir, M. V. Periv and I. M. Teslyuk, *Phys. B Condens. Matter*, 2014, **449**, 31–35.

55 Z. Jianliang, N. I. E. Qiuhua, D. A. I. Shixun, X. U. Tiefeng and C. Feifei, *J. Wuhan Univ. Technol. Sci. Ed.*, 2011, **26**, 61–64.

56 K. Nanda, R. S. Kundu, S. Sharma, D. Mohan, R. Punia and N. Kishore, *Solid State Sci.*, 2015, **45**, 15–22.

57 M. V. Rao, V. V. Ravi Kanth Kumar, N. K. Shihab and D. N. Rao, *Opt. Laser Technol.*, 2018, **107**, 110–115.

58 P. S. Salmon and A. Zeidler, *J. Phys. Condens. Matter*, 2015, **27**, 133201.

59 R. L. Mozzi and B. E. Warren, *J. Appl. Crystallogr.*, 1970, **3**, 251–257.

60 J. Krogh-Moe, *Acta Crystallogr.*, 1962, **15**, 190–193.

61 J. Krogh-Moe, *J. Non. Cryst. Solids*, 1969, **1**, 285–302.

62 L. Baia, R. Stefan, W. Kiefer, J. Popp and S. Simon, *J. Non. Cryst. Solids*, 2002, **303**, 379–386.

63 A. S. L. Gomes, E. L. Falcão Filho, C. B. De Araújo, D. Rativa, R. E. De Araujo, K. Sakaguchi, F. P. Mezzapesa, I. C. S. Carvalho and P. G. Kazansky, *J. Appl. Phys.*, 2007, **101**, 1–7.

64 P. Buffat and J.-P. Borel, *Phys. Rev. A*, 1976, **13**, 2287–2298.

65 S. Singla, O. P. Pandey and G. Sharma, *J. Non. Cryst. Solids*, 2019, **521**, 119481.

66 N. Shasmal and B. Karmakar, *J. Non. Cryst. Solids*, 2017, **463**, 40–49.

67 I. Soltani, S. Hraiech, K. Horchani-Naifer, H. Elhouichet, B. Gelloz and M. Férid, *J. Alloys Compd.*, 2016, **686**, 556–563.

68 P. D. Townsend, R. Brooks, D. E. Hole, Z. Wu, A. Turkler, N. Can, A. Suarez-Garcia and J.

Gonzalo, *Appl. Phys. B Lasers Opt.*, 2001, **73**, 345–353.

69 H. Inouye, K. Tanaka, I. Tanahashi and K. Hirao, *Jpn. J. Appl. Phys.*, 1998, **37**, L1520–L1522.

70 R. A. Ganeev, M. Suzuki, M. Baba, M. Ichihara and H. Kuroda, *J. Appl. Phys.*, 2008, **103**, 063102.

71 D. Compton, L. Cornish and E. Van Der Lingen, *Gold Bull.*, 2003, **36**, 51–58.

72 Y. Hamanaka, K. Fukuta, A. Nakamura and P. Mulvaney, *Appl. Phys. Lett.*, 2004, **84**, 4938–4940.

73 R. Del Coso, J. Requejo-Isidro, J. Solis, J. Gonzalo and C. N. Afonso, *J. Appl. Phys.*, 2004, **95**, 2755–2762.

74 Y. Hamanaka, A. Nakamura, S. Omi, N. Del Fatti, F. Vallée and C. Flytzanis, *Appl. Phys. Lett.*, 1999, **75**, 1712–1714.

75 J. Yumoto, S. Fukushima and K. Kubodera, *Opt. Lett.*, 1987, **12**, 832.

76 A. Clementi, N. Chiodini and A. Paleari, *Appl. Phys. Lett.*, 2004, **84**, 960–962.

77 A. Awang, S. K. Ghoshal, M. R. Sahar and R. Arifin, *Opt. Mater. (Amst).*, 2015, **42**, 495–505.

78 L. R. P. Kassab, F. A. Bomfim, J. R. Martinelli, N. U. Wetter, J. J. Neto and C. B. De Araujo, *Appl. Phys. B Lasers Opt.*, 2009, **94**, 239–242.

79 T. Som and B. Karmakar, *J. Appl. Phys.*, 2009, **105**, 013102.

80 M. R. Dousti, M. R. Sahar, S. K. Ghoshal, R. J. Amjad and A. R. Samavati, *J. Mol. Struct.*, 2013, **1035**, 6–12.

81 S. K. Singh, N. K. Giri, D. K. Rai and S. B. Rai, *Solid State Sci.*, 2010, **12**, 1480–1483.

82 D. Mariano, L. Reyes, P. Kassab, S. R. Lüthi, C. B. De Araújo, S. L. Anderson, M. José and V. Bell, *Appl. Phys. Lett.*, 2007, **90**, 1–3.

83 Z. Pan, A. Ueda, R. A. Jr, A. Burger, R. Mu and S. H. Morgan, *J. Non. Cryst. Solids*, 2010, **356**, 1097–1101.

CHAPTER 2 LITERATURE REVIEW

Overview

Constant efforts are being made to develop appropriate material to be used in optical components. These materials are supposed to have low absorption, higher optical nonlinearity and faster response. Among various materials used in optical devices, glasses containing metal nanoparticles are one of the best candidates as one can tune the property according to the requirement by simply changing the glass composition. Further, the properties are highly sensitive to the choice of nanoparticles. However, during the fabrication of glasses containing nanoparticles, coagulation and evaporation of nanoparticles occurs that prevents the uniforms distribution inside the glassy matrix. Therefore, it becomes necessary to study the behaviour of different metal nanoparticles in several glass systems. In present section, a concise summary of research on the various glass systems containing metal nanoparticles is presented along with the condition that can help to reduce the factors that can reduce the coagulation of particles and helping to achieve better nonlinearity. Based on these study, the literature gap and objectives to carry out research is presented at the end of this chapter.

2.1. Glasses for optical applications

Materials required for optical application should possess (i) higher susceptibilities against variation in the refractive index induced by light so that low power intensities can activate the material; (ii) small linear and nonlinear coefficients of absorption to achieve longer propagation lengths that reduces the possibility of photo induced thermal effects; and (iii) shorter lifetime for refractive index change that leads to faster signal processing. Organic materials, inorganic semiconductors and glasses are promising nominees for optical media. Among various candidates listed in table 2.1, glasses find major interest because of highest figure of merit (FOM), low response time and high nonlinear susceptibility in comparison to other candidate materials for opto-electronic devices. In addition, glasses are materials of considerable interest because of their unique properties like hardness, good tensile strength, optical transparency and excellent stability towards corrosion [1–4].

Table 2.1: Summary of linear and nonlinear parameters that illustrate the optical performance of different nonlinear materials. n_2 is nonlinear refractive index, a_0 is linear absorption coefficient, W and T are the FOM for switching application [5] and l is the wavelength at which measurements are done. Goal for W is >1 and for T is <1.

Material	**n_2 (cm^2/W)**	**α_0 (cm^{-1})**	**W**	**T**	**λ (nm)**	**Reference**
Semiconductors						
GaAs	-3×10^{-13}	1	<2.8	>17	1064	[6]
AlGaAs	-4×10^{-14}	18	2.5	0.9	810	[7]
Organics						
PTS	-2×10^{-12}	0.8	40	4	1064	[6]
DANS	8×10^{-14}	0.2	>2.5	<1	1310	[7]
DEANST	6×10^{-14}	10^{-2}	>40	<1	1064	[7]
Poly-4BCMU	5×10^{-14}	0.2	>2.5	<1	1310	[8]
DAN2	2×10^{-13}	1	>2	<1	1064	[7]
Inorganics (glasses)						
SiO2	2×10^{-16}	10^{-6}	>103	<<1	1064	[9]
BK7	3×10^{-16}	–	-	-	1500	[9]

2.2. Importance of small metal nanoparticles in glass

Oxide glasses are generally colourless. Colours appear in these glasses after the incorporation of metal nanoparticles. Ruby glass is one of the example. Particularly, such glasses exhibit fascination linear and nonlinear optical behaviour due to large coefficient of absorption in visible region associated with LSPR of metal nanoparticles.

In order to fabricate optical devices, laser irradiation has become powerful tool since it induces several beneficial modifications. Interaction of ultra-short laser pulses with glass containing metal ions have been examined in detail for its applications in functional optical devices. Among metallic ions, noble metal ions of silver, copper and gold have attracted several research interests. When glass containing silver nanoparticles was irradiated with intense fs-laser pulses, permanent change in sample colour is observed. The wavelength of the laser was so selected that it lies in the region of the particles' surface plasmon resonance [10]. Watanabe *et al.* [11] studied the photosensitivity of Ag^+ doped soda alumino-phosphate glass. Formation of Ag^0 and Ag^+ color centres in the glass is reported after the exposure to near-ultraviolet femtosecond laser pulses. Haglund *et al.* [12] analysed that the nonlinear response of nanostructures generated using pulsed laser deposition is higher than those generated using particle beam. Cheng *et al.* [13] examined the variation in refractive index of Foturan glass doped with Ag^+-ions after fs-laser irradiation followed by post baking. An effective route to precipitate metallic nanoparticles inside the glassy matrix after intense fs-laser irradiation was developed by Qiu *et al.* [14,15]. This approach facilitates to produce/precipitate metallic nanoparticles in desired area inside the glass. The decolouration and formation of Ag-related color centres and their precipitation, dissolution of silver nanoparticles in Ag^+-doped phosphate glass by 800 nm fs-laser followed by subsequent thermal treatment and the dissolution of the nanoparticles increased with an increase in annealing temperature [16]. As per the studies carried out by Simo *et al.* [17] on formation mechanism of Ag nanoparticles inside the glassy matrix, to have control over distribution and particle size, a constitutive understanding of the kinetics of the particle evolution and mechanisms is highly required. Rozra *et al.* [18] prepared the silver nanoparticles embedded glass using vacuum vapour deposition followed by subsequent thermal annealing. An increase in refractive index and dielectric constant from 1.53 to 1.96 and 2.4 to 3.8 respectively, have been observed with the addition of silver nanoparticles. Moreover, these parameter are found to be highly dependent on annealing time as the size of nanoparticles formed are reliant on the same. Photoluminescence of the silver glass nanocomposities was also studied. Tyrk *et al.* [19] introduced a new method to transform the shape of embedded metal nanoparticles inside the glass by using radially and azimuthally polarised light. Eugen *et al.* [20,21] achieved the uniform dispersion of nanoparticles inside the tellurite glass by direct incorporation of pre synthesised nanoparticles without any heat treatment that leads to enhancement in optical efficiency of the glass. In addition, enhanced luminescence can be achieved without subsequent heat treatment in Eu/Silver codoped borosilicate glass [22].

Copper nanoparticles have also attracted several research interests because of their exceptional chemical, electronic and optical properties that can be tuned by simply modifying their shape, size, crystalline structure, composition and dielectric environment around them. Lipovskii *et al.* [23] demonstrated the dissolution of copper nanoparticles in glass sample under the mutual action of DC electric field at elevated temperature. Transformation from red color of the sample to disappearance of the colour has been observed which in turn depends on local optical density in the surface layer of the sample and the surface relief of the electrode. Haglund *et al.* [24] studied the linear and nonlinear behaviour of Ag and cu deposited on soda-lime substrate prepared by ion-exchange technique. Podsvirov *et al.* [25] confirmed experimentally that irradiating photochromic glasses containing Cu^+ ions by electron beam is an effective way to produce metallic Cu nanoparticles inside the glass. However, the formation of Cu nanoparticles is limited to near surface layers of the glass only. Fast response time (35 ps) of Cu implanted silica has been reported by Hanlund *et al.* [26]. Almeida *et al.* [27] investigated the formation of Cu nanoparticles on the surface as well as in the bulk of borosilicate glass after fs-laser irradiation under transmission electron microscopy, electron diffraction and UV-Vis absorption. It was confirmed that only femtosecond lasers allow to control the morphology of nanoparticles three-dimensionally. Manzani *et al.* [28] determined the nonlinear behaviour of tungsten-phosphate glasses containing Cu nanoparticles with the help of Z-scan and pump probe technique using fs-laser pulses. The measured value of nonlinear refractive index is around 2.0×10^{-19} m^2/W from visible to telecom region. Jiménez *et al.* [29] in their work have shown that a phosphate glass matrix prepared with stoichiometric amounts of CuO and SnO dopants by the melting technique is well effective for the precipitation of copper nanoparticles upon heat treatment. While processing the glass thermally, Sn^{2+} chemically reduces the ionic copper and ultimately leads to the production copper nanoparticles in the glassy matrix. The existence of copper nanoparticles is confirmed by the presence of the SPR around 574 nm that leads to reduction of Cu^+ photoluminescence. Moreover, the emission band shows a dip due to reabsorption by copper nanoparticles near resonance. Whereas Xiang *et al.* [30] studied the copper nanoparticles containing Na_2O-B_2O_3-SiO_2 glass prepared by combining the sol–gel process and controlled thermal processing in H_2 gas using XRD, TEM and HRTEM to explore the structural properties and Z-scan to measure the optical nonlinear susceptibility which comes out to be 2.6×10^{-14} esu. An empirical linear dependence of the diffusion activation energy on the glass transition temperature with broad applicability is suggested [31]. Kumar *et al.* [32] reported the value of nonlinear susceptibility of 0.56 × 10^{-11} esu in copper containing soda lime glass that shows possible applications in the field of photonics.

Among the noble-metal nanoparticles, gold nanoparticles are particularly more interesting due to their catalytic properties and chemical inertness. The properties shown by gold nanoparticles are substantially attributed to their size, concentration and aggregation level. Haglund *et al.* [33–35] synthesised metal-nanocluster composites using ion implantation technique. He found that Au:sapphire nanocomposites show an order of magnitude higher nonlinearity as compared to Cu:silica nanocomposite. Moreover, it was proposed that nonlinear susceptibility is a function of size of nanoparticles along with the lifetime and dephasing time of thermal and electronic excitations [36]. Inouye *et al.* [37] in 1998 reported an ultrashort response time of 240 fs in gold nanoparticle embedded SiO_2 glass matrix obtained using femtosecond OKS experiment. The self-diffraction of incident pulse owing to the transient index grating originates the ultra-fast response. Calculated value of $\chi^{(3)}$ of the gold nanoparticle system is 2.0 $\times 10^{-8}$ esu (superior as compared to glasses containing other nobel metal nanoparticles) in the femtosecond region. Ganeev *et al.* [38] in 2008 compared the third and higher-order NLO behaviour of Ru, Pd, Pt and Au nanoparticles. The nonlinear parameters (refractive indices and coefficients of absorption) of these nanoparticles suspensions was measured using the 792 nm femtosecond and picosecond pulses. When the probe radiation of 210 ps pulses were used, highest values of these parameters (-8×10^{-14} m^2W^{-1} and 1.7×10^{-10} mW^{-1}) were obtained for gold nanoparticles suspension. Highest value of nonlinear susceptibility can be achieved after gold doping because of its lower electronegativity (1.8) as compared to other metal nanoparticles [39]. Som and Karmakar [40] in 2010 used single step melt-quench technique to synthesise elliptical gold nanoparticles dispersed dichroic glass nanocomposites. The elliptical shape of the gold nanoparticles induces dichroic behaviour in glass nanocomposites. In addition, these glasses are found to be promising candidate for display devices, laser and numerous nanophotonic applications. Siegel *et al.* [41] examined the electrical and optical properties, crystalline structure and density of gold nanostructures on glass substrate. DC sputtering was used for the preparation of these nanostructures. It was concluded that, gold nano layers (<10 nm) possess both semiconducting and metal like conductivity in wide temperature range. Rivera *et al.* [42] compared the effect of silver and gold nanoparticles on photoluminescence of Er^{3+} doped tellurite glasses. The interaction between metallic nanoparticles and Er^{3+} ion through energy transfer results in enhanced luminescence intensity. This enhancement was more prominent in glasses containing gold nanoparticles. Anavekar *et al.* [43] in 2014 studied oxide glass doped with gold by using nanosecond laser pulse excitation.

Z-scan experiments with 532 nm wavelength pulses are used to excite glass samples which show the optical limiting effect of these gold nanoparticles doped glasses. Sazali *et al.* [44] have inspected the impact of gold nanoparticles concentration in stimulating the ligand field interaction inside the erbium-tellurite glass network and a strong correlation between the ligand parameters and gold nanoparticle content have been reported. Ali *et al.* [45] used field-assisted solid-state ion-exchange technique to diffuse gold ions into soda lime borosilicate and silicate glasses. Both the glass systems were prepared under similar experimental conditions. UV–Vis spectra of the doped glasses exhibit broad SPR peaks at 500 and 525 nm for soda lime borosilicate and silicate glasses, respectively. The obtained spectra were fitted using the Mie–Gans model for spheroidal nanoparticles and the Mie model for spherical nanoparticles. Catauro *et al.* [46] studied the biological, chemical and antibacterial properties of silica glasses containing different concentrations of Ag and Au nanoparticles synthesized via sol-gel method. It was observed that antibacterial activity of Ag^+ ions gets reduced in vicinity of gold nanoparticles. Chen *et al.* [47] investigated germanium–gallium–sulphur glasses doped with different amounts of gold. Introduction of gold results in improved third-order optical nonlinearities of the germanium–gallium–sulphur glasses by approximately 47%. Ashok *et al.* [48,49] reported the enhanced structural, physical and electrical properties with increasing concentration of Au_2O_3 concentration in Antimony glass.

2.3. Role of matrix

From last few decades, oxide glasses have attracted several research interests due to its thermal and chemical stability, mechanical properties and wide range of applications in various fields of [50–56]. More specifically borate based glasses are seeking more attention because of its faster nonlinear response and higher nonlinear parameters as reported in Table 1.2. Husinsky *et al.* [57] compared the optical nonlinearity of different silicate glass systems containing gold nanoparticles prepared by ion implantation and concluded that among various systems borosilicate glass shows the highest value of two photon absorption (16.25 cm/GW). Faznny *et al.* [58] compared the effect of lanthanum nanoparticles and lanthanum oxide on the nonlinear behaviour of zinc borotellurite glasses. Nonlinear parameters show inconsistent dependency on concentration of both the dopants. Moreover, the nanoparticles doped glasses are reported to exhibit higher values of the nonlinear parameters as compared to the glasses containing lanthanum oxide. Increase in first linear and third nonlinear susceptibility has been observed by Gomaa *et al.* [59] with the increase in niobium penta oxide in bismuth borate glass. Rao *et al.* [60] confirmed the increase in linear and nonlinear optical parameters ($\chi^{(1)}$, $\chi^{(3)}$, n_o and n_2) with the increase in V_2O_5 content upto 0.6 mol% in LiO_2-WO_3-B_2O_3 glass matrix. Jagannathan *et al.* [61] recently studied the role of Li_2O and CaF_2 on optical behaviour of gold nanoparticles doped fluoroborate glasses. Prepared glasses were dichroic in nature and the nonlinear refractive index and nonlinear absorption coefficient gets improved with the increase of Li_2O content in the vicinity of gold nanoparticles. Ni nanoparticles containing sodium borosilicate glass has been reported to shows the nonlinear susceptibility as high as 5.51×10^{-12} esu that makes them highly suitable for nonlinear optical devices [62]. Also, the presence of hyper-polarizable Sb^{3+} and Sb^{5+} ions along with the existence of NBOs in the sodium borate glass results in enhanced nonlinear effect [63]. Sundari et al. [64] confirmed the suitability of sodium penta borate to design passive optical limiting component due to its optical limiting behaviour. Zhong *et al.* [65] reported the nonlinear enhancement in sodium borate glass with the increase in In_2O_3 content from 0.5 to 1.5 mol%. Whereas, Huang *et al.* [66] studied the effect of NiO nanoparticles on nonlinear behaviour of sodium borate glass. Rajaramakrishna *et al.* [67] reported the formation of gold nanoparticles in lead borate glasses after subsequent annealing at particular time-temperature combinations. Striking ruby color is observed after slow cooling such glasses to room temperature. At sufficiently low input intensity heat treated glasses exhibit saturable absorption whereas the glasses without heat treatment shows reverse saturable absorption at high input intensity which could be used to form detectors. Borate glasses show superior property for slow relaxation processes [68].

Heavy metal oxide in the glass matrix acts as a glass modifier that reduces the melting point of borate glass and supports the direct incorporation of metal nanoparticles. Presence of PbO results in enhanced coagulation of gold nanoparticles that could reduce the optical efficiency of the glass containing nanoparticles as reported by Zeng *et al.* [69]. Almeida *et al.* [70] confirmed that the presence of Bi_2O_3 along with gold enhances the nonlinear refractive upto 1.5 times as compared to the glass containing PbO. Also, such glass systems have ultrafast response less than the laser pulse duration (<220 fs). Xu *et al.* [71] used bismuth borosilicate glass to disperse metal nanoparticle because of its superior glass forming ability [71]. Also, it is worth noting that high processing temperature leads to clustering of heavy metal oxide species and hence formation of nanoparticles takes place [72]. Presence of these nanoparticles influences the physical as well as optical behaviour of the glass that needs to be taken care of.

2.4. Use of rare earths for better dispersion

In order to achieve better dispersion of nanoparticles currently rare earth doped glasses are extensively used. Ghoshal *et al.* [73–75] have explained the occurrence of Ostwald’s ripening of gold nanoparticles embedded zinc–sodium tellurite glass with the heat treatment. This process leads to loss of control over the size of nanoparticle and in turn largely affects the emission spectra of Er^{3+} ions. Rouge *et al.* [76] used the Zirconia protected gold nanoparticles in order to prevent coagulation of gold nanoparticles in sol–gel derived silica glasses. Also, the estimated value of second-order nonlinear coefficient of absorption (β) is around 13.7cm GW^{-1} at a wavelength near the Surface Plasmon Resonance of gold nanoparticles. Hayakawa *et al.* [77] confirmed the enhanced emission in Eu^{3+} doped borosilicate glass with the incorporation of polymer protected gold nanoparticles. This polymer protection controls the size of gold nanoparticles inside the glassy matrix. In a recent work, the covering of gold nanoparticles by Dy^{3+} in bismuth borosilicate glass that reduces coagulation and hence enhances the nonlinear efficiency of the material is reported [78].

Moreover, the energy transfer mechanism between metal nanoparticle and rare earth ions leads to enhanced luminescence and upconversion processes. Kassab *et al.* [79] studied the effect of presence of gold nanoparticles on upconversion mechanism in infrared-to-visible frequency region of TeO_2–PbO–GeO_2 glasses codoped with Er^{3+}–Yb^{3+}. It is reported that the combined effects of gold nanoparticles and the efficient Yb^{3+}-Er^{+3} energy transfer mechanism change the up-conversion visible spectrum. Rivera *et al.* [80] studied that gold nanoparticles provide tuneable emission resulting in a large enhancement for the $^2H_{11/2} \rightarrow {}^4I_{13/2}$ (emission at 805 nm) and $^4S_{3/2} \rightarrow {}^4I_{13/2}$ (emission at 840 nm) electronic transitions of Er^{3+} ions. This is associated with the quantum yield of the energy transfer process. The excitation pathways, up-conversion and luminescence spectra of Er^{3+} ions are described through simplified energy level diagrams. They observed that up-conversion is favoured by the excited-state absorption due to the presence of the gold nanoparticles coupled with the Er^{3+} ions within the glass matrix. Sazali *et al.* [81] prepared gold nanoparticles dispersed TeO_2–PbO–PbO_2 glasses doped with Er^{3+} and examined the effect of gold nanoparticles on its optical behaviours. The decrement in the optical band gap value from 2.82 to 1.09 eV with the increase in concentration of gold (0.025-0.1 mol%) is ascribed to the formation of more nanoparticles nucleation sites. The room temperature up-conversion emission spectra under 779 nm excitations shows three peaks centred at 520, 550 and 660 nm. Significant enhancement in the luminescence intensity observed is primarily attributed radiative energy transfer and SPR mediated strong local field effect of gold nanoparticles in the vicinity of Er^{3+} ion. Dan *et al.* [82] reported twenty-fold enhancement in red upconversion emission intensity band centred at 850 nm with the increase of $HAuCl_4$ concentration in Er^{3+}/Yb^{3+} ion in transparent glass–ceramics SiO_2–AlF_3–BaF_2–

TiO_2–$CaCO_3$ containing BaF_2 nanocrystals that further reaches its maximum at 1.5 mol% and decrease in emission intensity is observed which is attributed to the self-quenching effect.

Balzaretti *et al.* [83] synthesised the Sm^{3+} doped B_2O_3–PbO–Bi_2O_3–GeO_2 transparent glass implanted with univalent gold ions using an ions beam. Subsequent exposure of ion beam led to crystallization in the glass which makes them less useful in the field of optics. Garcia *et al.* [84] reported the improved solar cell efficiency of germinate glasses in proximity of gold nanoparticles when compared to germinate glasses without gold nanoparticle. The enhancement in efficiency was ascribed to the energy transfer from excited nanoparticles to the Eu^{3+} ions and the plasmonic enhancement around Eu^{3+} ions due to the presence of gold nanoparticles. Herrera *et al.* [85] studied the formation of Au nanoparticles in Pr^{3+} doped heavy metal oxide (B_2O_3-PbO-Bi_2O_3-GeO_2) glasses after the laser irradiation followed by subsequent annealing below the glass transition temperature which leads to the production of nanocrystals along with the formation of nanoparticles. Broadband emission in infrared region is observed under 488 nm excitation that makes such glasses highly suitable for optical telecommunication and data transfer applications. Thermal annealing of the glass results in significant enhancement of band intensity which is probably associated with local field effect of gold nanoparticles. Huang *et al.* [86] reported the enhancement in third order nonlinearities in sodium-borosilicate glasses containing nickel and gold bimetallic nanoparticles synthesised by sol gel technique followed by controlled heat treatment. For the Au/NiO nanoparticles dispersed glass, the improved third-order nonlinear behaviour mainly depends on a contribution from stronger nonlinear refraction response. Shasmal *et al.* [87] presented the production of uniformly distributed gold nanoparticle containing Dy doped antimony glass by single step melt quench technique. Two important observations are made. First is the enhancement in luminescence intensity after the attainment of critical size of the nanoparticles and second is the reduction in intensity due to crystallization in the glass matrix observed after heat treatment. Prusova *et al.* [88] demonstrated the luminescence enhancement in Eu doped phosphate glasses is a function of size of gold nanoparticles.

2.5. Gaps in the studies

1. The novel glasses containing metal nano particles have been studied in details. However, no acceptable space-selective control on the distribution and particle size was achieved. In addition to this the method (ion exchange, ion implantation, low energy beam mixing, physical vapour deposition, metal dielectric co-sputtering deposition and sol gel) used requires heat treatment as one of the important step of the technique which

leads to the formation of various phases along with the crystallization which reduces the optical efficiency of the material. In order to have efficient materials a methods free from heat treatment should be used.

2. Silver and copper doped glasses have been extensively studied because of their exceptional chemical, electronic and optical properties that are an intrinsic function of their shape, size, crystalline structure, composition and dielectric environment around the nanoparticles. However, other noble metals like Au, Pt, Pd, Rh etc. have not been studied extensively because of their higher cost. Au shows superior optical behaviour in NIR region and moreover, its lower electronegativity (1.8) as compared to silver (1.9) and copper (1.9) enables the material containing gold nanoparticles to show higher third order nonlinear susceptibility making them practically more important and requires detailed study.
3. A well-known phenomena Ostwald's repining occurs in absence of any stabilizers according to which the small nanoparticles coagulates inside the dielectric material resulting in the formation of bigger lumps of the metal inside the dielectric matrix. It acts as a barrier for the space selective control on the distribution of nanoparticles. This requires elaborate and detailed study.
4. New functionalities can be added to the material by accurate spatial control of the distribution of inhomogeneities. However, the crystalline features created in so far by laser processing have spatial extent of the order of microns or more, so they are not suitable for many applications where sub-micron size inclusions are required.
5. A different Femtosecond Laser Processing producing instead of spatially ordered patterns with periodic arrangement of inclusions can be used to test the possibility to fabricate photonic band gap structures. In this case, considering the size of inclusions, the periodicity of the pattern determines the wavelength region where the photonic structure is active. Attainment of processed domains with size well below the visible wavelength would allow for the production of photonic band gap structures operating in the visible-NIR region. This could pave the way to the realization of integrated optical components in glass like laser cavities or amplifiers. In addition, the novel functionalities and uses of these patterned glasses would be interesting.
6. The effect of addition of nanoparticles on the non-linear refractive index have been extensively studied due to good non-linear response of metallic nanoparticles. But the

variation in linear refractive index in Uv-vis and THz region is least reported. The materials showing good response in these regions can find wide applications in photonics.

2.6. Objectives

Considering the above facts following objectives have been proposed for present investigation:

1. To synthesize (x) Bi_2O_3-(100-x) B_2O_3 (x=30 mol %, 35 mol %, 40 mol %), $40Bi_2O_3$-$40B_2O_3$-$20SiO_2$ glasses containing gold nanoparticles.
2. To study the effect of different stabilizers (Europium oxide, Europium fluoride, potassium thiocynate) on the morphology of nanoparticles inside the glass and their influence on properties.
3. To calculate nonlinear refractive index and nonlinear absorption coefficient using z-scan technique.
4. To study the effect of stabilizers on the luminescence properties of the nanoparticles present inside the glass.
5. To characterize the glass using XRD, SEM, TEM for morphological studies, DTA and FTIR for thermal and structural properties and UV, PL and Z-scan for both linear and non-linear optical properties.

References:

1 S. Soo, *Mater. Res. Bull.*, 2014, **51**, 336–344.

2 S. Sindhu, S. Sanghi, A. Agarwal, V. P. Seth and N. Kishore, *Mater. Chem. Phys.*, 2005, **90**, 83–89.

3 K. Singh, H. Singh, G. Sharma, L. Gerward, A. Khanna, R. Kumar, R. Nathuram and H. Singh, *Radiat. Phys. Chem.*, 2005, **72**, 225–228.

4 M. Peng, D. Chen, J. Qiu, X. Jiang and C. Zhu, *Opt. Mater. (Amst).*, 2007, **29**, 556–561.

5 E. Cattaruzza, G. Battaglin, P. Calvelli, F. Gonella, G. Mattei, C. Maurizio, P. Mazzoldi, S. Padovani, R. Polloni, C. Sada, B. F. Scremin and F. D'Acapito, *Compos. Sci. Technol.*, 2003, **63**, 1203–1208.

6 S. R. Friberg and P. W. Smith, *IEEE J. Quantum Electron.*, 1987, **23**, 2089–2094.

7 J. L. Brédas, C. Adant, P. Tackx, A. Persoons and B. M. Pierce, *Chem. Rev.*, 1994, **94**, 243–278.

8 M. Cha, W. Torruellas, G. Stegeman, H. X. Wang, A. Takahashi and S. Mukamel, *Chem. Phys. Lett.*, 1994, **228**, 73–78.

9 K. Tanaka, in *Springer Handbook of Electronic and Photonic Materials*, eds. S. Kasap and P. Capper, Springer International Publishing, Cham, 2017, p. 1.

10 M. Kaempfe, T. Rainer, K. Berg, G. Seifert and H. Graener, *Appl. Phys. Lett.*, 1999, **74**, 1200–1202.

11 Y. Watanabe, G. Namikawa, T. Onuki, K. Nishio and T. Tsuchiya, *Appl. Phys. Lett.*, 2001, **78**, 2125–2127.

12 R. F. Haglund, Jr., C. N. Afonso Rodriguez, G. Battaglin, M. Godbole, F. Gonella, J. D. Hamilton, D. H. Lowndes, R. H. Magruder III, P. Mazzoldi, D. H. Osborne, Jr. and J. Solis, *Laser Appl. Microelectron. Optoelectron. Manuf. II*, 1997, **2991**, 90–101.

13 Y. Cheng, K. Sugioka, M. Masuda, K. Shihoyama, K. Toyoda and K. Midorikawa, *Opt. Express*, 2003, **11**, 1809–1816.

14 J. Qiu, X. Jiang, C. Zhu, M. Shirai, J. Si, N. Jiang and K. Hirao, *Angew. Chemie - Int. Ed.*, 2004, **43**, 2230–2234.

15 J. Qiu, K. Miyauchi and Y. Kawamoto, *Appl. Phys. Lett.*, 2002, **81**, 394–396.

16 Q.-Z. Zhao, J.-R. Qiu, X.-W. Jiang, C.-J. Zhao and C.-S. Zhu, *Opt. Express*, 2004, **12**, 4035–4040.

17 A. Simo, J. Polte, N. Pfander, U. Vainio, F. Emmerling and K. Rademann, *J. Am. Chem. Soc.*, 2012, **134**, 18824–18833.

18 J. Rozra, I. Saini, S. Aggarwal and A. Sharma, *Adv. Mater. Lett.*, 2013, **4**, 598–604.

19 M. A. Tyrk, S. A. Zolotovskaya, W. A. Gillespie and A. Abdolvand, 2015, **23**, 716–718.

20 E. Culea, I. Vida-Simiti, G. Borodi, E. N. Culea, R. Stefan and P. Pascuta, *J. Mater. Sci.*, 2014, **49**, 4620–4628.

21 E. Nicolae, P. Pascuta, M. Pustan, D. R. Tamas-gavrea, L. Pop and I. Vida-simiti, *J. Non. Cryst. Solids*, 2015, **408**, 18–25.

22 M. Haouari, F. Ben Slimen, A. Maaoui and N. Gaumer, *J. Alloys Compd.*, 2018, **743**, 586–596.

23 A. A. Lipovskii, V. G. Melehin and V. D. Petrikov, *Tech. Phys. Lett.*, 2006, **32**, 275–277.

24 R. F. H. Jr., C. N. A. Rodriguez, G. Battaglin, M. Godbole, F. Gonella, J. D. Hamilton, D. H. Lowndes, R. H. M. III, P. Mazzoldi, D. H. O. Jr. and J. Solis, *Int. Conf. Fiber Opt. Photonics Sel. Pap. from Photonics India*, 1996, **96**, 21–26.

25 O. A. Podsvirov, A. I. Sidorov, V. A. Tsekhomskii and A. V Vostokov, *Phys. Solid State*, 2010, **52**, 1906–1909.

26 L. Yang, K. Becker, F. M. Smith, R. H. Magruder III, R. F. Haglund, Jr., L. Yang, R. Dorsinville, R. R. Alfano and R. A. Zuhr, *J. Opt. Soc. Am. B*, 1994, **11**, 457.

27 J. M. P. Almeida, L. De Boni, W. Avansi, C. Ribeiro, E. Longo, A. C. Hernandes and C. R. Mendonca, *Opt. Express*, 2012, **20**, 15106.

28 D. Manzani, J. M. P. Almeida, M. Napoli, L. De Boni, M. Nalin, C. R. M. Afonso, S. J. L. Ribeiro and C. R. Mendonça, *Plasmonics*, 2013, **8**, 1667–1674.

29 J. A. Jiménez, *Appl. Phys. A Mater. Sci. Process.*, 2014, **114**, 1369–1376.

30 W. Xiang, H. Gao, L. Ma, X. Ma, Y. Huang, L. Pei and X. Liang, *ACS Appl. Mater. Interfaces*, 2015, **7**, 10162–10168.

31 M. Sendova, J. a. Jiménez, R. Smith and N. Rudawski, *Phys. Chem. Chem. Phys.*, 2015, **17**,

1241–1246.
32 P. Kumar, M. C. Mathpal, S. Hamad, S. V. Rao, J. H. Neethling, A. J. van Vuuren, E. G. Njoroge, R. E. Kroon, W. D. Roos and H. C. Swart, *Appl. Mater. Today*, 2019, **15**, 323–334.
33 R. F. H. Jr., *Mater. Sci. Eng. A*, 1998, **253**, 275–283.
34 R. F. Haglund, L. Yang, R. H. Magruder, K. Becker and J. E. Wittig, *Nonlinear Opt. Prop. Adv. Mater.*, 1993, **1852**, 113–124.
35 R. F. Haglund, L. Yang, R. H. Magruder, C. W. White, R. A. Zuhr, L. Yang, R. Dorsinville and R. R. Alfano, *Nucl. Inst. Methods Phys. Res. B*, 1994, **91**, 493–504.
36 L. Yang, D. H. Osborne, R. F. Haglund, R. H. Magruder, C. W. White, R. A. Zuhr and H. Hosono, *Appl. Phys. A Mater. Sci. Process.*, 1996, **62**, 403–415.
37 H. Inouye, K. Tanaka, I. Tanahashi and K. Hirao, *Jpn. J. Appl. Phys.*, 1998, **37**, L1520–L1522.
38 R. A. Ganeev, M. Suzuki, M. Baba, M. Ichihara and H. Kuroda, *J. Appl. Phys.*, 2008, **103**, 063102.
39 S. Ikeda and M. Aniya, *J. Non. Cryst. Solids*, 2012, **358**, 2381–2384.
40 T. Som and B. Karmakar, *Plasmonics*, 2010, **5**, 149–159.
41 J. Siegel, O. Lyutakov, V. Rybka, Z. Kolská and V. Švorčík, *Nanoscale Res. Lett.*, 2011, **6**, 96.
42 V. A. G. Rivera, Y. Ledemi, S. P. A. Osorio, D. Manzani, Y. Messaddeq, L. A. O. Nunes and E. M. Jr, *J. Non. Cryst. Solids*, 2012, **358**, 399–405.
43 R. Rajaramakrishna, C. Saiyasombat, R. V Anavekar and H. Jain, *J. Non. Cryst. Solids*, 2014, **406**, 107–110.
44 E. S. Sazali, M. R. Sahar, R. Arifin, S. K. Ghoshal and M. S. Rohani, *Mater. Sci. Forum*, 2016, **846**, 137–141.
45 S. Ali, Y. Khan, Y. Iqbal, K. Hayat and M. Ali, *J. Nanophotonics*, 2017, **11**, 016011.
46 M. Catauro, F. Papale, P. Caputo and G. Donnarumma, *Int. J. Appl. Ceram. Technol.*, 2017, **14**, 108–116.
47 F. Chen, Q. Yu, B. Qiao, T. Xu, S. Dai and W. Ji, *J. Non. Cryst. Solids*, 2015, **412**, 30–34.
48 J. Ashok, M. Kostrzewa, M. Srinivasa Reddy, V. Ravi Kumar, N. Venkatramiah, M. Piasecki and N. Veeraiah, *J. Am. Ceram. Soc.*, 2018, **102**, 1628–1641.
49 J. Ashok, M. Kostrzewa, A. Ingram, P. Nalluri, N. Venkatramaiah, M. Srinivasa Reddy, V. Ravi Kumar and N. Veeraiah, *J. Am. Ceram. Soc.*, 2019, **102**, 1921–1941.
50 M. A. F. Basha, R. M. M. Morsi, M. M. Morsi and A. F. Basha, *J. Electron. Mater.*, 2019, **48**, 6686–6693.
51 T. A. Taha and A. S. Abouhaswa, *J. Mater. Sci. Mater. Electron.*, 2018, **29**, 8100–8106.
52 A. V. Deepa, M. Priya and S. Suresh, *Sci. Res. Essays*, 2016, **11**, 57–63.
53 A. S. Abouhaswa, M. I. Sayyed, K. A. Mahmoud and Y. Al-Hadeethi, *Ceram. Int.*, 2020, **46**, 17978–17986.
54 S. Mohan, K. Singh, G. Sharma and L. Gerward, *Opt. Mater. (Amst).*, 2008, **70**, 1173–1179.
55 S. Naidu, *J. Mod. Phys.*, 2011, **2**, 1062–1066.
56 Y. Q. Zhang, Z. M. Yang, G. F. Yang, Z. D. Deng and Z. H. Jiang, *J. Phys. Chem. Solids*, 2005, **66**, 1281–1286.
57 W. Husinsky, A. Ajami, P. Nekvindova, B. Svecova, J. Pesicka and M. Janecek, *OPTICS*, 2012, **285**, 2729–2733.
58 M. F. Faznny, M. K. Halimah, C. Eevon, A. A. Latif, F. D. Muhammad, A. S. Asyikin, S. N. Nazrin and I. Zaitizila, *Opt. Laser Technol.*, 2020, **127**, 106161.
59 H. M. Gomaa, I. S. Ali, A. S. Morsy and M. I. Sayyed, *Appl. Phys. A Mater. Sci. Process.*, 2020, **126**, 1–8.
60 L. S. Rao, C. Thirmal and P. R. Rao, *J. Adv. Dielectr.*, 2020, **10**, 1–8.
61 A. Jagannathan, R. Rajaramakrishna, K. M. Rajashekara, J. Gangareddy, V. Pattar K, V. R. S, E. B, J. Angadi V, J. Kaewkhao and S. Kothan, *J. Non. Cryst. Solids*, 2020, **538**, 120010.
62 M. Liu, J. Zhong, X. Ma, Y. Huang and W. Xiang, *J. Non. Cryst. Solids*, 2019, **522**, 119560.
63 G. Jagannath, B. Eraiah, A. Gaddam, H. Fernandes, D. Brazete, K. Jayanthi, K. N. Krishnakanth, S. Venugopal Rao, J. M. F. Ferreira, K. Annapurna and A. R. Allu, *J. Phys. Chem. C*, 2019, **123**, 5591–5602.
64 A. Sundari and S. Manikandan, *J. Mater. Sci. Mater. Electron.*, 2018, **29**, 558–567.
65 J. Zhong and W. Xiang, *Mater. Lett.*, 2017, **193**, 22–25.

66 Y. Huang, Y. Zhang, S. Lin, L. Yan, R. Cao, R. Yang, X. Liang and W. Xiang, *J. Alloys Compd.*, 2016, **686**, 564–570.

67 R. Rajaramakrishna, S. Karuthedath, R. V Anavekar and H. Jain, *J. Non. Cryst. Solids*, 2012, **358**, 1667–1672.

68 J. Sasai and K. Hirao, *J. Appl. Phys.*, 2001, **89**, 4548–4553.

69 H. Zeng, G. Chen, J. Qiu, X. Jiang and C. Zhu, *J. Non. Cryst. Solids*, 2008, **354**, 1155–1158.

70 J. M. P. Almeida, D. S. Da Silva, L. R. P. Kassab, S. C. Zilio, C. R. Mendonça and L. De Boni, *Opt. Mater. (Amst).*, 2014, **36**, 829–832.

71 T. Xu, F. Chen, X. Shen, S. Dai, Q. Nie and X. Wang, *Mater. Res. Bull.*, 2010, **45**, 1501–1505.

72 F. Cabello, S. Sanchez-Cortes and M. Jiménez de Castro, *J. Non. Cryst. Solids*, 2016, **445–446**, 110–115.

73 S. K. Ghoshal, A. Awang, M. R. Sahar and R. Ari, *J. Lumin.*, 2015, **159**, 265–273.

74 A. Awang, S. K. Ghoshal, M. R. Sahar, R. Arifin and F. Nawaz, *J. Lumin.*, 2014, **149**, 138–143.

75 E. S. Sazali, M. R. Sahar, S. K. Ghoshal, R. Arifin, M. S. Rohani and R. J. Amjad, *J. Non. Cryst. Solids*, 2015, **410**, 174–179.

76 A. Le Rouge, H. El Hamzaoui, B. Capoen, R. Bernard, G. Martinelli, C. Cassagne, G. Boudebs, M. Bouazaoui and L. Bigot, *Mater. Res. Express*, 2015, **2**, 1–10.

77 T. Hayakawa, K. Furuhashi and M. Nogami, *J. Phys. Chem. B*, 2004, **108**, 11301–11307.

78 S. Singla, O. P. Pandey and G. Sharma, *J. Non. Cryst. Solids*, 2019, **521**, 119481.

79 L. Reyes, P. Kassab, M. Eiji, C. Taveira, D. Mariano and J. Roberto, *Opt. Mater. (Amst).*, 2011, **33**, 1948–1951.

80 V. A. G. Rivera, Y. Ledemi, S. P. A. Osorio, D. Manzani, F. A. Ferri, S. J. L. Ribeiro, L. A. O. Nunes and E. Marega, *J. Non. Cryst. Solids*, 2013, **378**, 126–134.

81 E. S. Sazali, M. R. Sahar, S. K. Ghoshal, R. Arifin, M. S. Rohani and A. Awang, *J. Alloys Compd.*, 2014, **607**, 85–90.

82 H. Kim, D. Zhou, R. Wang, Q. Jiao, Z. Yang and Z. Song, *Ceram. Int.*, 2015, **41**, 2648–2653.

83 N. M. B. A. Herrera, S. Buchner, R.V. Camerini, C. Jacinto, *Opt. Mater. (Amst).*, 2016, **52**, 230–236.

84 J. A. M. Garcia, L. R. P. Kassab, R. K. Onmori, B. C. Lima, L. A. Gomez-Malagon and A. S. L. Gomes, *SBMicro 2016 - 31st Symp. Microelectron. Technol. Devices Chip Mt. co-located 29th SBCCI - Circuits Syst. Des. 6th WCAS - IC Des. Cases, 1st INSCIT - Electron. Instrum. 16th SForum - Undergraduate-Stude*, 2016, 8–10.

85 A. Herrera and N. M. Balzaretti, *J. Lumin.*, 2016, **181**, 147–152.

86 Y. Huang, W. Xiang, S. Lin, R. Cao, Y. Zhang, J. Zhong and X. Liang, *J. Non. Cryst. Solids*, 2017, **459**, 142–149.

87 N. Shasmal and B. Karmakar, *J. Non. Cryst. Solids*, 2017, **463**, 40–49.

88 G. Y. Shakhgil'dyan, M. Z. Ziyatdinova, V. V. Kovgar, S. V. Lotarev, V. N. Sigaev and I. V. Prusova, *Glas. Ceram.*, 2019, **76**, 121–125.

CHAPTER 3 EXPERIMENTAL TECHNIQUES

Overview

In the present chapter, details of material used followed by experimental procedure adopted to fabricate glasses and techniques used to characterize is presented. Incorporation of gold nanoparticles (AuNPs) in glass was done using three different ways adopting melt-quench technique. Structural studies on the prepared glasses were carried out by X-ray diffraction (XRD) and Fourier-Transform Infra-red (FTIR) spectroscopy. Morphological analysis was done using field emission scanning electron microscopy (FESEM) and high resolution transmission electron microscopy (HRTEM). Differential thermal analysis (DTA) was used to study the thermal behaviour. Density measurements were done using standard Archimedes principle. In addition, UV-Visible-NIR spectroscopy and Photoluminescence were used to study the linear optical properties whereas Z-scan experiment was used to evaluate the nonlinear optical behaviour of the glasses. Also, the theoretical model used to obtain the nonlinear parameters from Z-scan is presented here in brief.

3.1. Raw materials

In the present study, raw materials used for the preparation of glassy samples are: Bi_2O_3 (Sigma Aldrich, 99.9%), B_2O_3 (Sigma Aldrich, 99.9%), SiO_2 (Sigma Aldrich, 99.9%), AuNPs of size 10nm, 40nm and 100nm suspended in PBS (Sigma Aldrich, 99.9%), EuF_3 (Sigma Aldrich, 99.9%), Eu_2O_3 (Sigma Aldrich, 99.9%) and KSCN (Sigma Aldrich, 99.9%). All the mentioned chemicals were used as such without any further processing.

3.2. Sample preparation

In the present work, direct incorporation of AuNPs was done to prepare AuNPs dispersed glasses. In order to achieve better dispersion of AuNPs inside the glass matrix and reduce the loss of nanoparticle via evaporation during preparation of glasses, three different methods were tried. These three methods are modified form of standard melt quench technique.

To prepare glass samples dispersed with AuNPs, the measured amount of starting chemicals (Sigma Aldrich with 99.9% purity level) were mixed properly for half an hour using motor and pestle. All the chemicals were weighed using a digital balance having an accuracy of about ± 0.001 g. Then these blended powders were transferred to alumina crucible and was placed in a furnace which is able to attain maximum temperature of 1600 ^oC. The crucible containing the powder was heated in between 850-950 ^oC to achieve complete homogeneous melt. The melt was kept at the holding temperature for 15 min to ensure complete homogenization of melt. As our main motive was to incorporate AuNPs in the glass directly and to achieve this, following exercises were carried out while pouring the sample.

1. **Drop Casting Method (DCM):** After pouring the molten material on the brass mould, the measured amount of AuNPs were added with the help of a micropipette followed by transferring it to annealing furnace.
2. **Sandwich Method (SM):** Using this method, the sample was prepared by following three simple steps. In the very first step, half of the molten glass was first poured on the mould, then the measured amount of AuNPs were added over it. Finally, the remaining melt was poured on top of the cast product and placed for annealing.
3. **Melt Quenching at Room Temperature (RTM):** In this method, while mixing/crushing the starting material (Bi_2O_3 and B_2O_3) measured amount of AuNPs was poured in them and mixed thoroughly along with them. The entire mass was heated to designated temperature as mentioned above before casting.

Figure 3.1: Schematic representation of all the three methods followed for the sample preparation.

Fig. 3.1 shows the step by step illustration of all the three methods whereas Fig. 3.2 displays the pictorial representation the important steps involved for the addition of AuNPs. In order to remove the residual stresses induced in the glass due to non-uniform cooling, brass mould containing the glass was placed in an annealing furnace kept at 300-450 °C for 2-3 hours. Analytical balance was used to measure the post melt weight losses that comes out to be in good agreement with the prediction. The prepared glass samples were cut and polished after cooling. For polishing, the samples were first ground with the help of an electric machine using different grades of SiC abrasives and aluminium oxide with machine oil. The samples were mounted in a specially designed holder to maintain the two faces parallel. The polishing was done with cerium oxide to obtain flatness.

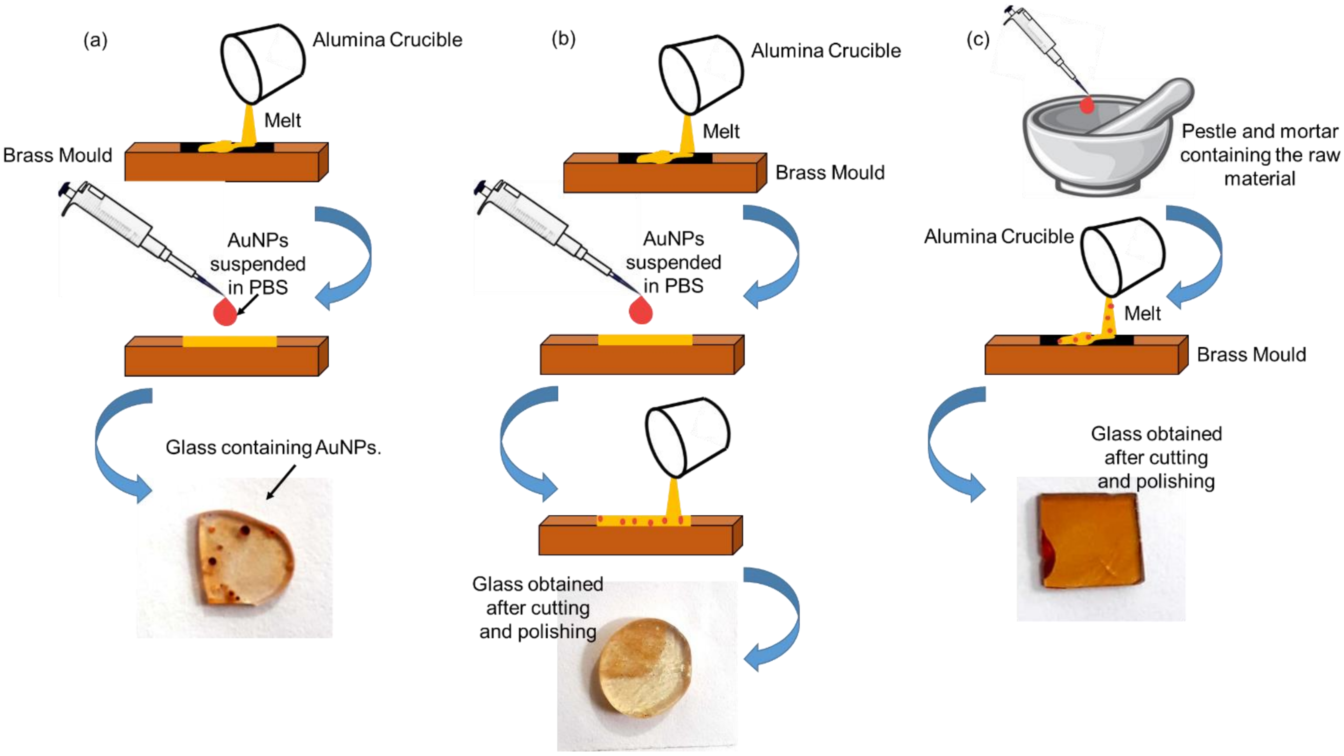

Figure 3.2: Pictorial representation of addition of AuNPs in (a) DCM, (b) SM and (c) RTM.

3.3. Characterization techniques

All the as prepared samples were characterized using various techniques to study the structural, morphological, thermal, physical, linear and nonlinear optical properties. The details of these techniques are given bellow:

3.3.1. X-ray diffraction

X-ray diffraction is a non-destructive technique used widely to identify the amorphous/crystalline nature (phases) of any material. In the present study, X-ray powder diffraction pattern of the samples have been recorded with the help of Panalytical Xpert Pro MPD using the Cu Kα radiation (λ = 1.5405 Å) in $10^o \leq 2\theta \leq 80^o$ range with a scan rate of 2^o/min. Powder samples having random orientation obtained after crushing the solid glass is analysed to ensure the scanning of all the crystallographic planes of the present phases by the X-ray beam. All the measurements were done at room temperature.

3.3.2. Fourier Transform Infrared spectroscopy

Fourier Transform Infrared Spectroscopy (FTIR) is another tool used here to detect the modification in basic structural units with the dispersion of metal nanoparticles. In this preferred technique of infrared spectroscopy, radiation from infrared region of electromagnetic spectrum is passed through the sample. Interaction between molecule and radiation is analysed after determining absorbed/transmitted portion of the radiation at particular energy. The absorbed energy corresponds to the vibrational frequency of the molecule that acts like a finger prints i.e. no two different materials can have same spectra.

FTIR spectra of the prepared glasses is collected at room temperature in absorption mode from 400-4000 cm^{-1} range using IRAffinity-1 (Shimadzu Co., Japan). The instrument is equipped with 'DRS-8000A Diffuse Reflectance Spectroscopy' powder sample assembly. A fine mixture of 1 mg of sample and 100 mg of KBr obtained in agate mortar was loaded on DRS attachment and the spectra was recorded. Each spectra was recorded with a resolution of 2 cm^{-1} and represents an average of 16 scans. Normalized spectrum of blank KBr of each sample was studied using IRsolution software.

3.3.3. Density measurement

Density is the measure of compactness of network structure. Using standard Archimedes principle, the density (ρ) of all the samples was measured with the help of following formula:

$$\rho = \frac{W_a}{W_a - W_b} \times \rho_b \tag{3.1}$$

where W_a and W_b are sample weight in air and immersion liquid, respectively. ρ_b is the density of Xylene used as immersion liquid. The weight of sample in air and liquid at room temperature are measured using sensitive digital microbalance (Shimadzu specific gravity kit). The measured weights are accurate upto ±0.001 mg. All the measurements were repeated five times in order to reduce experimental error. The average of these five measurements is the density of the sample whereas the standard deviation on five measurements is the relative error associated with them.

3.3.4. Field emission scanning electron microscopy

Morphology and distribution of metal nanoparticles inside the glassy matrix highly influence both linear as well as nonlinear optical properties of glass. Therefore, it is essential to carry out morphological studies. FESEM is a potential technique that provides magnified images of sample by scanning it with the beam of high energy electron. The interaction of electron with sample produces signals that include characteristic X-ray, secondary electrons, light (cathodoluminescence), back scattered electrons and transmission electrons that are detected by specialized detectors located at several places inside the machine. FESEM images were obtained using Zeiss Ultra 55 after scanning the solid sample pasted on aluminium stud with the help of a carbon tape. Further, elemental analysis was done using energy dispersive X-ray spectroscopy (EDS) analysis using EDS detector EDAX trident attached with the equipment.

3.3.5. High resolution transmission electron microscopy

Rare earth element present along with the metal nanoparticle forms a covering around them and prevents coagulation. This phenomena is difficult to observe through scanning electron microscopy and hence to visualize this transmission electron microscopy (TEM) was done. In TEM technique, a beam of electrons is passed through the ultra-thin specimen and the transmitted electrons are used to form and magnify image on an imaging device (fluorescent screen and layer of photographic film). The direct analysis of crystal structure can be done via high resolution TEM mode. TEM and HRTEM images were obtained using FEI Teenai G2 F20 operating at 200kV. The TEM specimens were prepared using fine powdered glass dispersed in ethanol that was mixed thoroughly with the help of ultrasonic vibrator in order to prevent coagulation of glassy particles. A drop of this dispersed solution was employed on a copper grid. This grid was dried completely under vacuum and was mounted on sample holder for further analysis.

3.3.6. Differential thermal analysis

Differential thermal analysis (DTA) is a thermo analytic method that provides the temperature difference between sample being observed and inert reference sample in heating/cooling cycle under specified conditions. The plot between obtained temperature difference and temperature/time is known as DTA curve. DTA curve provides significant information about thermal parameters such as glass transition, crystallization and melting temperature that in turns provides information about phase transformation. For this dissertation, thermal measurements are carried out using thermal analyser equipment NETZSCH DSC 404F3. The fine powdered sample weighing 50 mg are heated in alumina crucible from room temperature to 1100 °C at constant rate of 10 °C/min taking air as reference and N_2 as purging gas. The temperature measurement sensitivity of the equipment was ±1 ^oC. The exothermic peak in DTA curve denotes the glass crystallization whereas the endothermic peaks represents the glass transition temperature and melting temperature. ΔT is an important parameter that provides information about the glass stability and has been calculated using the following relation [1]:

$$\Delta T = T_x - T_g \tag{3.2}$$

where T_x and T_g are onset crystallization temperature and glass transition temperature. Moreover, according to the study carried out by Jiusti *et al.* [2] the best parameter to evaluate the thermal stability of glass is K_w given as follows.

$$K_w = \frac{T_x - T_g}{T_m} \tag{3.3}$$

where T_m is the melting point.

3.3.7. UV-Visible-NIR spectroscopy

Uv-Visible-NIR spectroscopy facilitates to examine the electronic transitions taking place in the molecule after passing the photons from Uv-visible and near infrared region of electromagnetic spectrum through the sample. It is a reliable technique that provides evidence about the transmission and absorption of electromagnetic radiation by the sample. In addition, useful information related to optical band gap and band structure of glassy material can be drawn from the absorption spectrum. Tauc's model for non-crystalline system is used here to further analyse the obtained optical data. According to this model, the absorption coefficient (α) and frequency (ν) is related as follows:

$$\alpha h\nu(w) = B[h\nu - E_o]^2 \tag{3.4}$$

where B is a constant and E_o is optical band gap whose value is calculated from linear extrapolation of $\sqrt{\alpha h\nu}$ v/s $h\nu$ plot to zero ordinate. Using following expression, refractive index (n) of glass can be measured [3],

$$\frac{n^2-1}{n^2+2} = 1 - \sqrt{\frac{E_o}{20}} \tag{3.5}$$

UV–Vis-NIR spectrophotometer (Carry 5000 UV-VIS-NIR) equipped with double beam is used to record the spectra in transmission mode in wavelength range 200–2500 nm at room temperature. The measurements were done on a well-polished solid sample using air as reference.

3.3.8. Photoluminescence

The phenomena of spontaneous light emission by a material under optical instigation is photoluminescence. More specifically, material re-emits a part of absorbed Uv-radiation at different wavelength in visible region of spectrum and the remaining part of the absorbed radiation ends up in heat. Presence of metal nanoparticles along with rare-earth elements results into new functionalities in the material that makes it necessary to investigate. Luminescence spectra of glass containing rare-earth along with AuNPs were recorded on Perkin Elmer LS55 spectrophotometer. It is equipped with Xe-flash lamp that acts as a source of radiation and a gated photomultiplier tube detector. All the emission spectra were recorded in the range of 450-800 nm at an excitation of 390 nm on well-polished glass samples at room temperature. Slit width was kept 15 nm in order to reduce noise.

3.3.9. Z-scan

This powerful technique enables to determine the sign and magnitude of coefficient of nonlinear absorption and nonlinear refractive index simultaneously. When a laser beam of high intensity interacts with material, self-focusing and defocusing of laser beam takes place due to variation in induced refractive index that leads to third order nonlinearity.

In a typical Z-scan experimental setup, a laser beam with a transverse Gaussian profile is focused by a lens. The sample is then moved along the axial direction of the focused beam in such a way that it passes through the focal point. At the focal point the sample experiences maximum pump intensity, which will progressively decrease in either direction. In the far field, the variation in transmission of laser intensity is measured using a photodiode as the sample translates through focal point. Z-scan is equipped with two configurations: open aperture (OA) Z-scan and closed aperture (CA) Z-scan based upon the absence and presence of aperture in front of photodiode, respectively as shown in Fig. 3.3. Nonlinear processes are distinguished in a Z–scan experiment based on their transmission response. For example, decrease in transmission at Z=0 in OA Z-scan is attributed to reverse saturable absorption (RSA) and increase in transmission at the focal point to saturable absorption (SA). Where the pre-focal dip and post-focal peak in CA Z-scan indicates the existence of positive nonlinear refractive index and vice versa.

In our experiment, Z-scan measurement was done by using a femtosecond laser (Tsunami-Ti: sapphire laser) operating at 80 MHz with 100 fsec pulse at 800 nm. A 10 cm focal length lens is used to focus the laser beam to 18 μm diameter (measured by knife-edge method). The sample is moved along Z-axis by mounting it on a stepper motor driven translation stage (Newport) with 0.1 µm step size. Both open and closed aperture measurements were carried out simultaneously without and with an aperture before two photo detectors (Hamamatsu), respectively.

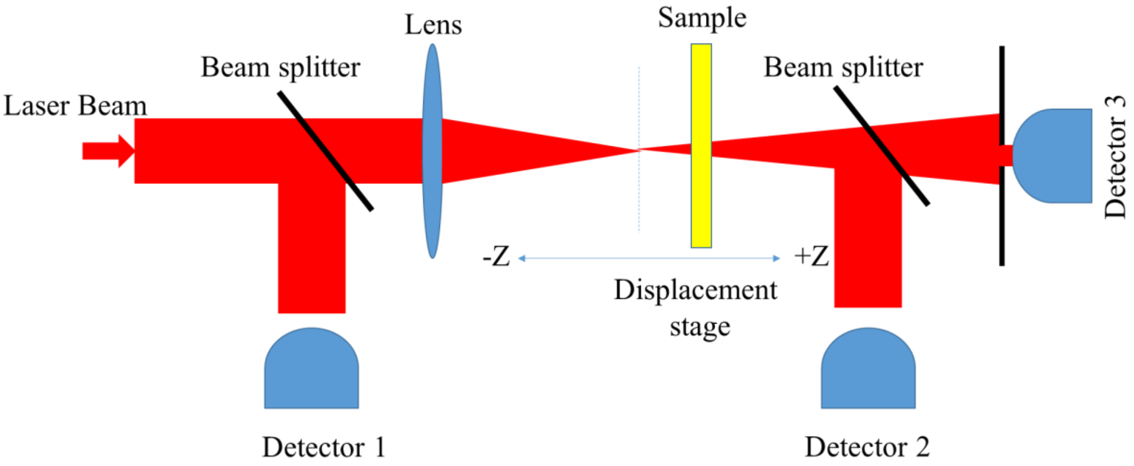

Figure 3.3: Experimental setup of Z-scan.

Theoretical analysis of Z-scan

The measured OA Z-scan curves are used to evaluate the contribution of nonlinear absorption. Due to absorption, the optical intensity (I) within the sample varies and it follows the equation:

$$\frac{dI}{dz} = -\alpha(I)I, \tag{3.6}$$

where 'z' is the thickness of the sample and '$\alpha(I)$' is the absorption coefficient which is a function of irradiance. In the absence of any nonlinearity, Eqn. (3.6) simplifies to Beer-Lamberts law of optical absorption [4]. In the present case, the intensity dependent absorption coefficient $\alpha(I)$ is given by [5]:

$$\alpha\,(I) = \alpha_o I + \beta_{eff} I, \tag{3.7}$$

where, α_0 is the linear absorption coefficient, I is the laser peak intensity and β_{eff} is the two photon absorption coefficient. Normally, the normalized transmittance in the Z-scan measurement is given by [6]:

$$T\,(Z) = \sum_{m=0}^{\infty} \frac{(-\alpha(I)L_{eff})^m}{(m+1)^{1.5}}, \tag{3.8}$$

where, L_{eff} is the effective thickness of the sample, which can be calculated from the real thickness and the linear absorption coefficient α_0, in the form of $L_{eff} = [1 - e^{\alpha_0 L}]/\alpha_0$. k =

2π/λ, here, k is the wave vector of the incident laser and λ is the wavelength. By fitting the experimental OA Z-scan data using Eqn. (3.8), two photon absorption coefficient (β_{eff}) is estimated.

In order to extract the nonlinear parameter from measured trend in CA Z-scan transmission, following theoretical expression given by Sheik Bahae *et. al.* [6] is used in this case and is given by:

$$T_1(x, \Phi_{0n}) = 1 + \frac{4x\Phi_{0n}}{(x^2+1)(x^2+9)}, \tag{3.9}$$

where, Φ_{0n} is the phase difference related to (2n+1)- order nonlinearity caused by the nonlinear material in the laser beam and can be obtained by fitting the CA Z-scan experimental data with Eqn. (3.10). The nonlinear refractive index is calculated using,

$$n_{2n}(\mathrm{m^2/W}) = \frac{\Phi_{0n}}{k I_0^n L_{eff}^n}, \tag{3.10}$$

Using the following equation (3.11) one can calculate the absolute values of third-order nonlinear susceptibility $\chi^{(3)}$

$$|\chi^{(3)}|\ (\mathrm{esu}) = \{(\mathrm{Re}\ \chi^{(3)})^2 + (\mathrm{Im}\ \chi^{(3)})^2\}^{1/2} \tag{3.11}$$

where Re $\chi^{(3)}$ and Im $\chi^{(3)}$ are the real and imaginary parts of the third-order nonlinear susceptibility given by Eqns. (3.12) and (3.13).

$$\mathrm{Re}\ \chi^{(3)}(\mathrm{esu}) = \frac{\varepsilon_o c^2 n_o^2}{\pi} n_2\ (\mathrm{m^2/W}) \tag{3.12}$$

$$\mathrm{Im}\ \chi^{(3)}\ (\mathrm{esu}) = \frac{\lambda \varepsilon_o c^2 n_o^2}{4\pi^2} \beta\ (\mathrm{m/W}) \tag{3.13}$$

The condition for TON material suitable for all optical switching applications is represented as follows [7]:

$$W = \frac{n_2 I_{max}}{\alpha\lambda} > 1 \tag{3.14}$$

$$T = \frac{\beta\lambda}{n_2} < 1 \tag{3.15}$$

where I_{max} is the threshold damage intensity for the glassy material.

References:

1 E. R. Shaaban, *Phys. B Phys. Condens. Matter*, 2011, **406**, 406–411.

2 J. Jiusti, D. R. Cassar and E. D. Zanotto, *Int. J. Appl. Glas. Sci.*, 2020, 1–10.

3 A. Awang, S. K. Ghoshal, M. R. Sahar and R. Arifin, *Opt. Mater. (Amst).*, 2015, **42**, 495–505.

4 S. B. Kolavekar, N. H. Ayachit, G. Jagannath, K. NagaKrishnakanth and S. Venugopal Rao, *Opt. Mater. (Amst).*, 2018, **83**, 34–42.

5 R. C. Fernández-Hernández, R. Gleason-Villagran, C. Torres-Torres, L. Rodríguez-Fernández, A. Crespo-Sosa, J. C. Cheang-Wong, A. López-Suárez, R. Rangel-Rojo, A. Oliver and J. A. Reyes-Esqueda, *J. Opt. (United Kingdom)*, 2012, **14**, 125203.

6 M. Sheik-Bahae, A. A. Said, T. H. Wei, D. J. Hagan and E. W. Van Stryland, *IEEE J. Quantum Electron.*, 1990, **26**, 760–769.

7 E. Cattaruzza, G. Battaglin, P. Calvelli, F. Gonella, G. Mattei, C. Maurizio, P. Mazzoldi, S. Padovani, R. Polloni, C. Sada, B. F. Scremin and F. D'Acapito, *Compos. Sci. Technol.*, 2003, **63**, 1203–1208.

CHAPTER 4 RESULTS AND DISCUSSION-I

Overview

The major focus of the present chapter is to optimize the fabrication conditions of borate glass to get better distribution of gold nanoparticles (AuNPs) inside the glass matrix to achieve enhanced optical efficiency of glass. Here, a comparative study is made on distribution of AuNPs inside the glassy matrix after adopting three different preparation methods discussed in previous section. Prepared glasses are characterized using XRD and FTIR to investigate the structural modifications. FESEM is carried out to study the morphological dependence of AuNPs inside the glass on method chosen for their preparation. Furthermore, thermal and physical properties are analysed using DTA and density measurements, respectively. Uv-Vis spectroscopy is employed to study the linear optical properties and the optical band structures. In the last, nonlinear behaviour using Z-scan technique is observed from which several nonlinear parameters were calculated to estimate the optical efficiency of the prepared glasses. All the results are discussed in light of distribution of AuNPs inside the glass.

4.1. Introduction

Glasses containing uniformly distributed metallic nanoparticles exhibit wide range of interesting properties like ultrafast nonlinear optical response, large third order nonlinear susceptibility, ultrafast optical switching in THz region etc. [1–5]. The problems faced for the production of glasses containing noble metal nanoparticles is its distribution inside the glass matrix where coagulation of nanoparticles and their losses due to high heat while fabricating the glasses is major challenge. In order to achieve relatively uniform distribution with least loss of AuNPs during fabrication, samples have been prepared using three different methods: drop casting method (DCM), sandwich method (SM) and melt quenching at room temperature (RTM). The details of these techniques is already described in the previous chapter. Also, the choice of glass composition plays an important role. The low melting point of bismuth borate glass provide appropriate environment for the reduction in coagulation and loss of nanoparticles while fabricating the glass [6]. In order to achieve uniform distribution of AuNPs in the glass matrix, for achieving better efficiency, these were directly discharged during preparation. This helps in avoiding the heat treatment to glasses [7]. Table 1 displays the composition of prepared glass samples. The samples obtained after cutting and polishing are shown in Fig. 4.1.

Table 4.1: Glass codes, method of preparation and glass composition.

Sample name	Method used for preparation	Percentage composition		Number of AuNPs	Size of AuNPs (nm)
		Bi_2O_3	B_2O_3		
BiB-DCM	DCM	30	70	3×10^{11}	10
BiB-SM	SM	30	70	3×10^{11}	10
BiB-RTM	RTM	30	70	3×10^{11}	10

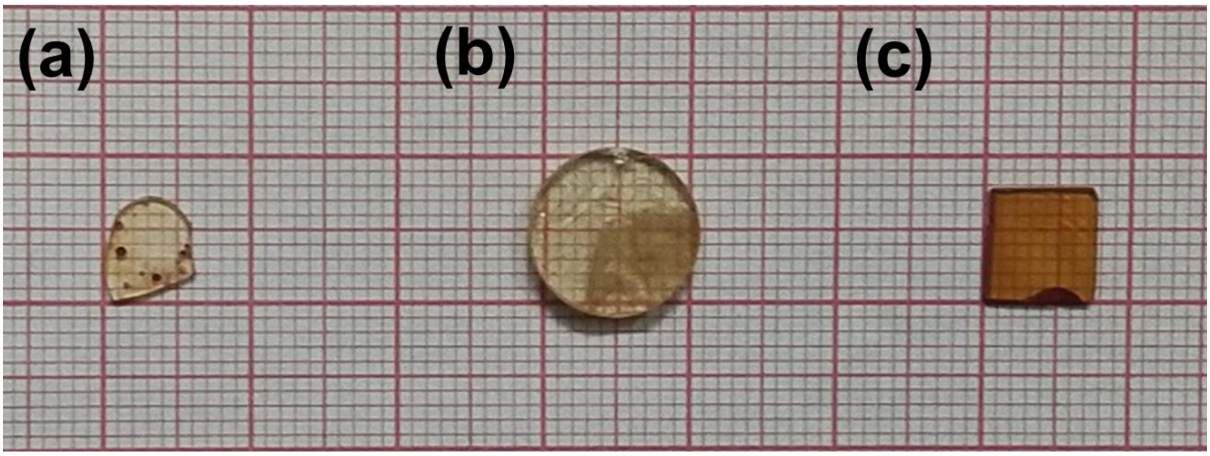

Figure 4.1: Pictures of samples prepared using (a) DCM, (b) SM and (c) RTM.

4.2. Structural analysis

4.2.1. X-ray Diffraction

The X-ray diffraction (XRD) pattern of the prepared glass sample is shown in Fig. 4.2. Broad humps in XRD pattern centred at 30° and 45° shows that the prepared glasses are non-crystalline, although additional AuNPs were incorporated.

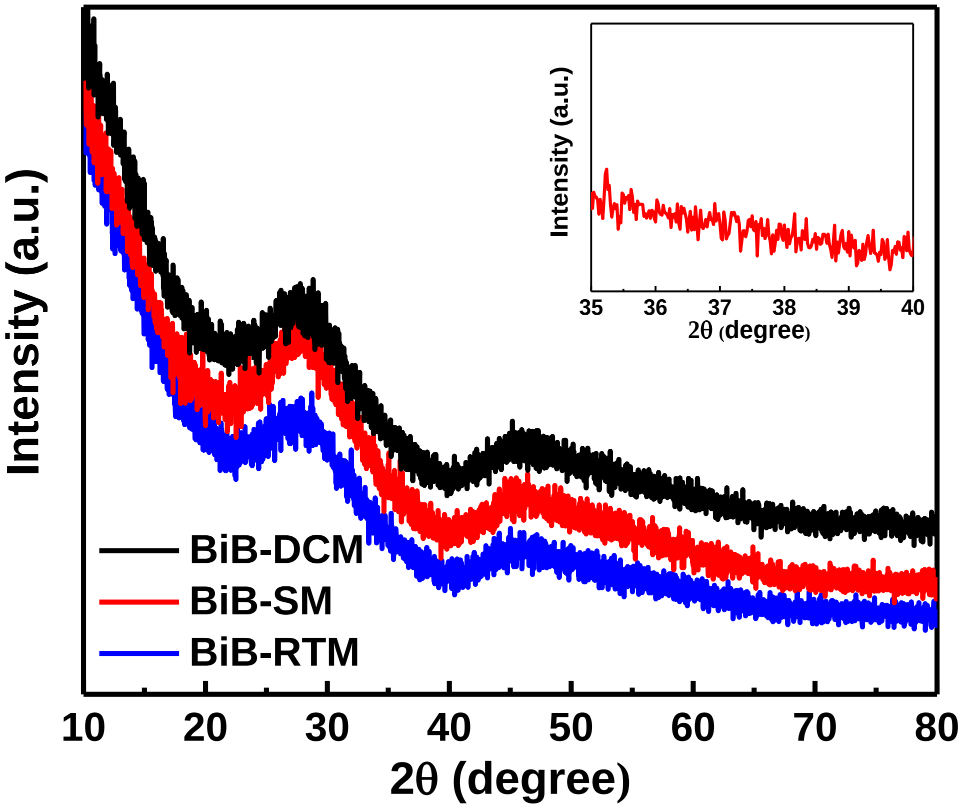

Figure 4.2: X-ray diffractrograph of the glass samples prepared using different techniques. Inset shows the magnified view of sample BiB-SM.

The presence of two broad humps confirm the existence of phase separation in the glass [8]. Moreover, the invariability in amorphous nature of glass even after the addition of AuNPs confirms that the direct addition of AuNPs does not induce any crystalline phase in the glass. Also, the volume of 3×10^{11} number of 10 nm size nanoparticle is 1.2×10^{-12} m^3. Rolland *et. al.* [9], have already reported that XRD cannot detect small nanoparticles in presence of a large amorphous material background. Also, the most prominent peak of gold for the (111) plane lies at 38° which is not seen in the inset of Fig. 4.2 that displays the XRD data from 35-40° for sample BiB-SM.

4.2.2. Fourier Transform Infrared Spectroscopy (FTIR)

The method used for the preparation of glass plays an important role in its structural and optical properties. In order to have insight of effect of the method chosen for the incorporation of AuNPs on the structure of all prepared glasses, FTIR spectra are recorded and are shown in Fig. 4.3. The spectra in the higher wavenumber range (above 1600 cm^{-1}) is not shown here as it gives the bands attributed to water groups and hydrogen bonding [10]. The absorption bands are found to be broad and asymmetric which is a result of distribution of local electronic/atomic environment and overlapping of individual bands. This signifies the amorphous state of the synthesised material [2]. Different bands obtained in spectra attributes to the bond vibration in specific structural group. Table 4.2 displays assignment of different bands.

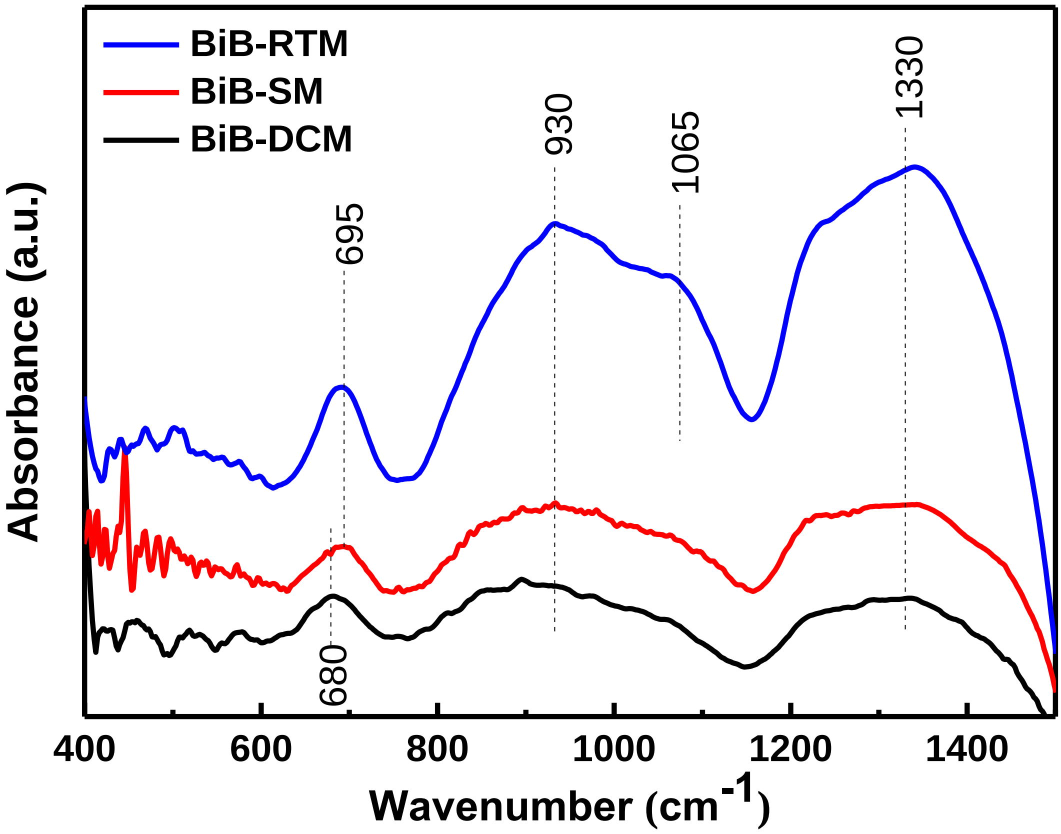

Figure 4.3: FTIR spectra of prepared glass samples in range 400-1500 cm^{-1}.

Infrared spectra of the present systems are dominated by broad peaks at 600-800 cm^{-1} and 800-1200 cm^{-1}, which are the main feature of B-O-B linkages in BO_3 triangles and B-O bond stretching of tetrahedral BO_4 units respectively [11–18]. The strong absorption band at 1200-1500 cm^{-1} is assigned to B-O bond stretching of trigonal BO_3 units such as metaborate chains and rings, pyroborate and orthoborate groups [19], indicating that the main glass network is formed of BO_4 and BO_3 units. Moreover, the weak peaks in the region of 400-600 cm^{-1} are attributed to the vibration of Bi-O bonds and overlapping of Bi-O bonds in BiO_6 octahedral units [12,20], thus confirming the co-existence of bismuth units in the boron network structure. The spectra of sample BiB-RTM contains an additional shoulder at 1065 cm^{-1} which concludes the formation of $[BO_4]^{-5}$ units in glass [21]. It is clear from the FTIR spectra that in BiB-RTM, the band around 1330 cm^{-1} becomes sharper and gets shifted towards higher wavenumber which supports the formation of non-bridging oxygens [22]. The formation of non-bridging oxygens results in the expansion of glass structure.

Table 4.2: Attribution of the infrared absorption bands positions of studied glass.

Wavenumber (cm^{-1})	**Assignment**
400-600	Bi-O vibrations in octahedral BiO_6
~695	Bending vibration of B-O-B in BO_3 triangles
~930	B-O bond stretching of tetrahedral BO_4 units
~1065	Asymmetric vibration in $[BO_4]^{-5}$ units
~1330	B-O bond stretching of trigonal BO_3 units

4.3. Morphological studies

4.3.1. Field Emission Scanning Electron Microscopy (FESEM)

In order to have insight of nanoparticle distribution in as prepared glass, it was first cut into different slices of approximately 2-3 mm thickness and then the images of different regions/layers have been taken. Fig. 4.4 represents the FESEM images of approximately all the sections of the glass. It could be clearly noticed that, method of preparation largely influence the morphology of AuNPs and their distribution inside the glass. Fig. 4.4(a), 4.4(b) and 4.4(c) displays the top, middle, and lower sections of the glass BiB-DCM whereas Fig. 4.4(d) and 4.4(e) represents the top and middle sections of glass BiB-SM. Fig. 4.4(f) is the magnified view of 4.4(e). In the last, Fig. 4.4(g) and 4.4(h) shows the morphology of different sections of glass BiB-RTM. Top layer of sample BiB-DCM shows intense distribution of nanoparticles where their intensity gets reduced as we move from top to bottom. For the glass sample prepared using DCM (BiB-DCM) the observed average size of AuNPs is 100 nm whereas AuNPs of 10 nm size were incorporated. This coagulation is due to very low mobility of AuNPs in DCM as they have got very less time to move from their respective place and got settled mostly in the top layer. This results into clustering and leads to the formation of distorted 100 nm size AuNPs. This low mobility can also be evidenced form Fig. 4.1 (a) where dark brown spots are seen at some random regions where the drops have been casted.

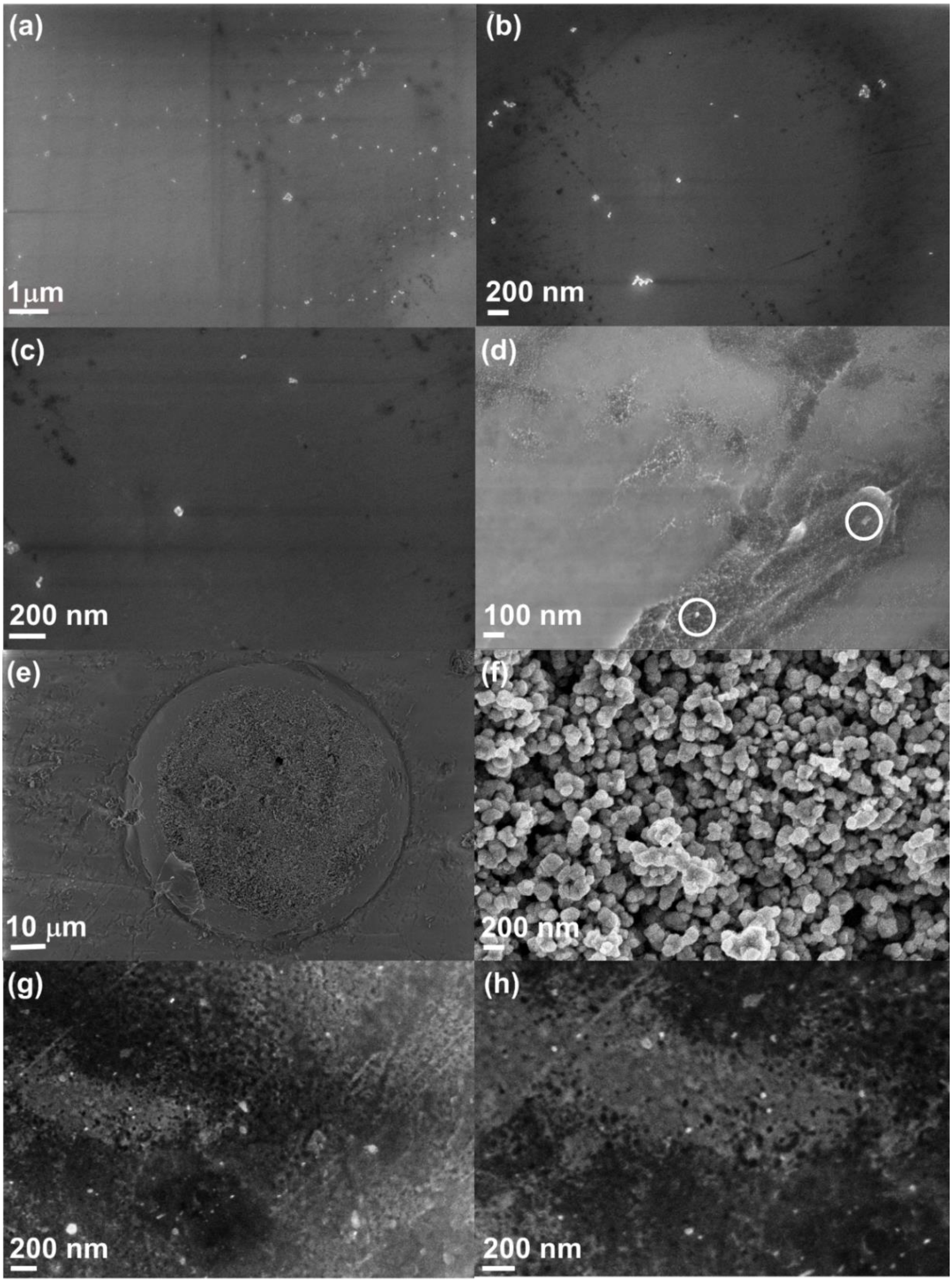

Figure 4.4: FESEM images of (a) top, (b) middle and (c) lower layer of BiB-DCM. (d) and (e) shows the top and middle layer of the sample prepared by BiB-SM and (f) is the magnified view of (e). (g) and (h) represents the microstructures at different region of BiB-RTM.

Now, for the sample BiB-SM, the particle distribution is highest in the middle section of glass. Top layer (Fig. 4.4(d)) shows the presence of few nanoparticles whereas, the middle section (Fig. 4.4(e)) displays a huge cluster of nanoparticles. For the sample prepared by SM (BiB-SM), the average size of the AuNPs comes out to be 200 nm. The formation of cluster/high intensity at the middle is attributed to low mobility of nanoparticles.

In case of the sample prepared by RTM (BiB-RTM) in which the AuNPs have been heated at 850 ^{o}C along with the premixed batch, the average particle size obtained is 50 nm (Fig. 4.4(g) and 4.4(h)). Several studies in the past have been done to check the dependence of physical properties on the size of the material, most often when it enters in the nanometres range and have been concluded that the size abruptly affect them [6,23]. Same is for the melting point i.e. a large reduction in the melting point have been reported when the size of the particle enters the nanometres range. Castro et. al. [24] have reported two main causes for such phenomena, one of them is the increase in surface atoms with the decrease in the size of the particle and second is the generation of particle-substrate interface with the reduction in the size. This increase in surface energy forces the phase transition temperature to follow scaling law i.e. varies with R^{-1}, where R is the radius of the nanoparticles. This phenomena leads in the decrease of the phase transition temperature (melting is a change in phase) of gold from 1064 ^{o}C to several lower ^{o}C depending upon R. We have used 10 nm sized AuNPs for the present study, and reduced melting point leads to splitting of AuNPs into Au atoms when they are heated along with the batch. At the time of annealing these Au atoms gets sufficient time to move and get coagulated to form nanoparticles of size 50 nm (Fig 4.4 (g) and (h)). It can be clearly seen from Fig. 4.4, that particle distribution is more uniform as compared to the distribution obtained for other two samples (BiB-DCM and BiB-SM) that gives it a uniform brown color. However, some coagulation of AuNPs still occurs in sample BiB-RTM.

4.4. Physical properties of the glass

As shown in Fig. 4.1, samples prepared using different techniques exhibit different colours. The appearance of such variation is due to variation in technique for their preparation where distribution of AuNPs inside the glass matrix plays important role. The presence of AuNPs in the sample prepared using SM and DCM can be clearly seen. Moreover, the color of these samples are light as compared to the sample prepared using RTM (Fig. 4.1). The appearance of dark brown color of the sample BiB-RTM is attributed to the homogeneous distribution of AuNPs inside the glassy matrix.

4.4.1. Density measurements

Dependence of density on the method chosen for the incorporation of AuNPs inside the glass can be clearly seen from Table 4.3. All the values are measured using Archimedes principle discussed in section 3.3.3. Evaluation of density provides the interesting information related to the structural changes occurring because of the change in recipe.

From Table 4.3, it is clearly observed that the density is maximum for BiB-RTM (6.04 g cm^{-3}) and approximately similar for BiB-SM (5.45 g cm^{-3}) and BiB-DCM (5.54 g cm^{-3}). Density is the measure of compactness of the structure. The observed lower density values for both BiB-SM and BiB-DCM is attributed to the fact that the added AuNPs are simply inserted to the host matrix after melting which are concentrated on a very small region (discussed with the help of FESEM images in the next section). Whereas the addition of AuNPs at the time of mixing and melting in BiB-RTM allows the Au atoms to enter into the glass and modify the structural units [7]. Moreover, the uniform distribution of AuNPs in BiB-RTM observed in FESEM images leads to occupation of free space and hence density increases. This observed structural compactness in BiB-RTM is in agreement with FTIR results. The dependence of density on the route of fabrication is in agreement with the reported literature [25,26].

Table 4.3: Measured physical, optical and thermal properties for the prepared glass samples.

Properties	**BiB-DCM**	**BiB-SM**	**BiB-RTM**
Physical properties			
Density, ρ (g cm^{-3}) ± 1%	5.54	5.45	6.04
Optical properties			
Optical band gap, E_o (eV)	3.31	3.23	3.08
Refractive index, n	2.36	2.34	2.38
Nonlinear absorption coefficient, β (m/W)	-	-	5.2×10^{-13}
Nonlinear refractive index, n_2 (m^2/W)	-	-	2.2×10^{-18}
Third order nonlinear susceptibility, $\lvert\chi^{(3)}\rvert$ (esu)	-	-	3.16×10^{-12}
Figure of merit, F	-	-	2.6
W	-	-	>1
T	-	-	1.3
Thermal Properties			
First glass transition temperature, T_{g1} (°C)	449	449	444
Second glass transition temperature, T_{g1} (°C)	-	-	499
Glass melting temperature, T_m (°C)	718	718	-

4.5. Thermal properties

4.5.1. Differential Thermal Analysis (DTA)

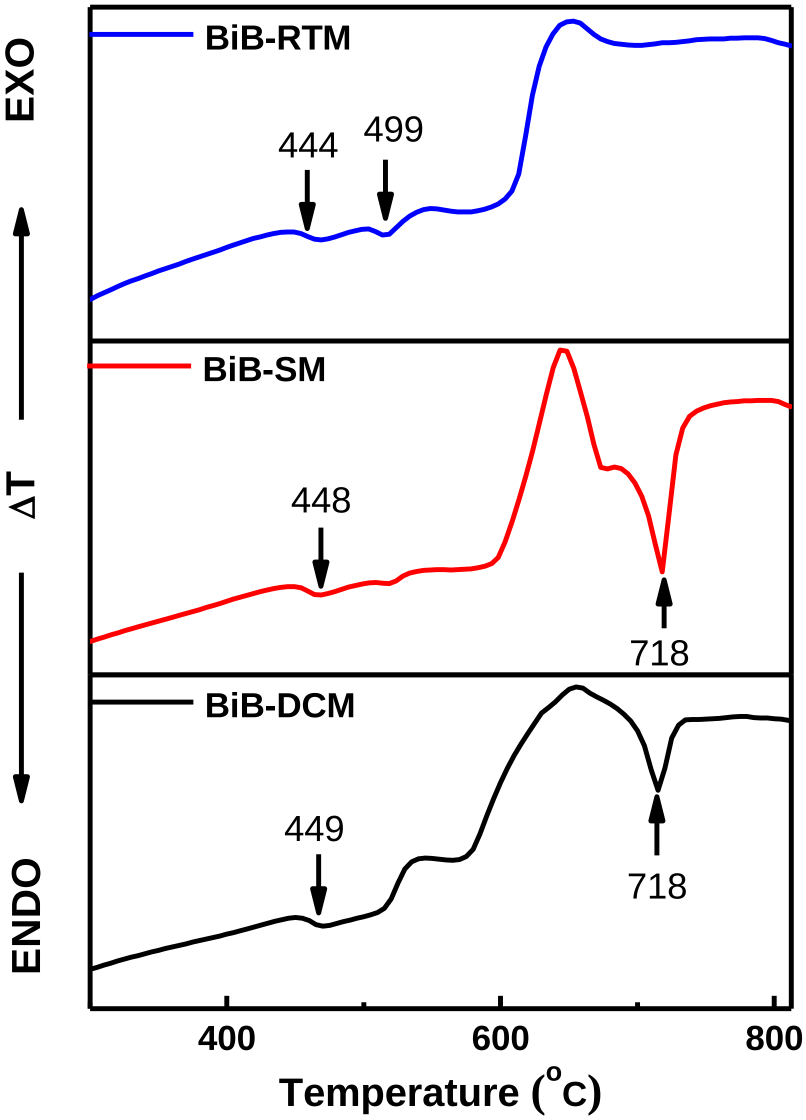

Figure 4.5: Thermogram of the prepared glass samples using above mentioned techniques.

Thermograms for all glasses recorded in the present study are shown in Fig. 4.5 and the corresponding thermal parameters (glass transition temperatures (T_g) and glass melting temperatures (T_m)) are represented in Table 4.3. It can be clearly seen that no change has been observed in the thermal parameters for sample BiB-DCM and BiB-SM. In both of these systems AuNPs were added after melting the batch and AuNPs have not changed their thermal properties i.e. T_g (449 °C) and T_m (718 °C) remain same for both the systems. Whereas, for sample BiB-RTM considerable changes have been observed. Appearance of two glass transition temperatures (T_{g1} = 444 °C and T_{g2} = 499 °C) has introduced phase separation in the glassy matrix which is attributed to the formation of glass nanocomposities [27]. But no such phase separation has been observed in other studied systems (BiB-DCM and BiB-SM) as the AuNPs have been added after melting the glass matrix constituents and hence in that case AuNPs are not able to penetrate into the glass structure. Therefore, they do not play any role in thermal properties of the glass much. Moreover, the presence of AuNPs along with the batch while melting of BiB-RTM, shifts the melting point to the higher temperature.

4.6. Optical properties

4.6.1. UV-Visible-NIR Spectroscopy

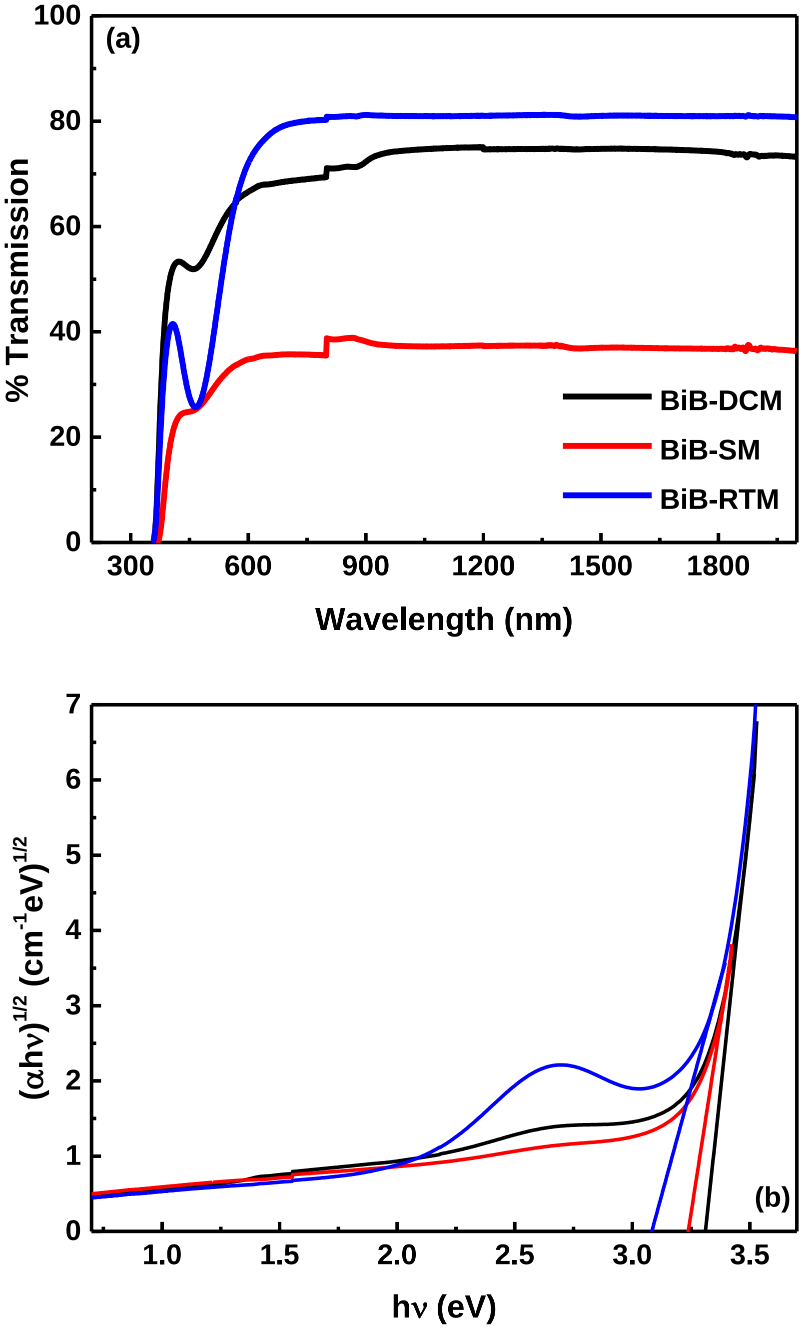

Figure 4.6: (a) Transmission spectra of prepared glass samples (b) Tauc's plots of $(h\nu\alpha)^{1/2}$ v/s hν for the measurement of optical band gap.

The variation in percentage transmission as a function of wavelength observed for glasses prepared by DCM, SM and RTM is shown in Fig. 4.6. It is clear that transmission is maximum for BiB-RTM and minimum for BiB-SM which is attributed to high particle density observed in FESEM results (section 4.4.1). A dip around 465 nm in all the samples is attributed to the presence of Bi content [28]. No surface plasmon resonance peak has been observed for the samples as the concentration or particle density of AuNPs in BiB-DCM and BiB-RTM are very less on the other hand for BiB-SM the particle size obtained from FESEM is 200 nm which are unable to show any local plasmon resonances.

The optical band gap calculated using Tauc's model (discussed in section 3.3.6.) for the prepared sample are displayed in table 4.2. The obtained band gap values is highest for sample BiB-DCM and is lowest for BiB-RTM. In literature, the reported value of optical band gap for $30Bi_2O_3:70B_2O_3$ glass system is 3.33 eV which is nearly same values as been calculated for glasses BiB-DCM and BiB-SM [29]. This again confirms the least role played by AuNPs in structural modification of the glass when prepared using DCM and SM methods. Also, heating of AuNPs along with the starting materials to prepare the glass reduced band gap value of BiB-RTM that confirms the active participation of AuNPs in structural modification. Presence of AuNPs results into the formation of non-bridging oxygens in the glass matrix that shifts the band edge to lower energies [30]. Also, the lower value of band gap indicates the increase in disorderness and decrease in rigidity of the glass [31].

4.6.2. Z-Scan

OA and CA Z-scan measurements are performed on all the sample to observe the nonlinear behaviour of the sample and the fitting is done according to the theory proposed by Sheik Bahae et al. [32] (discussed in section 3.3.8.) to get the values of nonlinear absorption coefficient from OA Z-scan and nonlinear refractive index from CA Z-scan. The non-uniformity observed for samples BiB-DCM and BiB-SM in Fig. 4.1 acts as scattering centres results into scattering of laser light and hence poor or no signal is obtained at the photodiode for both OA as well as CA measurements. Inset of Fig. 4.7 (a) and (b) shows the obtained Z-scan data for BiB-DCM glass sample. Although, for sample BiB-RTM due to uniform distribution of AuNPs inside the glass, no such scattering is observed. Fig 4.7 (a) and (b) displays the obtained OA and CA Z-scan data for sample BiB-RTM respectively, where the experimental data is represented by solid squares and the fit is represented by solid line. After fitting the obtained data for sample BiB-RTM, calculated value of nonlinear absorption coefficient is 5.2×10^{-13} mW^{-1} and the value of refractive index is 2.2×10^{-18} m^{2}W^{-1}. High value of nonlinear third order susceptibility (χ^3) and figure of merit given in table 4.2. makes these uniformly AuNPs dispersed glasses highly suitable for optical applications [33].

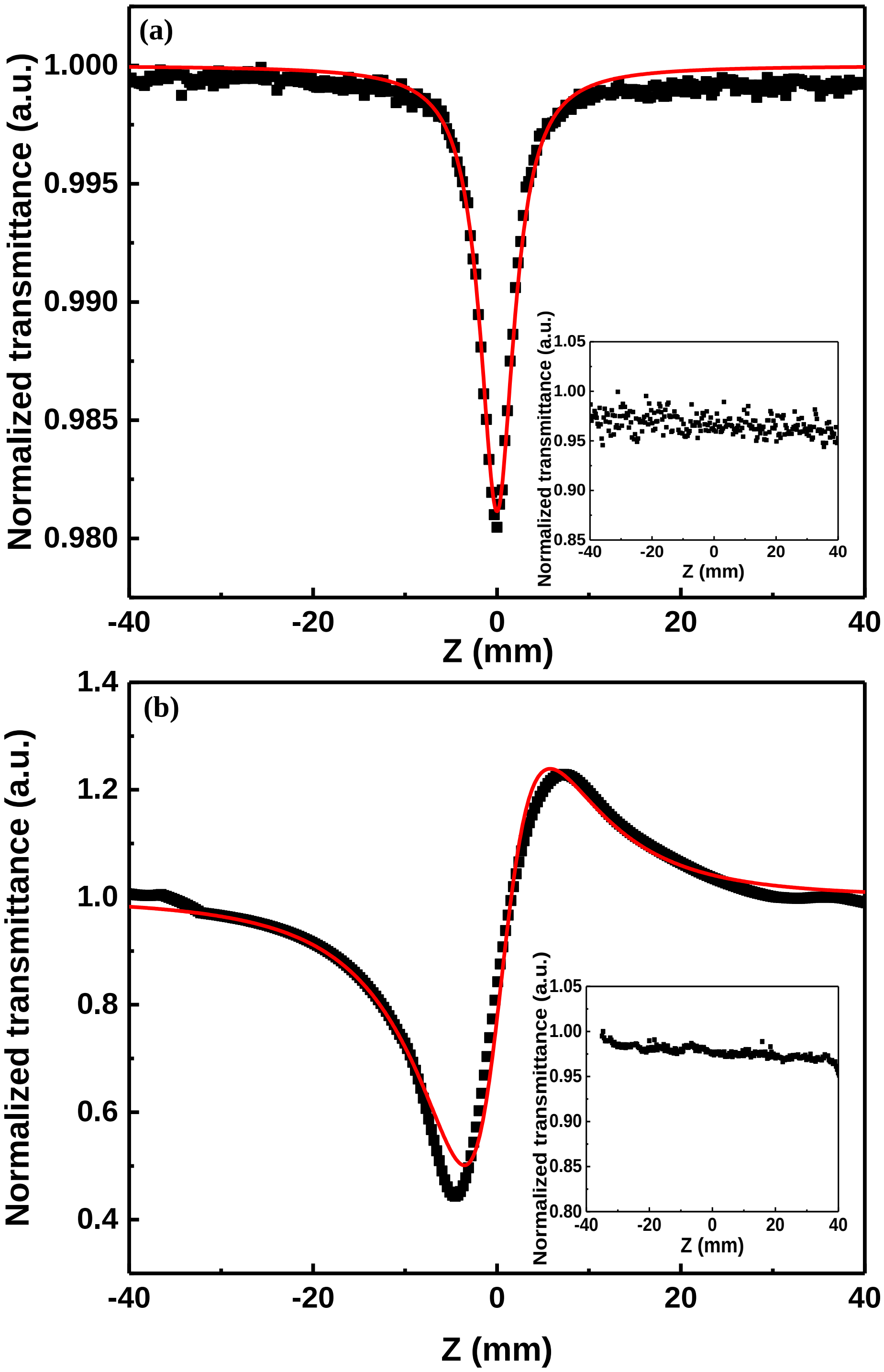

Figure 4.7: Z-scan measurements taken in (a) OA and (b) CA mode. Solid squares represents the experimental data whereas the theoretical fit is represented by solid line. Inset of (a) and (b) are the OA and CA Z-scan data of BiB-DCM.

References:

1 H. Zeng, G. Chen, J. Qiu, X. Jiang and C. Zhu, *J. Non. Cryst. Solids*, 2008, **354**, 1155–1158.

2 E. Culea, I. Vida-simiti, G. Borodi, E. Nicolae, R. Stefan and P. Pascuta, *Ceram. Int.*, 2014, **40**, 11001–11007.

3 A. L. Stepanov, in *Silver Nanoparticles*, 2007, pp. 93–121.

4 D. Manzani, J. M. P. Almeida, M. Napoli, L. De Boni, M. Nalin, C. R. M. Afonso, S. J. L. Ribeiro and C. R. Mendonça, *Plasmonics*, 2013, **8**, 1667–1674.

5 S. Singla, V. Gopal, N. Mahendru, S. S. Prabhu, M. Falconieri and G. Sharma, *Opt. Mater. (Amst).*, 2017, **72**, 91–97.

6 P. Buffat and J.-P. Borel, *Phys. Rev. A*, 1976, **13**, 2287–2298.

7 E. Nicolae, P. Pascuta, M. Pustan, D. R. Tamas-gavrea, L. Pop and I. Vida-simiti, *J. Non. Cryst. Solids*, 2015, **408**, 18–25.

8 J. E. Shelby, *Structures of glasses*, 2007.

9 S. Rolland, M. Tribet, P. Jollivet, C. Jégou, V. Broudic, C. Marques, H. Ooms and P. Toulhoat, *J. Nucl. Mater.*, 2013, **433**, 382–389.

10 Y. B. Saddeek, *J. Non. Cryst. Solids*, 2017, **40**, 545–553.

11 H. Doweidar and Y. B. Saddeek, *J. Non. Cryst. Solids*, 2009, **355**, 348–354.

12 Y. B. Saddeek and M. S. Gaafar, *Mater. Chem. Phys.*, 2009, **115**, 280–286.

13 S. Baccaro, Monika, G. Sharma, K. S. Thind, D. Singh and A. Cecillia, *Nucl. Instruments Methods Phys. Res. Sect. B Beam Interact. with Mater. Atoms*, 2007, **260**, 613–618.

14 Y. D. Yiannopoulos, G. D. Chryssikos and E. I. Kamitsos, *Phys. Chem. Glas.*, 2001, **42**, 164–172.

15 E. I. Kamitsos and G. D. Chryssikos, *Solid State Ionics*, 1998, **105**, 75–85.

16 E. I. Kamitsos, M. A. Karakassides and G. D. Chryssikos, *J. Phys. Chem.*, 1987, **91**, 1073–1079.

17 G. D. Chryssikos, L. Liu, C. P. Varsamis and E. I. Kamitsos, *J. Non. Cryst. Solids*, 1998, **235–237**, 761–765.

18 E. I. Kamitsos, A. P. Patsis, M. A. Karakassides and G. D. Chryssikos, *J. Non. Cryst. Solids*, 1990, **126**, 52–67.

19 Manupriya, K. S. Thind, G. Sharma, V. Rajendran, K. Singh, A. V. G. Devi and S. Aravindan, *Phys. Status Solidi Appl. Mater. Sci.*, 2006, **203**, 2356–2364.

20 D. Saritha, Y. Markandeya, M. Salagram, M. Vithal, A. K. Singh and G. Bhikshamaiah, *J. Non. Cryst. Solids*, 2008, **354**, 5573–5579.

21 A V Egorysheva, V. D. Volodin and V. M. Skorikov, *Inorg. Mater.*, 2008, **44**, 1261–1265.

22 N. N. Ahlawat, P. Agamkar, N. Ahlawat, A. Agarwal, Monica and Rekha, *Adv. Mater. Lett.*, 2013, **4**, 71–73.

23 G. Schmid and B. Corain, *Eur. J. Inorg. Chem.*, 2003, **2003**, 3081–3098.

24 R. P. A. T. Castro, R. Reifenberger, E. Choi, *Phys. Rev. B*, 1990, **42**, 8548–8557.

25 G. Kaur, G. Pickrell, N. Sriranganathan, V. Kumar and D. Homa, *J. Biomed. Mater. Res. - Part B Appl. Biomater.*, 2016, **104**, 1248–1275.

26 D. Carta, D. M. Pickup, J. C. Knowles, I. Ahmed, M. E. Smith and R. J. Newport, *J. Non. Cryst. Solids*, 2007, **353**, 1759–1765.

27 G. Senthil Murugan, *J. Non. Cryst. Solids*, 2001, **279**, 1–13.

28 M. Peng, C. Zollfrank and L. Wondraczek, *J. Phys. Condens. Matter*, 2009, **21**, 285106.

29 S. B. Mallur, T. Czarnecki, A. Adhikari and P. K. Babu, *Mater. Res. Bull.*, 2015, **68**, 27–34.

30 S. B. Kolavekar, N. H. Ayachit, G. Jagannath, K. NagaKrishnakanth and S. Venugopal Rao, *Opt. Mater. (Amst).*, 2018, **83**, 34–42.

31 G. Jagannath, B. Eraiah, K. NagaKrishnakanth and S. Venugopal Rao, *J. Non. Cryst. Solids*, 2018, **482**, 160–169.

32 M. Sheik-Bahae, A. A. Said, T. H. Wei, D. J. Hagan and E. W. Van Stryland, *IEEE J. Quantum Electron.*, 1990, **26**, 760–769.

33 D. Compton, L. Cornish and E. Van Der Lingen, *Gold Bull.*, 2003, **36**, 51–58.

CHAPTER 5 RESULTS AND DISCUSSION-II

Overview

Size and number of AuNPs present in the glass matrix plays a crucial role in variation in their optical behaviour. For the optimization of above-mentioned parameters, study has been categorized into two sections, (i) effect of number of AuNPs with uniform size i.e. 10 nm; and (ii) effect of size of AuNPs with 3×10^8 number of AuNPs. Glass samples prepared using RTM are characterized using XRD, FTIR, FESEM, density measurements and DTA in order to identify their structural, morphological and thermal behaviour. XRD confirms the amorphous nature whereas FTIR elucidates that BO_3 and BO_4 are the major component of glass structure. FESEM micrographs evidences the morphological dependence on number and size of incorporated AuNPs. Shielding of bonds by AuNPs have been confirmed by shifting T_g to higher temperature after gold incorporation. Further this effect is found to be dependent on number and size of AuNPs. AuNPs dispersed glasses are found to be optically efficient for several optical devices after employing UV-Vis spectroscopy and Z-scan measurements. Moreover, the impact of Bi_2O_3 concentration (30, 35 and 40 mol%) on structural, thermal and optical behaviour of glass samples incorporated with AuNPs (same number and size) is discussed.

5.1. Introduction

Glasses dispersed with AuNPs find several applications in the field of therapeutics, biomarkers, diagnostics and optical sensing [1–6]. Most of these applications, arises due to their linear and nonlinear optical response. Large enhancement in optical response of any random material containing AuNPs is associated with strong absorption and scattering of light by nanoparticles in visible and IR region [7]. Collective oscillations of free electrons of metal nanoparticles (known as surface plasmon resonance; SPR) inside the glassy matrix are the origin of this optical enrichment. Further, these SPRs are intrinsic function of size, shape and concentration of nanoparticles [8,9]. Apart from optical behaviour of material, other properties like physical appearance, thermal stability, density, conductivity etc. also show a significant dependence on the size, shape and concentration of the AuNPs [10,11]. In order to empower the optical performance of a material for a specific application, it is necessary to tune the band width of SPR that can be achieved simply by varying particle size, concentration and shape of NPs.

In addition to the properties (size, shape and concentration) of nanoparticles, the refractive index of surrounding glass matrix also influences the peak position, width and amplitude of plasmonic properties of nanoparticles which is an intrinsic function of the composition of glass [12]. Therefore, it becomes necessary to study the effect of size, shape and composition of nanoparticles along with the role of glass composition on optical performance.

5.2. Effect of concentration

In order to study the effect of AuNPs concentration on structural, thermal and optical properties glasses of composition $30Bi_2O_3:70B_2O_3$ are prepared by RTM process (section 3.2.) to get uniform distribution of AuNPs inside the glass. The details of composition of prepared glasses along with the sample codes are given in Table 5.1. Fig. 5.1 shows the samples obtained after cutting and polishing.

Table 5.1: Composition of the prepared glasses.

Sample label	**Percentage Composition**		**Number of AuNPs**	**Size of AuNPs (nm)**
	Bi_2O_3	**B_2O_3**		
BiB	30	70	-	-
BiB7	30	70	3×10^7	10
BiB8	30	70	3×10^8	10
BiB9	30	70	3×10^9	10

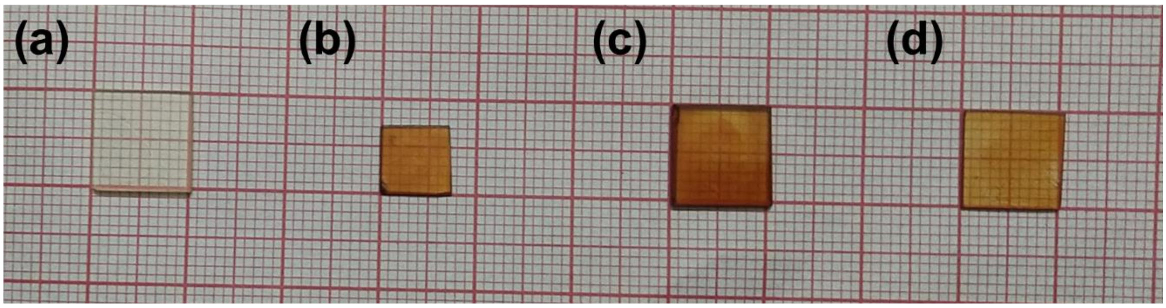

Figure 5.1: Picture of sample (a) BiB, (b) BiB7, (c) BiB8 and (d) BiB9 obtained after cutting and polishing.

5.2.1. Structural analysis

5.2.1.1. X-ray diffraction:

Fig. 5.2 shows the X-ray diffraction spectra of prepared glass samples. The broad hump in the spectra confirms the expected amorphous nature of the samples even after the addition of AuNPs.

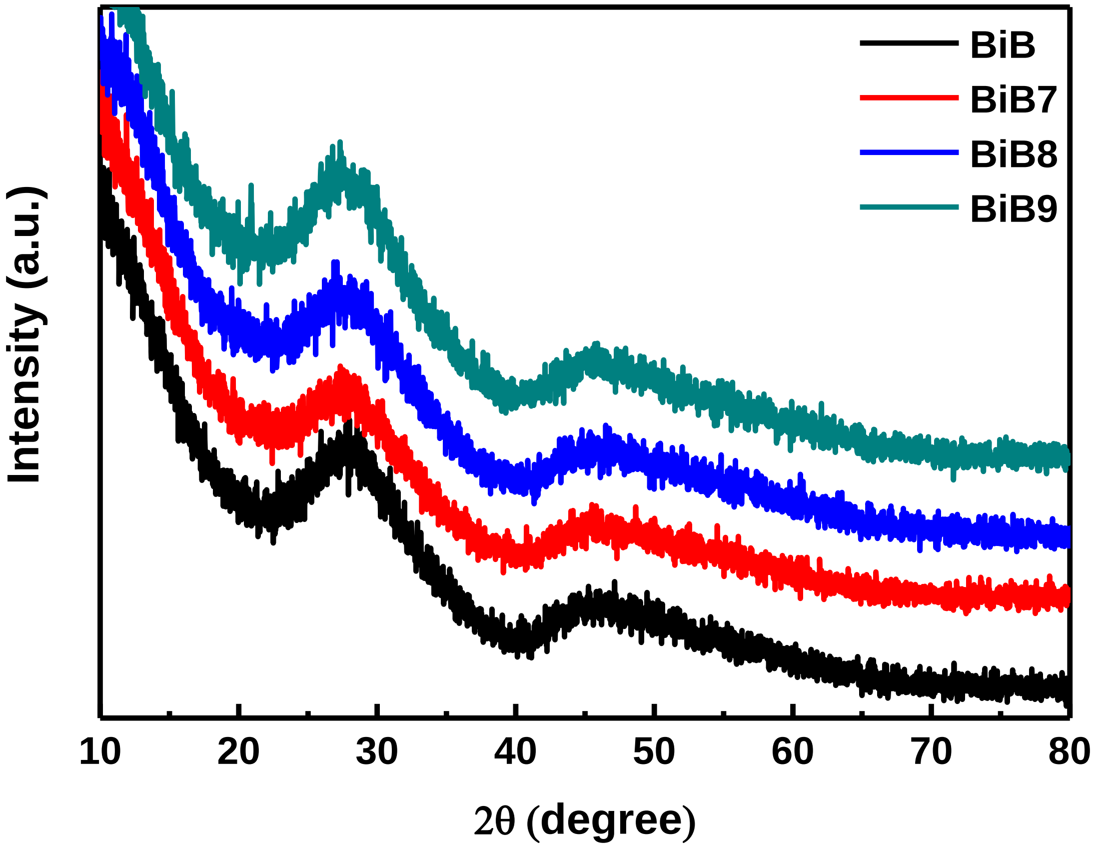

Figure 5.2: XRD spectra of different glass samples (bare and containing different concentrations of AuNPs).

5.2.1.2 Fourier Transform Infrared spectroscopy:

In order to have insight of structure of as prepared glasses due to change in AuNPs concentration FTIR spectra were recorded and shown in Fig. 5.3. Generally, infrared spectra of borate glasses show three main groups of absorption bands: (i) Around 640 -740 cm^{-1} attributed to bond bending vibrations of B-O-B linkages in BO_3 triangles [13–16], (ii) Between 800-1200 cm^{-1} to B-O bond stretching of tetrahedral BO_4 units [17–20] and (iii) Between 1200-1500 cm^{-1} attributed to B-O bond stretching of trigonal BO_3 units such as metaborate chains and rings, pyroborate and orthoborate groups [21].

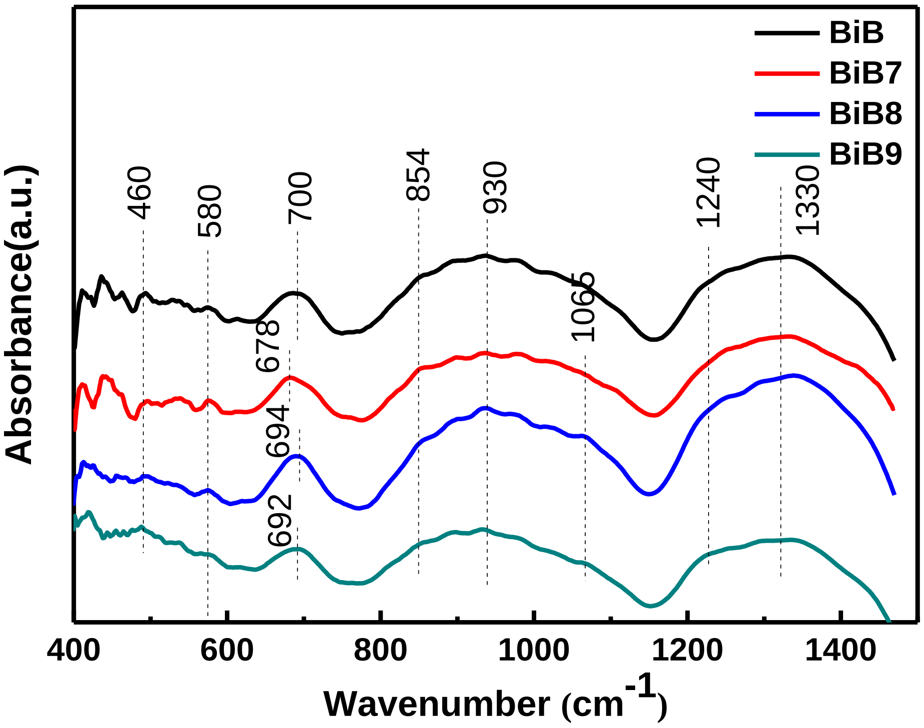

Figure 5.3: FTIR spectra of all the prepared glasses in the range of 400-1500 cm^{-1}.

For the prepared glass sample without AuNPs (BiB) peaks centered at 460 cm^{-1} and 580 cm^{-1} in the region 400-600 cm^{-1} are attributed to the vibration of Bi-O bonds and overlapping of Bi-O bonds in BiO_6 octahedral units [17,22]. In the region 600-700 cm^{-1}, vibration of B-O-B in BO_3 triangles is confirmed by the presence of peak at 690 cm^{-1} [13,21]. A shoulder around 854 cm^{-1} appears due to symmetrical stretching vibrations of Bi-O linkage in BiO_3 units. The presence of clear peak at 930 cm^{-1} (for BiB) confirms the B-O bond stretching of tetrahedral BO_4 units [17,23] while a broad band centred at 1330 cm^{-1} (for BiB) verifies the stretching vibrations of B-O units of trigonal BO_3 [13,24]. A clear shoulder at 1240 cm^{-1} for all the samples determine occurrence of $(BO)^{3-}$ units [22]. On comparison of structural changes for all the prepared samples it is seen (Fig. 5.3) that no prominent change has been observed. Whereas, for the sample BiB8 and BiB9 a new peak at 1065 cm^{-1} is observed which concludes the formation of $[BO_4]^{-5}$ units [24]. It is clear from the FTIR spectra that with the addition of AuNPs the band around 1240cm^{-1} becomes sharper and gets shifted towards higher wavenumber which supports the formation of non-bridging oxygens [25].

5.2.2. Morphological studies

5.2.2.1. Field emission scanning electron microscopy:

The FESEM micrograph of glass without AuNPs (BiB) shown in Fig. 5.4 (a) presents the surface of glass matrix. Fig. 5.4 (b)-(d) presents the micrographs of samples BiB7, BiB8 and BiB9, respectively and shows the presence of AuNPs whose size varies with concentration of AuNPs. The energy dispersive X-ray spectrum obtained for sample BiB7 is shown in Fig. 5.4 (e) that confirms the presence of Bismuth, Gold and Oxygen in the glass. The calculated size of AuNPs in the three samples with increasing gold concentration is about, 2 nm (BiB7), 30 nm (BiB8) and 100 nm (BiB9), respectively. As discussed in section 4.5.1, melting point of gold gets reduced when it enters the nano range. During the synthesis of glass sample, the temperature is very high that results into splitting of 10 nm size AuNPs into Au atoms [26]. As Au^0 atoms are not stable they start interacting with other Au^0 atoms resulting in the formation of small sized AuNPs. This whole process of formation of AuNPs in the glass may not take place while melting only but also extends during the annealing of the glass. In the present study, melting occurs because of the absence of refractory materials that can protect the AuNPs from high temperature [27]. The size of the particle after coagulation depends upon the concentration of the AuNPs. The increased concentration results in the formation of more Au atoms and hence more coagulation resulting in the increase of the size of AuNPs. For the sample with very low concentration of the AuNPs (BiB7), nanoparticles of very small size (2nm) are formed. On the other hand for the sample with highest concentration (BiB9) due to coagulation bigger particles (100 nm) are formed. This coagulation further reduces the particle density with the increase in the concentration of AuNPs. The nanoparticle density (particles/μm^2) estimated from FESEM images, is 23, 5 and 1 for the three samples BiB7, BiB8 and BiB9, respectively. As nanoparticle density is very low for the samples BiB8 and BiB9, therefore it is not possible to quantify the size from XRD spectrum. For sample BiB7, though the particle density is higher, the particle size is very small, and it is below the detectable limit of the XRD technique. The fact that XRD cannot detect these nanoparticles in presence of a large amorphous material background was already reported in the literature [28].

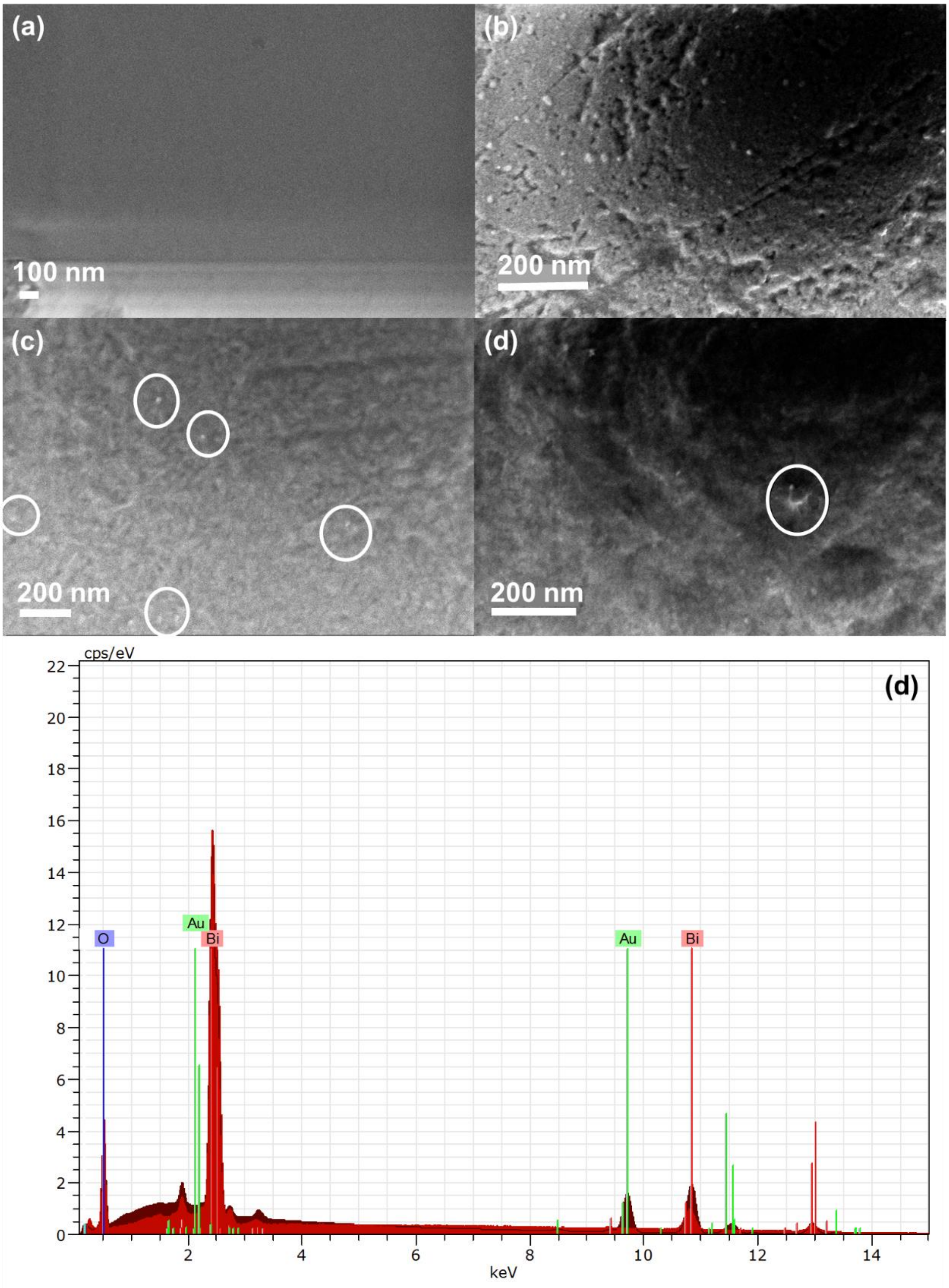

Figure 5.4: FESEM images of samples (a) BiB, (b) BiB7 (c) BiB8 and (c) BiB9. AuNPs locations are highlighted with circles. (e) shows the presence of different elements in BiB7.

5.2.3. Physical properties of glass

A colour change in sample is observed in Fig. 5.1 from light yellow for undoped glass to darkest brown for sample containing lowest concentration of AuNPs. The intensity of the colour decreases with the increase in concentration of AuNPs, which is attributed to the decrease in particle density as observed in FESEM micrographs.

5.2.3.1. Density measurements

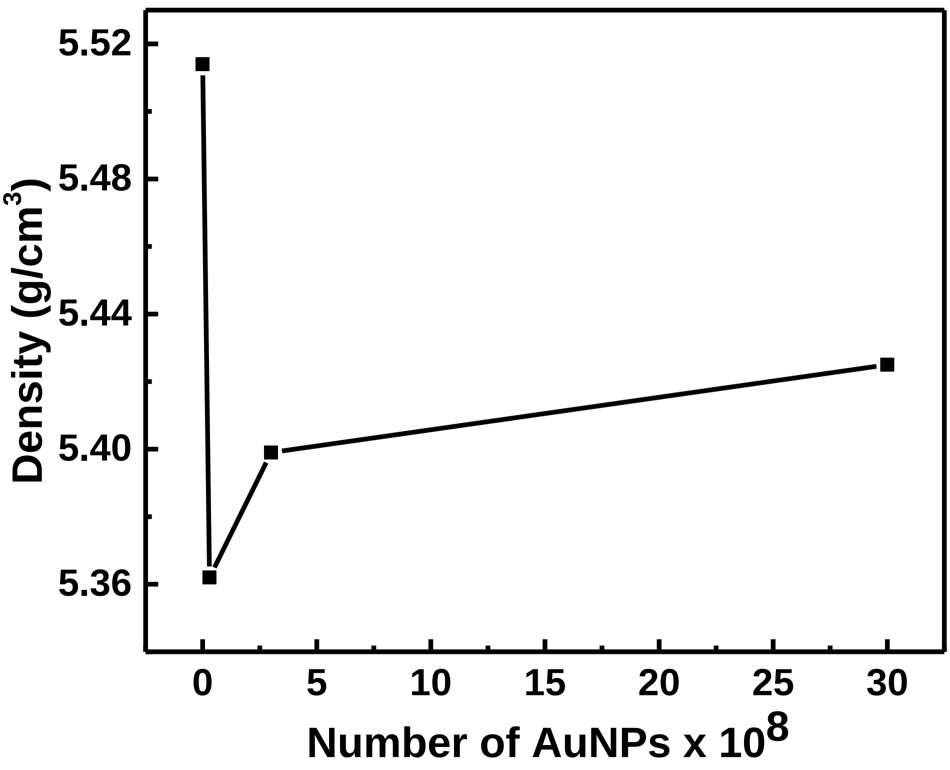

Figure 5.5: Density dependence on gold concentration.

Table 5.2: Measured physical, optical and thermal properties for the prepared glass samples.

Properties	**BiB**	**BiB7**	**BiB8**	**BiB9**
Physical properties				
Density, ρ (gcm^{-3}) ± 1%	5.51	5.36	5.39	5.42
Optical properties				
Optical band gap, E_o (eV)	3.28	3.06	3.22	3.24
Refractive index, n_o	2.099	2.162	2.117	2.092
Thermal Properties				
First glass transition temperature, T_{g1} (°C)	447	453	452	440
Second glass transition temperature, T_{g2} (°C)	500	504	504	498
Glass melting temperature, T_m (°C)	724	724	724	724

The measured values of density for the prepared samples are given in Table 5.2. A clear decrease of density from 5.51 gcm^{-3} to 5.36 gcm^{-3} is observed with the incorporation of 3×10^7 number of AuNPs. Moreover, a negligible increase in density from 5.36 gcm^{-3} to 5.42 gcm^{-3} is detected with the increase in gold content from 3×10^7 to 3×10^9 in the glass that still remains lower as compared to density value of base glass. Fig. 5.5 shows the density dependence on AuNPs concentration. The incorporation of AuNPs inside the glass matrix results in formation of non-bridging oxygens that in turn alters the glass structure resulting into decrease in density [29].

5.2.4. Thermal properties

5.2.4.1. Differential thermal analysis

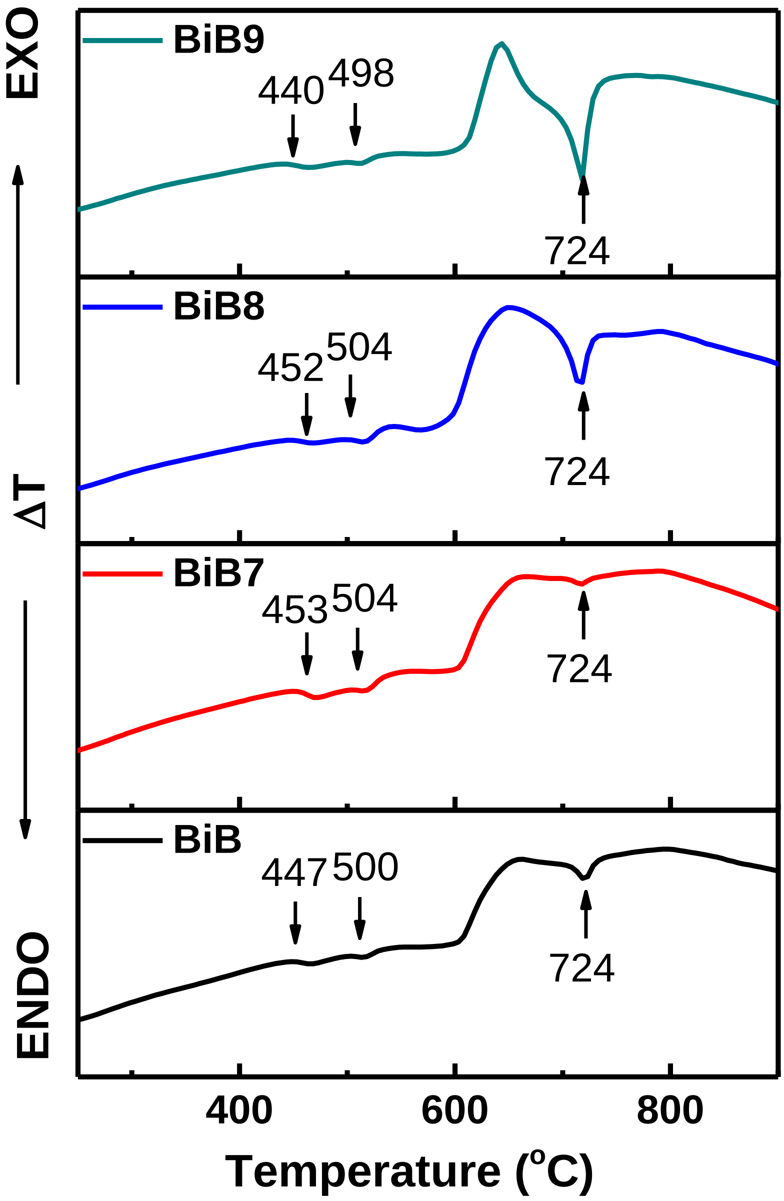

Figure 5.6: Isotherms for the prepared glasses (undoped and doped with different concentrations of AuNPs) representing the two glass transition temperatures (T_{g1} and T_{g2}) and glass melting temperature (T_m).

Fig. 5.6 displays the DTA thermogram for the bare glass and for the glasses dispersed with AuNPs with different concentrations. Three endothermic peaks are evidenced in Fig. 5.6. The onset of first two peaks represents the two glass transition temperatures T_{g1} and T_{g2} whereas the third peak corresponds to melting point (T_m) of the glass. Existence of two glass transition temperatures evidences the presence of phase separation inside the glass [30]. The values of T_{g1}, T_{g2} and T_m are summarized in Table 5.2.

For the base glass without AuNPs (BiB), the first and second glass transition temperature (T_{g1} and T_{g2}) are detected at about 447 ^{o}C and 500 ^{o}C, respectively. However, an increase from 447 ^{o}C to 500 ^{o}C in the value of T_{g1} and from 500 ^{o}C to 504 ^{o}C in T_{g2} is observed for the sample BiB7 containing 3×10^7 number of AuNPs. This increase in the glass transition temperature is attributed to shielding effect of AuNPs. Due to the presence of AuNPs, more heat will be required to break the bonds because of the shielding by AuNPs that results in the increased glass transition temperature [31]. With the increase in gold concentration from 3×10^7 to 3×10^8 for sample BiB8 and finally to 3×10^9 for sample BiB9, a small but clear decrease in T_{g1} and T_{g2} values are witnessed with respect to the glass containing low concentration of AuNPs. This can be explained on the basis of FESEM results showing that with the increase in concentration of gold, coagulation of AuNPs takes place, resulting in formation of bigger particles which will not be able to shield the bonds from high temperature leading to a lower T_g. Also, this decrease in T_g with increase in concentration of AuNPs results in enhanced coagulation as reported by Zeng *et al.* [32]. Sharma *et al.* [33] reported that the addition 3×10^8 number of AuNPs in borosilicate glass also shifts the T_g to lower temperature. Further, decrease in glass formation ability and stability is observed (observed decrease in T_g) with increase in concentration of AuNPs. Melting point of glass shows no significant dependence on addition and concentration of AuNPs inside the glass (Table 5.2).

5.2.5. Optical Properties

5.2.5.1.UV-Visible-NIR spectroscopy

Transmission spectra (Fig. 5.7 (a)) of prepared glass samples clearly indicate that all samples exhibit transparency in the visible region. The reference glass is 83% transparent whereas the decrease in transparency to 53% is observed for the glass sample with lowest concentration of AuNPs. In Fig. 5.7, fair increase in the transmission is found with the increase in the concentration of AuNPs. It is well known that AuNPs strongly absorb and scatter light and their optical response depends on the size of the nanoparticles. As the particle size increases, the scattering efficiency increases [34]. However, as seen from Fig. 5.5, the increase in particle size with concentration is associated with reduction in density of nanoparticles in the glasses. This results in reduced scattering and thus enhanced transmission with increasing gold concentration. The decrease in transmission in the form of dip at 465 nm observed with addition of AuNPs is attributed to the absorption of light from Bi^+ active centres (Fig. 5.7) [35].

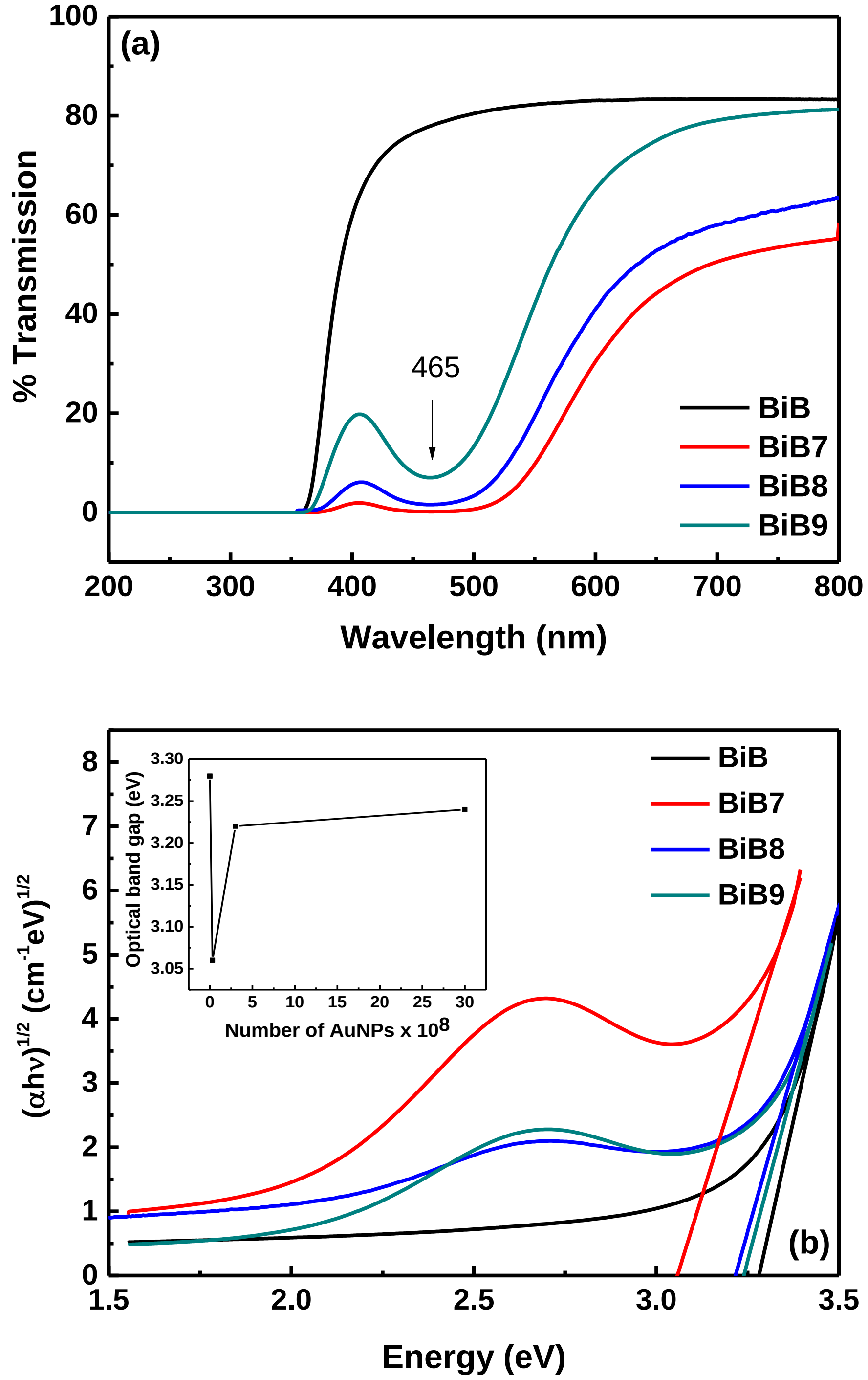

Figure 5.7: (a) Measured transmission spectra for undoped and doped samples with varying concentrations of AuNPs and (b) Tauc's plot for all the glass samples. Inset of (b) shows the variation in band gap with AuNPs concentration.

Fig 5.7 (b) shows the Tauc plots for the prepared glasses and the calculated value of optical band gap are given in Table 5.2. Inset of Fig 5.7 (b) displays the variation in optical band gap with AuNPs concentration. The observed decrease in optical band with the incorporation of 3 × 10^7 number of AuNPs is associated with the increase in structural disorderness and reduces rigidity of glass [9]. With increase in gold content, the particle density inside the glass decreases (as observed in FESEM images) and results in reduction of disorderness. Because of this the optical band gap value increases. However, the band gap of AuNP dispersed glasses remains lower than the base glass (BiB) because of formation of non-bridging oxygens as discussed in previous chapter.

5.2.5.2.Z-scan

In Fig. 5.8 (b), solid squares represents the recorded OA Z-scan data for bare and AuNPs dispersed glass samples whereas the solid line represents the theoretical fit. The observed dip at $Z = 0$ for all the glasses illustrates the existence of reverse saturable absorption (RSA). Moreover, the calculated values of $h\nu/E_o$ for all samples lies between 0.5 and 1. According to the theory of nonlinearity given by Sheik Bahae *et. al.* origin of RSA in such cases is two photon absorption (2PA) induced by electronic transitions of Bi^{3+} [36,37]. Also, obtained data fits well with the two photon absorption theory discussed in section 3.3.8 and the values of 2PA coefficient (β) obtained after fitting are displayed in Table 5.3. The electronic transitions in Bi ions present in the bare glass induces the 2PA which is further altered by the presence of AuNPs [38]. The decrease in 2PA coefficient with the addition of AuNPs is attributed to the suppression of electronic transitions. This suppression further increases with increase in AuNPs content and leads to decrease in 2PA coefficient (Table 5.3). Xu et al. [37] reported that the enhancement in nonlinear response in metal nanoparticle doped glasses is dependent on local surface plasmon resonance and excitation wavelength. In the present study, nonlinear measurements are carried out at non-resonant wavelength (800 nm) where virtual transitions give rise to non-resonant nonlinearities. For non-resonant excitation, the free electrons with insufficient energy gets trapped in the energy states that leads to the blocking of 2PA caused by electronic transition [39]. This blocking increases with the increase in size of nanoparticles. As AuNPs size increases with increase in gold concentration and hence results into decrease in 2PA coefficient.

In Fig. 5.8 (b), the obtained CA Z-scan experimental data is represented by solid squares whereas the theoretical fit done using the theory discussed in section 3.3.8 is shown by a solid line. The value of nonlinear refractive index (n_2) obtained are displayed in Table 5.3. The sepra-

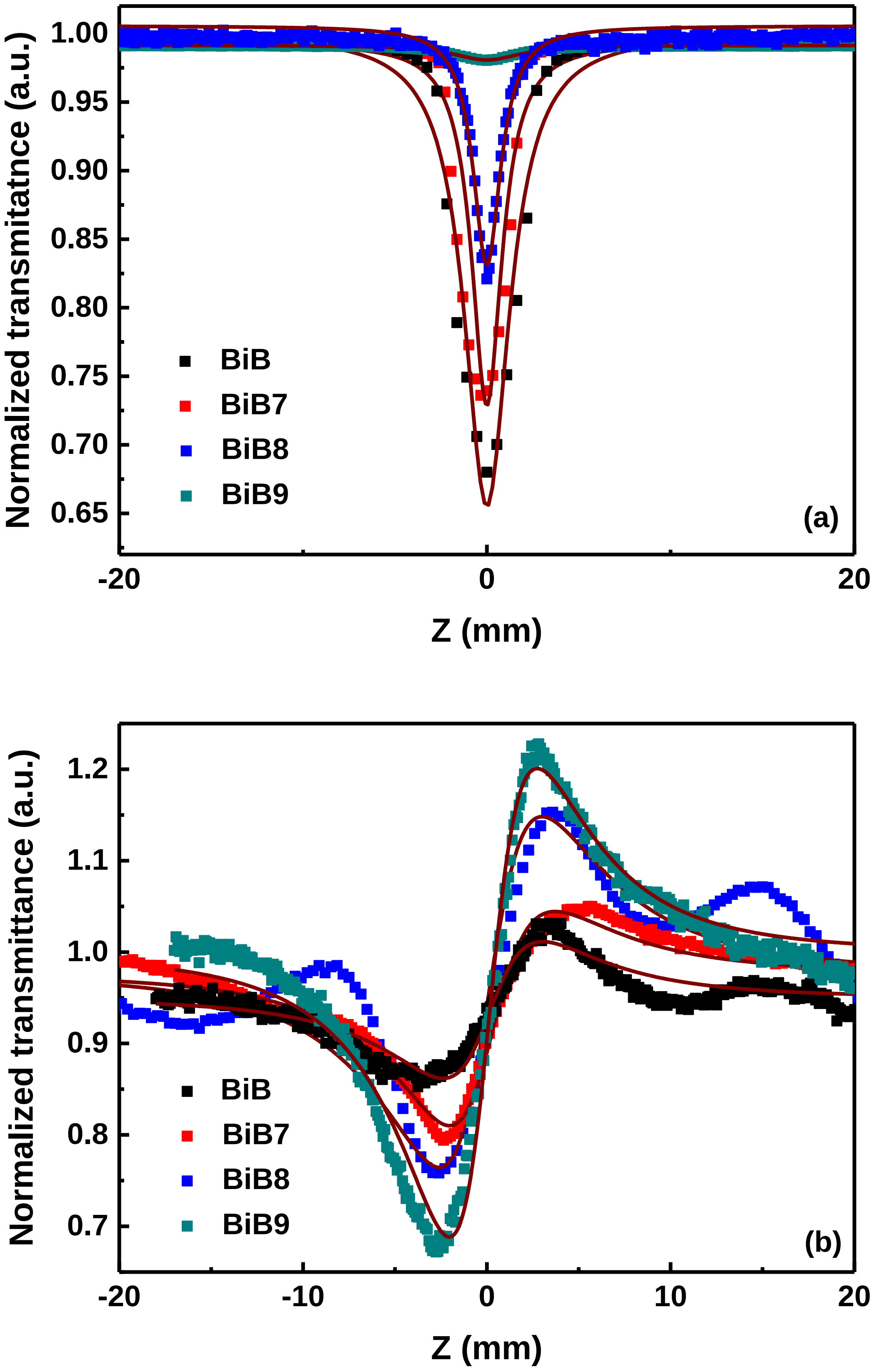

Figure 5.8: Z-scan curves obtained from (a) Open aperture and (b) Closed aperture setup taken at 800 nm. The solid square dots is the obtained experimental data and solid lines represents the theoretical fit.

-tion between dip and peak position is calculated to be 1.7 Z_0 that validate the existence of nonlinearity with ultra-fast response due to a purely electronic process [36]. Zhu et al. [40] demonstrated that the presence of heavy metal oxide in the glass composition results in high nonlinear refractive index due to unusual hyper-polarizability of non-bridging lone pair electrons of heavy metal ion and effective screening of outer electrons from the nucleus under the influence of applied optical electric field. In the present case, the hyper-polarizability of the Bi ions present in the glass composition leads to the existence of positive type of nonlinearity even in the undoped glass. Moreover, the third order nonlinearity increases with the increase in the concentration of nanoparticles inside the glass. The increase in nonlinear refractive index with the addition of gold is attributed to enhanced local electric field due to surface plasmon resonances. Nonlinear susceptibility also increases with increase in gold concentration (Table 5.3). The calculated values of Figure of merits are displayed in table 5.3. The Figure of merit F increases and T decreases with increase in AuNPs content in the glass making them suitable for several optical applications.

Table 5.3: Nonlinear absorption coefficient (β), nonlinear refractive index (n_2), nonlinear susceptibility (χ_3) and figure of merits (F, W, T) obtained after fitting Z-scan data.

Sample	**β (m/W)**	**n_2 (m^2/W)**	**$\left|\chi^{(3)}\right|$ (esu)**	**F**	**W**	**T**
BiB	4.3×10^{-12}	9.2×10^{-19}	1.1×10^{-12}	0.13	>1	3.77
BiB7	3.4×10^{-12}	1.3×10^{-18}	1.5×10^{-12}	0.24	>1	2.10
BiB8	0.9×10^{-12}	1.8×10^{-18}	2.0×10^{-12}	1.11	>1	0.44
BiB9	1.3×10^{-13}	2.1×10^{-18}	2.4×10^{-12}	9.96	>1	0.05

5.3. Effect of size

Bismuth borate glass dispersed with three different size of AuNPs (10 nm, 40 nm and 100 nm) are prepared using RTM methods. All the samples are prepared with 3×10^8 number of nanoparticles initially as least coagulation was observed for sample containing 3×10^8 number of nanoparticles as reported in the previous section. Table 5.4 shows the composition of prepared samples and the samples obtained after cutting and polishing are shown in Fig 5.9. Samples are characterised using following techniques and all the results are discussed in light of change in size.

Table 5.4: Composition of the prepared glasses.

Sample label	**Percentage Composition**		**Number of AuNPs**	**Size of AuNPs (nm)**
	Bi_2O_3	**B_2O_3**		
BiB0	35	65	-	-
BiB10	35	65	3×10^8	10
BiB40	35	65	3×10^8	40
BiB100	35	65	3×10^8	100

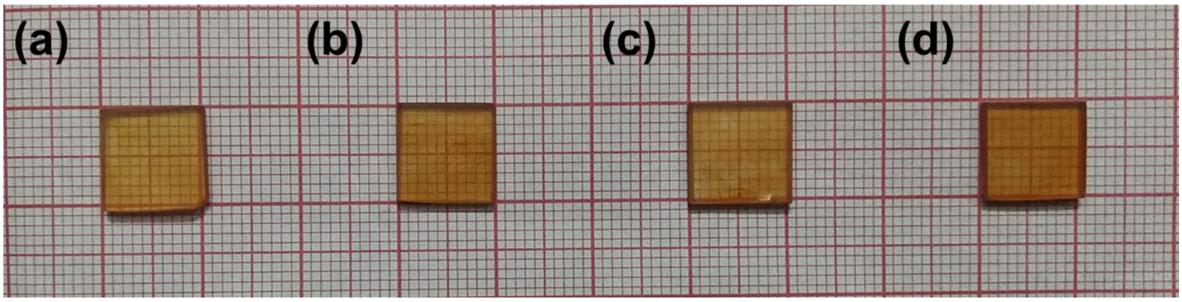

Figure 5.9: Picture of sample (a) BiB0, (b) BiB10, (c) BiB40 and (d) BiB100.

5.3.1. Structural analysis

5.3.1.1. X-ray Diffraction

Fig. 5.10 shows the X-ray diffraction pattern of the present glass systems with no detectable sharp peaks. The presence of two broad peaks centred at 27° and 45° shows the existence of short range ordering in the synthesised materials and hence confirms its glassy nature. The increased scattering due to larger AuNPs is seen in BiB40 and BiB100 samples.

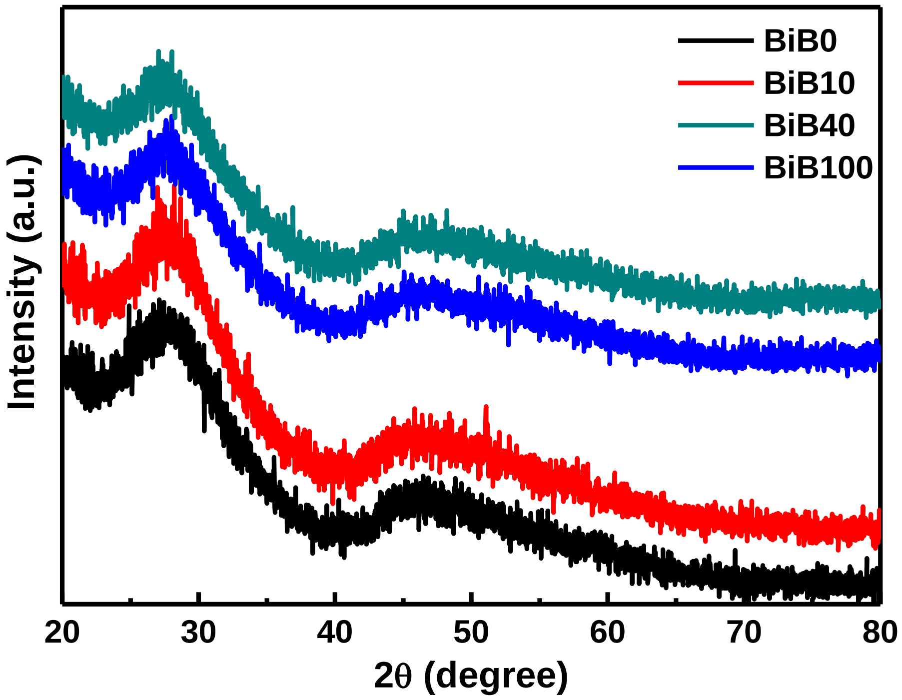

Figure 5.10: X-ray diffraction spectra of the prepared glass systems.

5.3.1.2. Fourier Transform Infrared Spectroscopy (FTIR)

Fig. 5.11 shows the effect of size of nanoparticle on the infrared spectra of the studied glass samples. The infrared spectra of bismuth borate glass shows three main bands in (i) 640

-740 cm^{-1}, (ii) 800-1200 cm^{-1} and (iii) 1200- 1500 cm^{-1} regions which are the main features of borate glasses. In Fig. 5.11, presence of peaks centred at 460 cm^{-1} and 580 cm^{-1} in the region 400-600 cm^{-1} are attributed to the vibration of Bi-O bonds and overlapping of Bi-O bonds in BiO_6 octahedral units [22,41]. The appearance of the peaks becomes more prominent with the increase in the size of the AuNPs incorporated. A clear shift from 710 cm^{-1} to 700 cm^{-1} for sample BiB40 that further shifts to 680 cm^{-1} for BiB100 have been observed with the increase in size of AuNPs. Presence of shoulder around 854 cm^{-1} is related to symmetric vibrations of Bi-O bonds in BiO_3 structural units whereas appearance of peak centred at 930 cm^{-1} is attributed to stretching vibrations of B-O linkage in BO_4 units. Further, a peak around 1300 cm^{-1} is observed for the base glass (BiB) that gets broaden for the sample BiB10 and BiB40. Finally these peaks get splitted into two peaks centred at 1220 cm^{-1} and 1360 cm^{-1}. The band centred at 1300 cm^{-1} is assigned to asymmetrical bond vibrations of B-O in BO_4 units [42,43]. While for the sample BiB100 two peaks around 1220 cm^{-1} and 1360 cm^{-1} which are attributed to the presence of the BO_3 units [44] are observed and hence confirms the formation of non-bridging oxygens.

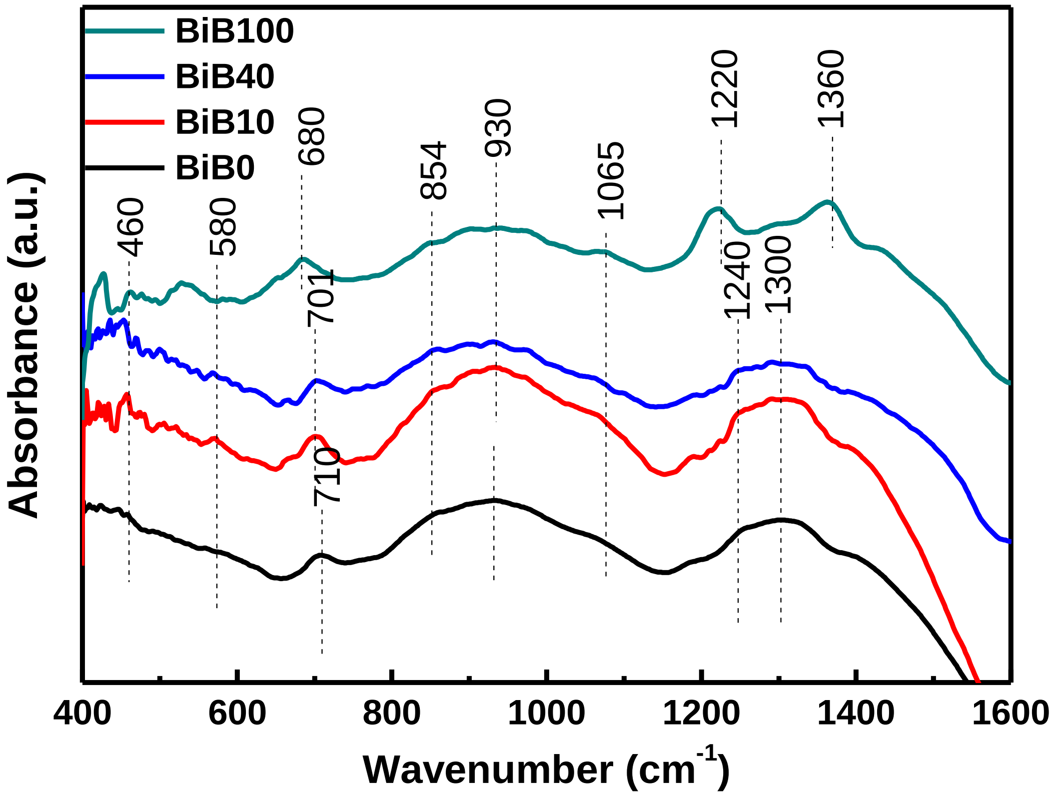

Figure 5.11: FTIR spectra of the prepared glass samples.

5.3.2. Morphological studies

5.3.2.1. Field emission scanning electron microscopy

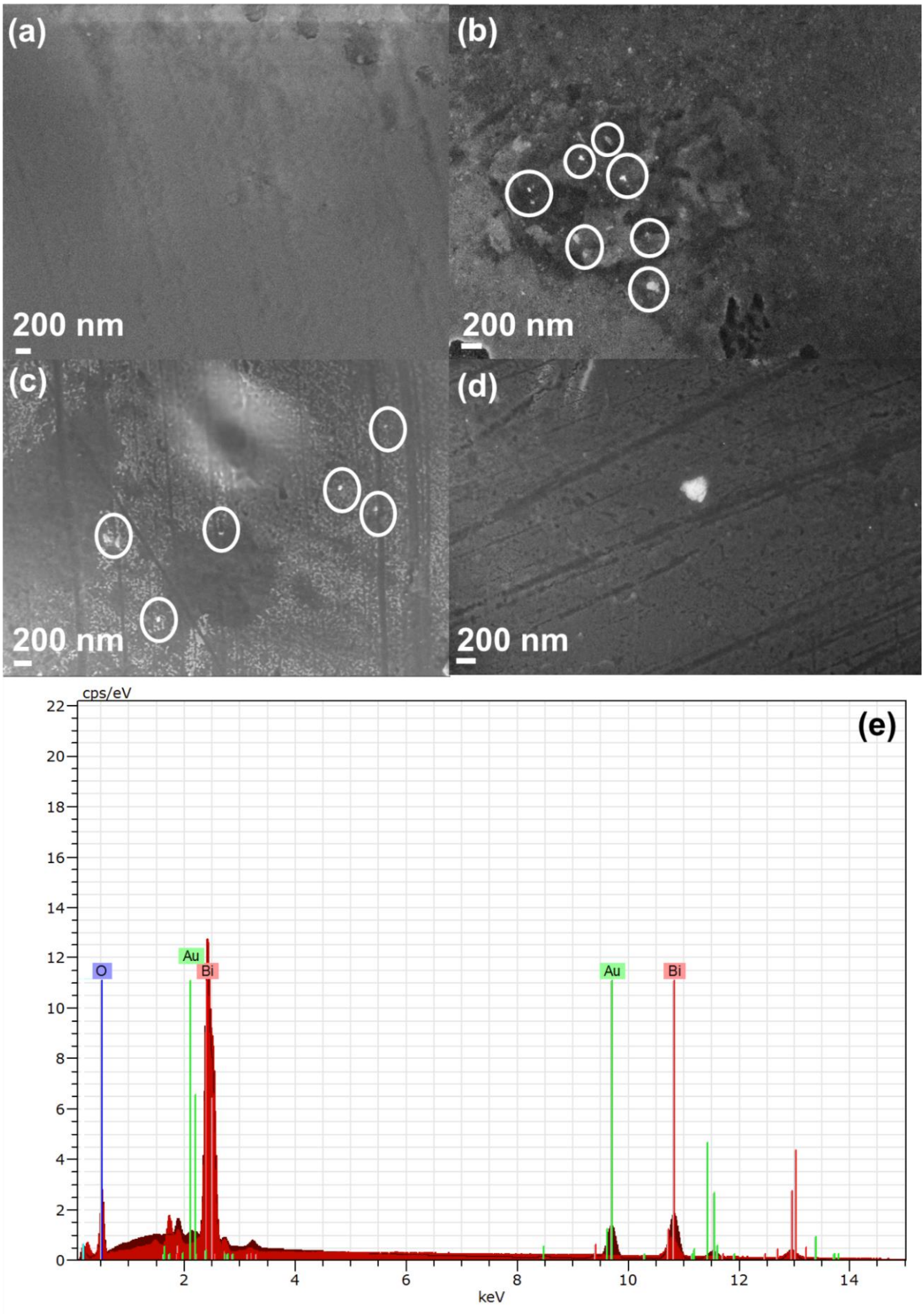

Figure 5.12: FESEM image of (a) BiB0, (b) BiB10, (c) BiB40 and BiB100. Circles have been used here to highlight the nanoparticles. Where (e) shows the EDS spectrum of BiB10.

In order to investigate the morphology of different size AuNPs inside the glass matrix, FESEM images are recorded and are shown in Fig. 5.12 (a-d). Fig. 5.12 (a) is the image of the bare glass (BiB0) and shows the glass matrix only. Fig. 5.12 (b-d) show the presence of AuNPs in the glass matrix. Particle size calculated from Fig. 5.12 (b), 5.12 (c) and 5.12 (d) are 45 nm, 78 nm and 200 nm for the samples BiB10, BiB40 and BiB100, respectively. The observed increase in particle size in comparison to the initially added AuNPs evidences the occurrence of phenomena of Ostwald's ripening and has been discussed in section 5.2.2. Moreover, the observed particle density is very less as compared to the number of particles added initially. Average particle separation between particles is also found to decrease with increase in particles size which is 0.5 μm, 0.4 μm and 0.3 μm for sample BiB10, BiB40 and BiB100, respectively. Since the as prepared AuNPs are mixed and heated in furnace along with the batch, the reduction in concentration of AuNPs may occur due to evaporation, oxidation phenomena and Ostwald's ripening while melting the batch at 850 °C [45]. The presence of Bismuth, Oxygen and Gold is confirmed from EDS shown in Fig 5.12 (e).

5.3.3. Physical properties of the glass

From Fig. 5.9, a clear change in colour from dark orange (BiB0) to light orange (BiB10) has been evidenced with the addition of 10 nm size AuNPs whereas this colour intensity further increases with the increase in size of incorporated AuNPs from 10 nm to 100 nm. This observed color change is highly dependent on the morphology and size of nanoparticles as seen from FESEM micrographs.

5.3.3.1. Density measurements

Table 5.5: Measured physical, optical and thermal properties for the prepared glass samples.

Properties	BiB0	BiB10	BiB40	BiB100
Physical properties				
Density, ρ (gcm^{-3}) ± 1%	5.86	5.74	5.76	5.78
Optical properties				
Optical band gap, E_o (eV)	3.09	3.08	3.07	3.06
Refractive index, n_o	2.373	2.374	2.377	2.381
Thermal Properties				
Glass transition temperature, T_g (°C)	444	443	439	435
Onset crystallization temperature, T_x (°C)	571	554	555	562
First peak crystallization temperature, T_{p1} (°C)	592	571	580	582
peak crystallization temperature, T_{p2} (°C)	-	615	609	617
Glass melting temperature, T_m (°C)	722	722	722	722
ΔT (°C)	128	111	116	121
K_w	0.18	0.15	0.16	0.17

Table 5.5 displays the measured values of density for the series being discussed here. The density value decreases from 5.86 gcm^{-3} to 5.74 gcm^{-3} with the addition of AuNPs. The added AuNPs goes into the free space present in the structure and results in elongation of bonds. Decrease in density suggests that incorporation of gold assists Bi_2O_3 to create NBOs [46]. The presence of non-bridging oxygens results in weakening of glass network and hence reduces the density.

5.3.4. Thermal properties

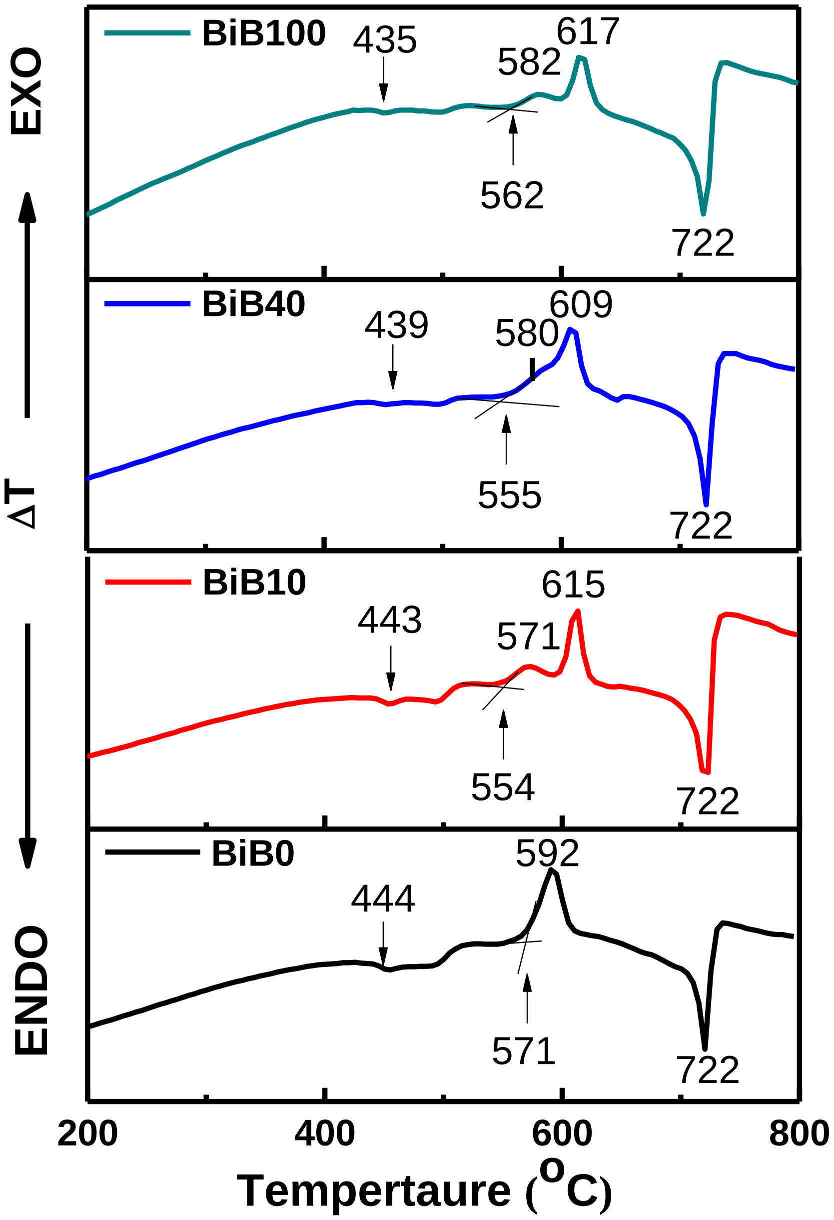

Figure 5.13: Thermograph of the prepared glass samples.

Fig. 5.13 displays the thermogram of the prepared glass samples. The results of thermal parameters like glass transition temperature (T_g), onset crystallization temperature (T_x), peak crystallization temperature (T_p), melting points (T_m) and thermal stability factor ($\Delta T = T_x - T_g$) are given in Table 5.5. It is observed that with the addition of AuNPs (of any size) leads to the appearance of two crystallisation peaks which directly indicates to the existence of phase separation [30]. As discussed in section 5.2.2, while melting the glass, AuNPs first splits into Au atoms which coagulate to form bigger AuNPs (as seen in Fig. 5.12) or it can be said that gold nano-composites are formed which leads to the existence of the phase separation. It can be clearly seen that with the addition of AuNPs, T_g for the glass decreases. Lower T_g supports the coagulation of nanoparticles inside the glass [32]. Moreover, the bigger sized GNPs further decreases the T_g because of the shielding effect as discussed in section 5.2.4. No remarkable influence on the glass melting point has been observed.

Thermal stability factor is an important parameter to determine the working range for fiber drawing [47]. Larger the difference in T_x and T_g greater will be the resistance to crystallization [48]. For all the prepared samples, ΔT calculated using Equation (3.2) is more than 100 ^{o}C (Table 5.5) and hence the fabricated glasses are highly suitable for fiber drawing applications [49]. From Table 5.5, it is observed that ΔT and K_w decreases with the addition of AuNPs and hence the glass forming ability and stability gets decreased i.e. nucleation could take place more rapidly inside the glassy matrix.

5.3.5. Optical properties

5.3.5.1.UV-Visible absorption spectroscopy

Transmission spectra of the prepared glass sample is taken in the region of 200-900 nm and is displayed in Fig. 5.14 (a). It is clear from Fig. 5.14 that glasses show effective transparency in the visible region. Whereas, no surface plasmon resonance peak corresponding to the AuNPs is observed because of its low content as well as much larger size due to coagulation as seen from FESEM images. The observed peak at 465 nm is attributed to the presence of Bi in the glass matrix [35]. Negligible effect of variation of size of AuNPs is observed on the percentage transmission of the glass.

Optical transmission studies provides the information about band structure and hence the optical band gap of crystalline as well as non-crystalline material. Tauc's model discussed in section 3.3.6 for non-crystalline system is used here to further analyse the obtained optical data [50,51]. The Tauc's plot are shown in Fig. 5.14 (b) and the obtained values of optical band gap are displayed in Table 5.5. Inset of Fig 5.14 (b) is the magnified view of Fig 5.14 (b) clearly showing the variation in band gap. Noticeable decrease in optical band gap from 3.09 to 3.06 eV is observed with the increase in size of incorporated GNPs from 10 to 100 nm (Table 2).

This change in optical band gap is attributed to the increase in disorderness and decrease in rigidity of the glass as a result of formation of non-bridging oxygens with the addition of AuNPs [52].

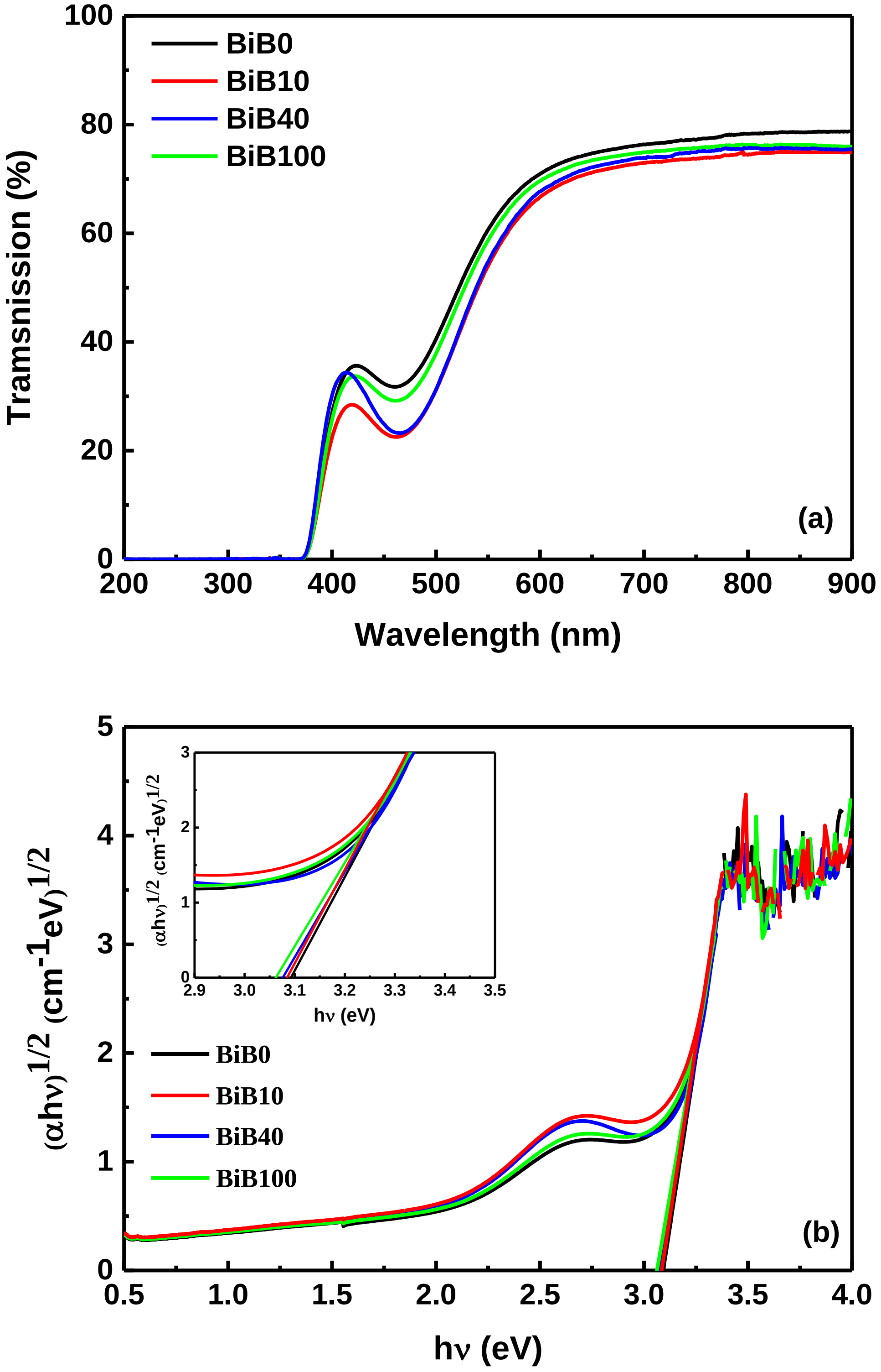

Figure 5.14: (a) Transmission spectra and (b) $(\alpha h\nu)^{1/2}$ v/s energy for band gap of $35Bi_2O_3{:}65B_2O_3$ undoped and doped with differently sized 3×10^8 number of GNPs. Inset is the magnified view of 5 (b).

5.3.5.2.Z-Scan

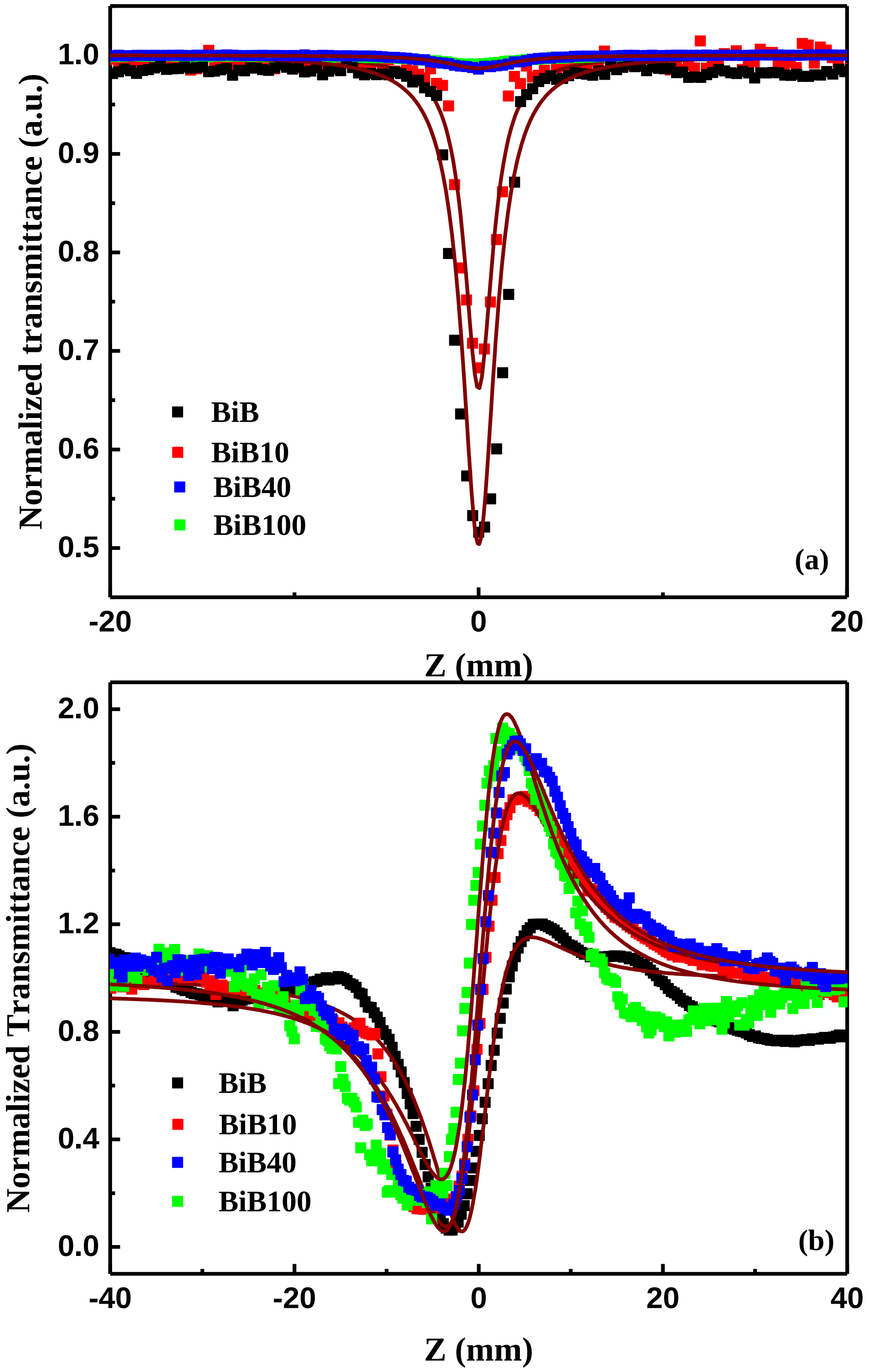

Figure 5.15: Z-scan curves obtained from (a) Open aperture and (b) Closed aperture setup taken at 800 nm. The solid square dots is the obtained experimental data and solid lines represents the theoretical fit.

Fig. 5.15 (a) displays the signatures of OA Z-scan data taken for all the samples. OA Z-scan curves of all the samples comprises of a valley at Z = 0 confirming the existence of RSA. As discussed earlier in section 5.2.6.2, the values of $h\nu/E_o$ for all samples lies between 0.5 and 1. Therefore, electronic transitions of Bi^{3+} ions present in the glass results in origin of RSA via 2PA [36,37]. The values of 2PA coefficient given in Table 5.6 are calculated by fitting the experimental data (shown by solid square in Fig. 5.15 (a)) using the Equation (3.7). Presence of AuNPs suppresses the electronic transitions leading to observed decrease in 2PA coefficient. Further decrease in 2PA coefficient with increase in size is attributed to increased suppression in electronic transitions with increase in particle size.

Fig. 5.15 (b) displays the CA Z-scan data with features of a valley followed by a dip which indicates the existence of positive type of nonlinearity and the lensing effect leading to self-focusing. Purely electronic processes in Bi ions leads to the existence of ultra-fast third order nonlinearity [36]. In order to calculate the nonlinear refractive index (n_2), the CA Z-scan data is fitted using the equation (3.8). Theoretical fit is shown using a solid line in Fig. 6.7. After substituting the fitting parameter to equation (3.9), the value of n_2 is obtained and is reported in Table 5.6. Theory fits well with the data and the third order nonlinearity increases with the increase in the particle size of nanoparticles inside the glass. Surface plasmon responses associated with AuNPs enhances the local electric field inside the glass that results in increase in nonlinear refractive index. The calculated values of χ^3, F, W and T are displayed in Table 5.6.

Table 5.6: Nonlinear absorption coefficient (β), nonlinear refractive index (n_2), nonlinear susceptibility (χ_3) and figure of merits (F, W, T) obtained after fitting Z-scan data.

Sample	**β (m/W)**	**n_2 (m^2/W)**	**$\lvert\chi^{(3)}\rvert$ (esu)**	**F**	**W**	**T**
BiB0	5.2×10^{-12}	1.0×10^{-18}	1.5×10^{-12}	0.13	>1	3.94
BiB10	3.8×10^{-12}	2.0×10^{-18}	2.9×10^{-12}	0.33	>1	1.52
BiB40	1.4×10^{-13}	2.2×10^{-18}	3.2×10^{-12}	9.60	>1	0.05
BiB100	9.0×10^{-14}	2.5×10^{-18}	3.6×10^{-12}	17.34	>1	0.02

5.4. Role of matrix composition

A series of glasses having base composition $(30+x)Bi_2O_3$-$(70-x)B_2O_3$ (x = 0, 5 and 10) dispersed with 0 and 3×10^8 number of 10 nm size AuNPs are prepared (Table 5.7). In order to study the effect of composition on structural, thermal and optical performance of AuNPs dispersed glasses, all the parameters are compared and discussed in light of varying concentration of Bi_2O_3.

Table 5.7: Composition of glasses under investigation.

Sample label	**Percentage Composition**		**Number of AuNPs**	**Size of AuNPs (nm)**
	Bi_2O_3	**B_2O_3**		
BiB	30	70	-	-
BiB8	30	70	3×10^8	10
BiB0	35	65	-	-
BiB10	35	65	3×10^8	10
BiB **'0'**	40	60	-	-
BiB **'10'**	40	60	3×10^8	10

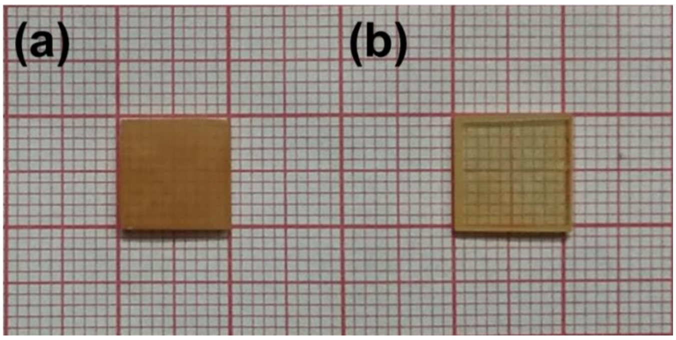

Figure 5.16: Picture of well-polished (a) BiB **'0'** and (b) BiB **'10'** glass samples.

5.4.1. Structural analysis

5.4.1.1. X-ray diffraction

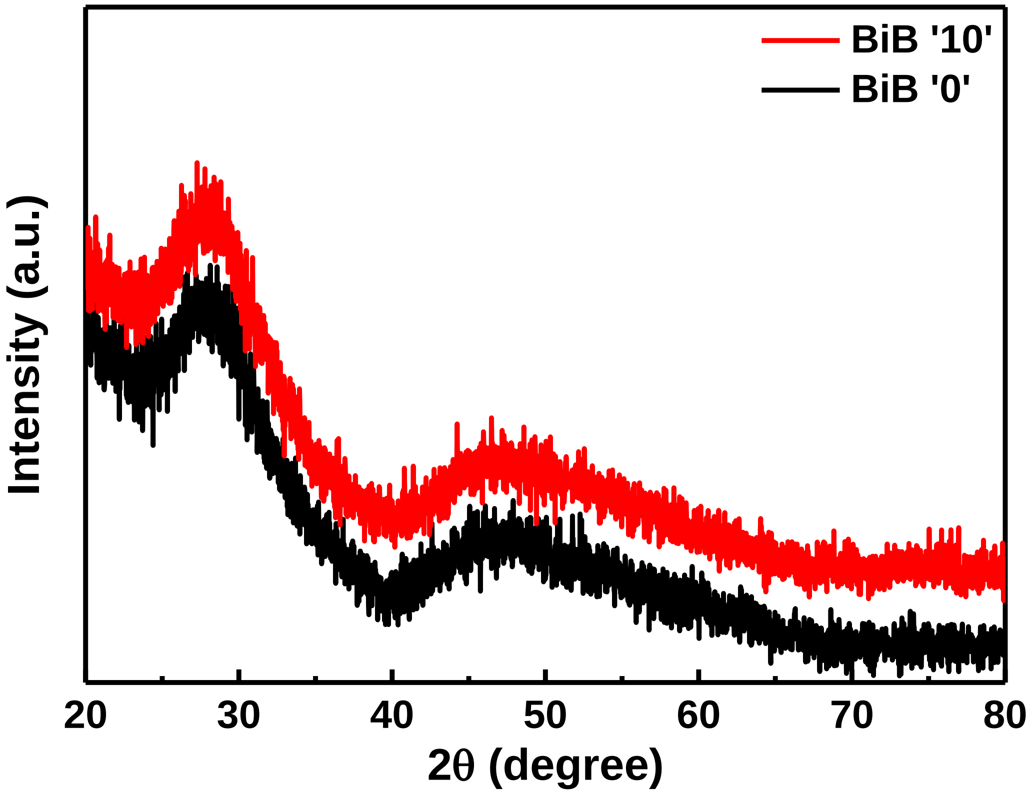

Figure 5.17: XRD pattern of bare and AuNPs dispersed $40Bi_2O_3{:}60B_2O_3$ glass.

X-ray diffraction pattern of BiB **‘0’** and BiB **‘10’** are given in Fig. 5.17 whereas the spectra for rest of the samples mentioned in Table 5.7 have already been given and discussed in previous sections. Existence of two diffuse broad humps around lower angle region observed for all the glass samples clearly indicates their phase separated amorphous nature [53]. Further, this amorphous nature is not affected by the variation in Bi_2O_3 concentration both in bare as well as AuNPs dispersed glasses.

5.4.1.2.Fourier transform infrared spectroscopy

Fig. 5.18 displays the FTIR spectra of $40Bi_2O_3$:$60B_2O_3$ glass containing 0 (BiB **‘0’**) and 3 × 10^8 (BiB **‘10’**) number of AuNPs. In order to identify the effect of Bi_2O_3 concentration on structural behaviour of glasses, all the observed peaks in the IR spectra of glasses under investigation as given in Table 5.8. Fundamental vibrations corresponding to the presence of Bi_2O_3 in the glass appears at 460 cm^{-1}, 580 cm^{-1} and 854 cm^{-1} whereas the bands corresponding to B_2O_3 are observed in the three region (640-740 cm^{-1}, 800-1200 cm^{-1} and 1200-1500 cm^{-1}). The attribution of the peaks are enlisted in Table 5.8 have already been discussed in section 5.2.1.2 and 5.3.1.2. With the increase in Bi_2O_3 content from 30 mol% to 40 mol% the peaks become more intense that correspond to the formation of non-bridging oxygens inside the glass [22].

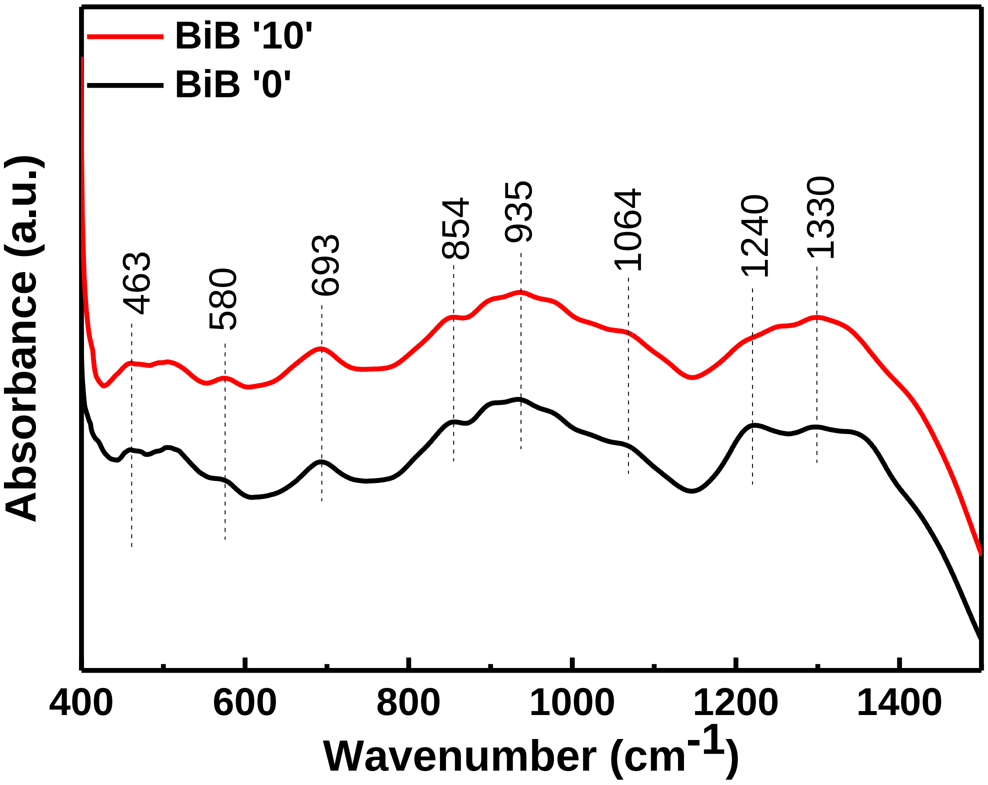

Figure 5.18: FTIR spectra of $40Bi_2O_3$:$60B_2O_3$ glass containing 0 and 3 × 10^8 number of AuNPs.

Table 5.8: Peak positions and corresponding band assignments for the samples containing different concentrations of Bi_2O_3.

Glass sample and peak positions in cm^{-1}						Assignments
BiB	**BiB8**	**BiB0**	**BiB10**	**BiB ‘0’**	**BiB ‘10’**	
460	460	460	460	463	463	Bi-O vibrations in octahedral BiO_6
580	580	580	580	580	580	
700	694	710	701	693	693	Bending vibration of B-O-B in BO_3 triangles
854	854	854	854	854	854	Symmetrical stretching vibrations of Bi-O linkage in BiO_3 structural units
930	930	930	930	935	935	B-O bond stretching of tetrahedral BO_4 units
-	1065	1065	1065	1064	1064	Asymmetric vibration in $[BO_4]^{-5}$ units
-	1240	1240	1240	1240	1240	Stretching vibration of B-O in $(BO)^{3-}$ units
1330	1330	1300	1300	1330	1330	B-O bond stretching of trigonal BO_3 units

5.4.2. Morphological studies

5.4.2.1. Field emission scanning electron microscopy

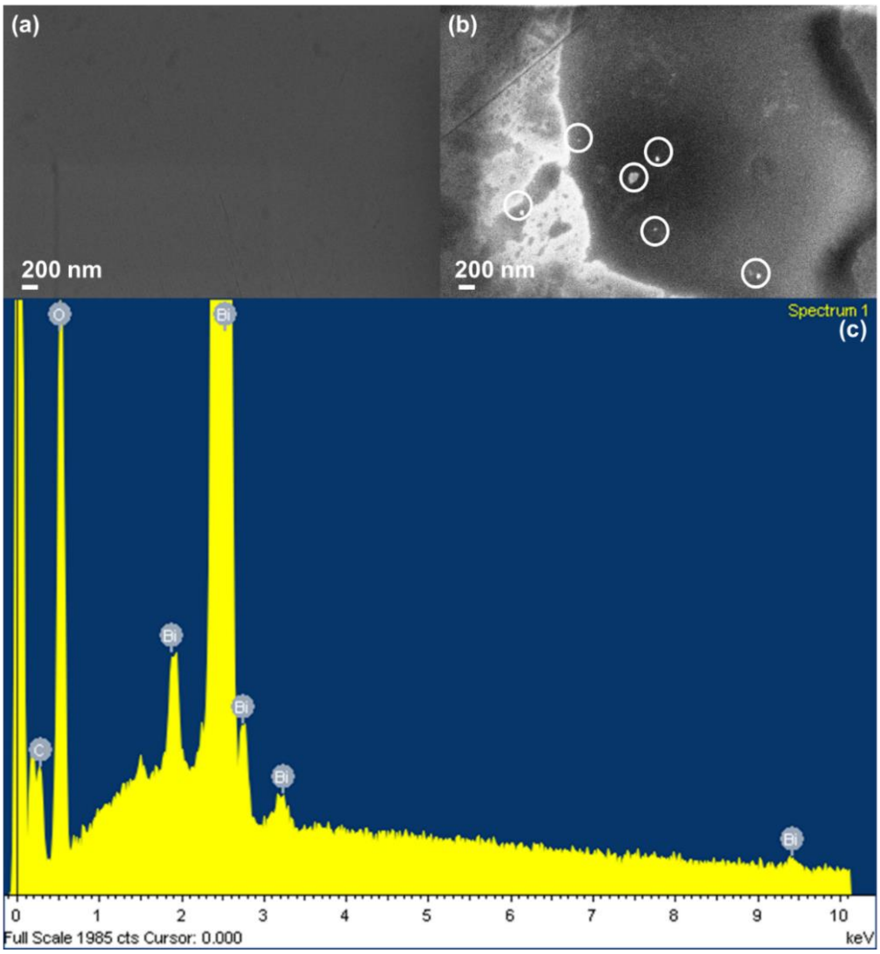

Figure 5.19: FESEM micrographs for glass (a) BiB **‘0’** and BiB **‘10’**. AuNPs are highlighted using circles. (c) is EDS spectrum of BiB **‘0’** showing the presence of different elements**.**

FESEM micrograph of bare glass BiB **'0'** is given in Fig. 6.19. Fig. 6.19 (a) shows the glass surface only. Presence of average 80 nm size AuNPs in BiB **'10'** (40 mol% Bi_2O_3) is verified from Fig. 6.19 (b). Also the obtained particles size from Fig. 5.4 (c) and 5.12 (b) for AuNPs dispersed sample BiB8 and BiB10 containing 30 and 35 mol% Bi_2O_3, respectively are summarised in Table 5.9. It is clear that particle size i.e. coagulation of AuNPs increases with the increase in Bi_2O_3 content with almost same particle density. This increase in coagulation can be explained on the basis of thermal studies discussed in forthcoming section. The recorded EDS spectrum for sample BiB **'0'** is shown in Fig 5.19 (c).

5.4.3. Physical properties of glass

A clear change in colour for bare glass from transparent to dark orange and then yellow is observed with the increase in Bi_2O_3 mol% from 30 to 40 as shown in Fig 5.1, Fig 5.9 and Fig 5.16, respectively. Whereas, for AuNPs dispersed glasses the colour gets modified from dark brown to orange and then yellow with the increasing Bi_2O_3 concentration.

5.4.3.1. Density measurements

Calculated density values of all the glasses are displayed in Table 5.9. A clear increase in density value from 5.51 to 6.19 gcm^{-1} and from 5.39 to 5.99 gcm^{-1} is observed with the increase in Bi_2O_3 concentration from 30 to 40 mol% in bare glass and AuNPs dispersed glasses, respectively. Fig. 5.20 shows the dependence of density on Bi_2O_3 concentration. Since, Bi_2O_3 is added on the expense of B_2O_3 in all the glasses and this increase is attributed to the relatively higher molecular mass of Bi_2O_3 as compared to B_2O_3 [17,54,55]. Whereas, observed decrease in density in AuNPs dispersed glass with respect to their respective bare glass for all the glass compositions occurs due to the formation of non-bridging oxygens in the glass having the presence of AuNPs as discussed in earlier sections.

Table 5.9: Obtained particle size from FESEM images, density, optical band gap, refractive index and thermal parameters for glasses containing different Bi_2O_3 concentration.

Sample code	**Size of NPs obtained from FESEM (nm)**	ρ	**E_o (eV)**	**n**	**Thermal parameters ^{0}C**						**ΔT**	**K_w**
					T_{g1}	**T_{g2}**	**T_x**	**T_{p1}**	**T_{p2}**	**T_m**		
BiB	-	5.51	3.28	2.10	447	500	-	-	-	724	-	
BiB8	30	5.39	3.22	2.12	452	504	-	-	-	724	-	
BiB0	-	5.86	3.09	2.37	444	-	571	592	-	722	128	0.18
BiB10	45	5.74	3.07	2.37	443	-	554	571	615	722	111	0.15
BiB **'0'**	-	6.19	3.04	2.39	428	-	535	555	638	716	107	0.15
BiB**'10'**	80	5.99	3.00	2.40	435	-	537	557	632	716	102	0.14

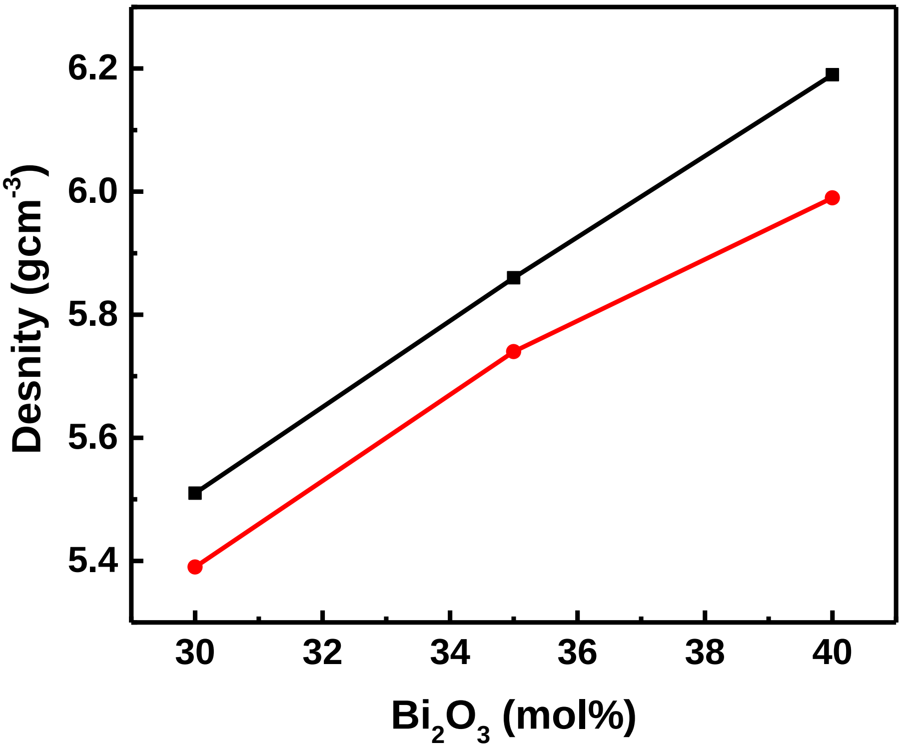

Figure 5.20: Measured density of bare and AuNPs dispersed verses Bi_2O_3 concentration. Density of bare glasses are represented with square solid dots whereas the density of AuNPs dispersed glasses are represented using circular solid dots.

5.4.4. Thermal properties

5.4.4.1. Differential thermal analysis

Thermograms for bare and AuNPs dispersed $40Bi_2O_3$:$60B_2O_3$ glasses are displayed in Fig. 5.21 and the obtained values of thermal parameters after analysis are reported in Table 5.9. Existence of multiple glass transition temperature and crystallization temperatures confirms the phase separation inside the glass. Moreover, it is evident from Table 5.9 that thermal parameters of glass shows significant dependency on Bi_2O_3 concentration. All the thermal parameters shifts to lower temperature with increase in bismuth concentration in bare as well in AuNPs dispersed glasses [56]. Decrease in glass transition temperature is directly related to bond strengths which is an intrinsic function of interionic bond lengths. The larger ionic radius of Bi^{3+} ion (0.108 nm) as compared to B^{3+} ion (0.02 nm) leads to reduction of Bi-O bond strength (80.3 Kcal mol^{-1}) than B-O bond strength (192.7 Kcal mol^{-1}) [57]. Increasing concentration of Bi_2O_3 on the expense of B_2O_3 inside the glass results in replacement of B-O linkage by weaker Bi-O linkage that reduces the glass transition temperature. In addition, this shift may be attributed to the formation of non-bridging oxygens inside the glass. As reported by Sharma *et al.* [33], reduced glass transition temperature results in enhanced coagulation of

AuNPs that further supports the FESEM results where increase in particle size is observed with the increase in Bi_2O_3 concentration.

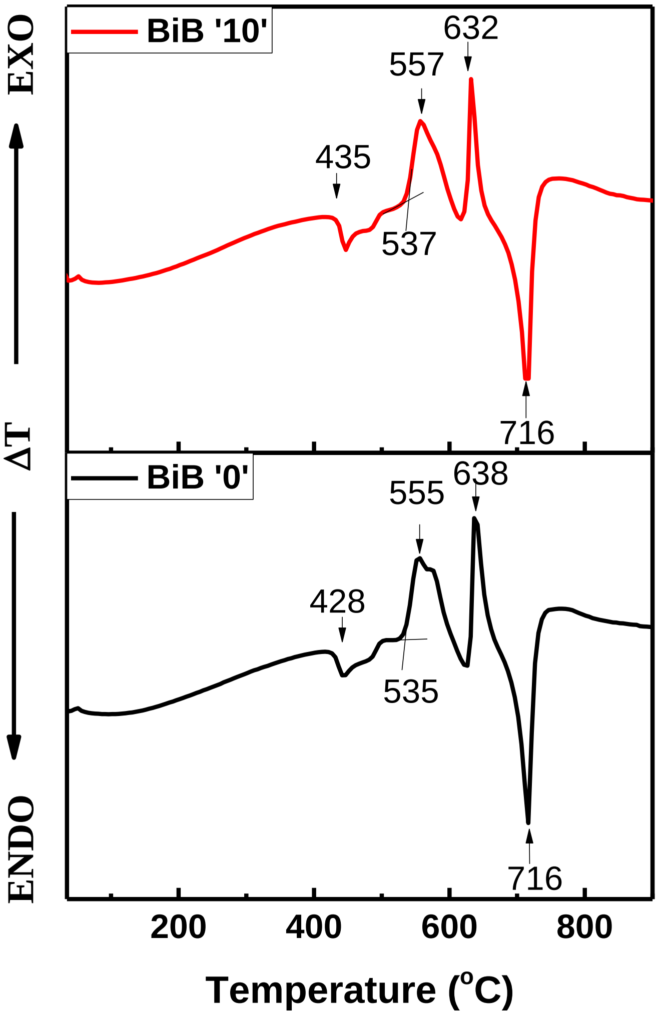

Figure 5.21: DTA trace of bare and AuNPs dispersed $40Bi_2O_3:60B_2O_3$ glass taken at 10 °C/ min heating rate.

5.4.5. Optical properties

5.4.5.1. Uv-VIS spectroscopy

Transmission spectra of BiB **'0'** and BiB **'10'** (both containing 40 mol% Bi_2O_3) are given in Fig. 5.22 (a). Percentage transmission decreases from 80% to 40% for the bare glass with the increase in Bi_2O_3 concentration from 30 mol% to 40 mol% (Fig. 5.7 (a), Fig. 5.14 (a) and Fig 5.22 (a)). Also, decrease in transmission due to presence of AuNPs in the glasses with respect to their respective bare glass is attributed to the scattering phenomena of nanoparticles. Transmission dip around 465 nm appears due to the presence of Bi ions in the glass.

Tauc plots for glass BiB **'0'** and BiB **'10'** are shown in Fig. 5.22 (b) and the calculated values of optical band gap for all the samples are given in Table 5.9. The band gap value decreases from 3.28 to 3.00 eV for bare glasses and from 3.22 to 3.00 for AuNPs dispersed glasses with the increase in Bi_2O_3 concentration from 30 to 40 mol%. This decrease is attributed to increase in non-bridging oxygens in the glass with increasing Bi content which is in agreement with FTIR results [58].

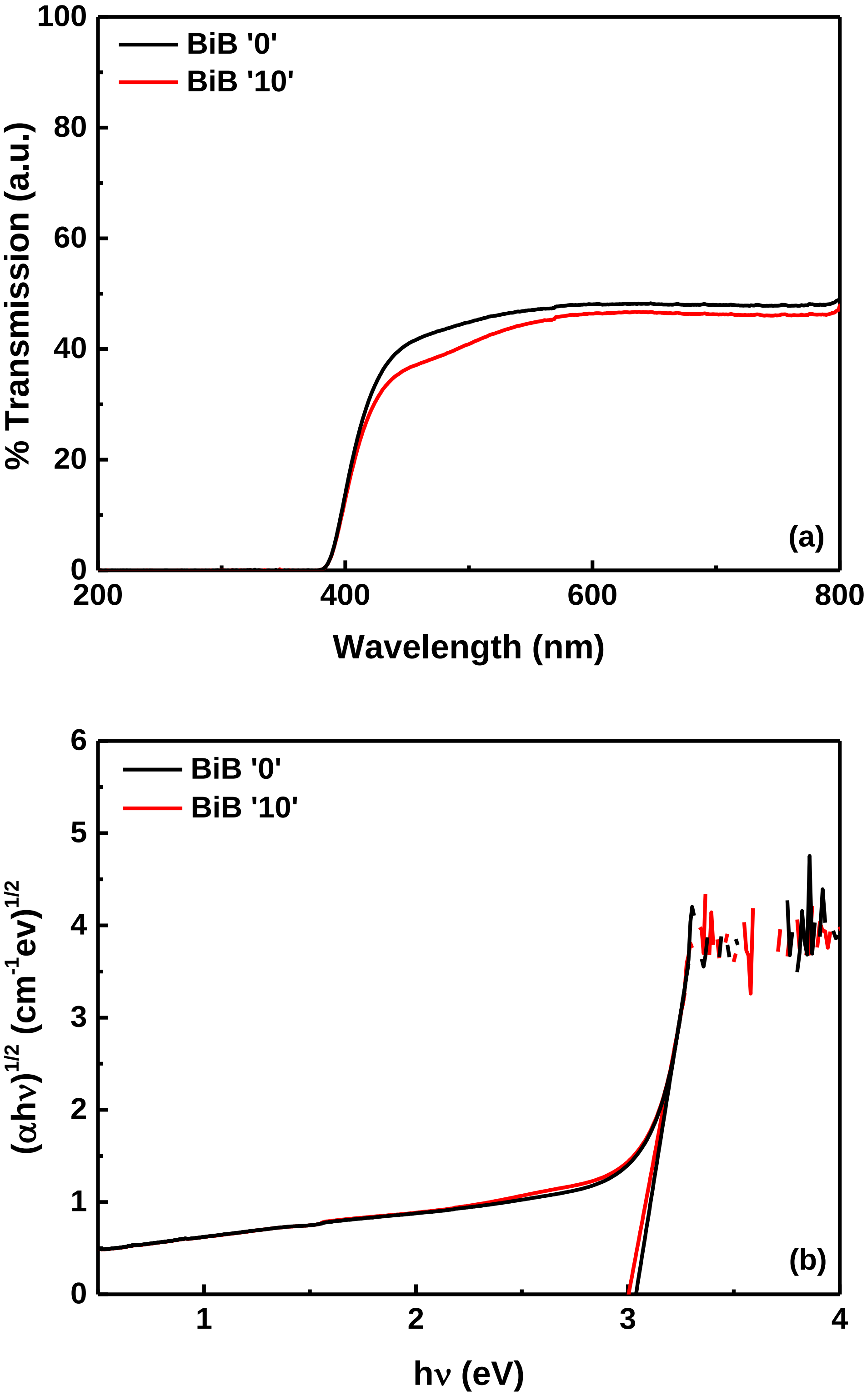

Figure 5.22: (a) Transmission spectra and (b) Tauc's plot for bare and AuNPs dispersed $40Bi_2O_3{:}60B_2O_3$ glass samples.

5.4.5.2. Z-Scan

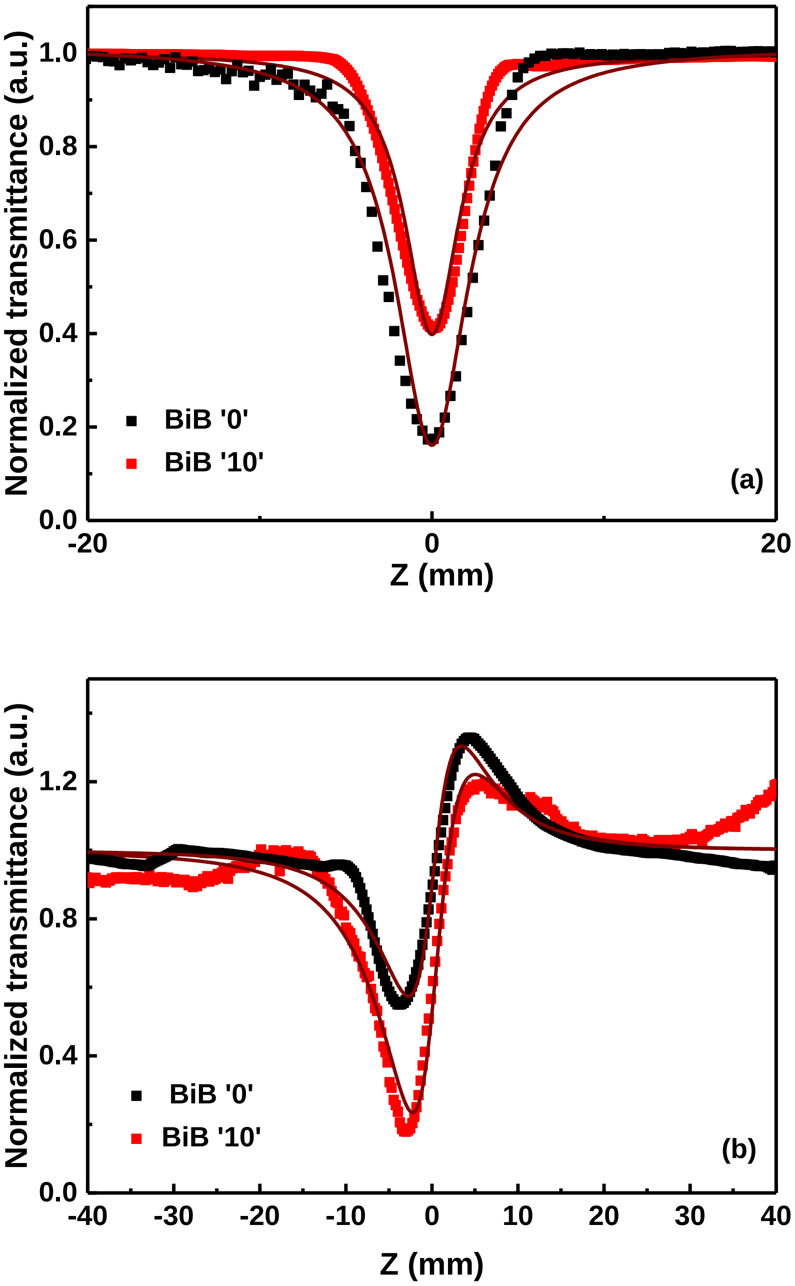

Figure 5.23: (a) Open aperture and (b) Closed aperture Z-scan curves obtained at 800 nm. The solid square dots is the obtained experimental data and solid lines represents the theoretical fit.

OA and CA Z-scan data along with the theoretical fit for bare and AuNPs dispersed $40Bi_2O_3:60B_2O_3$ glasses are represented in Fig. 5.23. Obtained nonlinear parameters (β, n_2 and $\chi^{(3)}$) for glasses containing different Bi_2O_3 content are listed in Table 5.10. Estimated values of nonlinear parameters increases with increase in Bi_2O_3 concentration from 30 to 40 mol% in bare as well as in AuNPs dispersed glasses. Hyper-polarizability of constituent elements like heavy metal oxide, transition elements and non-bridging oxygens are the origin of nonlinearity in oxide glasses. Replacement of more polarizable Bi_2O_3 by less polarizable B_2O_3 are the main reason behind the increase in nonlinearity [59,60]. Also, as observed from DTA and optical band gap results, progressive substitution of Bi_2O_3 leads to formation of more non-bridging oxygens. Distortion of valence electrons of non-bridging oxygens by strong electronic field results in stronger harmonic effects leading to enhanced nonlinearity [61].

Table 5.10: Nonlinear optical parameters (β, n_2 and χ_3) and figure of merits (F, W, T) obtained after fitting Z-scan data.

Sample	**β (m/W)**	**n_2 (m^2/W)**	**$\lvert\chi^{(3)}\rvert$ (esu)**	**F**	**W**	**T**
BiB	4.3×10^{-12}	9.2×10^{-19}	1.1×10^{-12}	0.13	>1	3.77
BiB8	0.9×10^{-12}	1.8×10^{-18}	2.0×10^{-12}	1.11	>1	0.44
BiB0	5.2×10^{-12}	1.0×10^{-18}	1.5×10^{-12}	0.13	>1	3.94
BiB10	3.8×10^{-12}	2.0×10^{-18}	2.9×10^{-12}	0.33	>1	1.52
BiB0’	7.8×10^{-12}	1.9×10^{-18}	2.7×10^{-12}	0.15	>1	3.35
BiB10’	4.8×10^{-12}	2.5×10^{-18}	3.7×10^{-12}	0.33	>1	1.50

References:

1 W. Haiss, N. T. K. Thanh, J. Aveyard and D. G. Fernig, 2007, **79**, 4215–4221.

2 K. Magyari, T. Nagy-Simon, A. Vulpoi, R. A. Popescu, E. Licarete, R. Stefan, K. Hernádi, I. Papuc and L. Baia, *Mater. Sci. Eng. C*, 2017, **76**, 752–759.

3 V. Aina, G. Cerrato, G. Martra, L. Bergandi, C. Costamagna, D. Ghigo, G. Malavasi, G. Lusvardi and L. Menabue, *J. R. Soc. Interface*, 2013, **10**, 1–10.

4 A. Awang, S. K. Ghoshal, M. R. Sahar and R. Arifin, *Opt. Mater. (Amst).*, 2015, **42**, 495–505.

5 A. Awang, S. K. Ghoshal, M. R. Sahar, M. Reza Dousti, R. J. Amjad and F. Nawaz, *Curr. Appl. Phys.*, 2013, **13**, 1813–1818.

6 R. Rajaramakrishna, S. Karuthedath, R. V Anavekar and H. Jain, *J. Non. Cryst. Solids*, 2012, **358**, 1667–1672.

7 J. W. Jeon, P. A. Ledin, J. A. Geldmeier, J. F. Ponder, M. A. Mahmoud, M. El-Sayed, J. R. Reynolds and V. V. Tsukruk, *Chem. Mater.*, 2016, **28**, 2868–2881.

8 L. Cognet, P. Tamarat and B. Lounis, *Nano Lett.*, 2005, **5**, 515–518.

9 G. Jagannath, B. Eraiah, K. NagaKrishnakanth and S. Venugopal Rao, *J. Non. Cryst. Solids*, 2018, **482**, 160–169.

10 S. K. Ghosh and T. Pal, *Chem. Rev.*, 2007, **107**, 4797–4862.

11 R. P. A. T. Castro, R. Reifenberger, E. Choi, *Phys. Rev. B*, 1990, **42**, 8548–8557.

12 T. König, R. Kodiyath, Z. A. Combs, M. A. Mahmoud, M. A. El-Sayed and V. V. Tsukruk, *Part. Part. Syst. Charact.*, 2014, **31**, 274–283.

13 H. Doweidar and Y. B. Saddeek, *J. Non. Cryst. Solids*, 2009, **355**, 348–354.

14 E. I. Kamitsos, M. A. Karakassides and G. D. Chryssikos, *J. Phys. Chem.*, 1987, **91**, 1073–1079.

15 G. D. Chryssikos, L. Liu, C. P. Varsamis and E. I. Kamitsos, *J. Non. Cryst. Solids*, 1998, **235–237**, 761–765.

16 E. I. Kamitsos, A. P. Patsis, M. A. Karakassides and G. D. Chryssikos, *J. Non. Cryst. Solids*, 1990, **126**, 52–67.

17 Y. B. Saddeek and M. S. Gaafar, *Mater. Chem. Phys.*, 2009, **115**, 280–286.

18 S. Baccaro, Monika, G. Sharma, K. S. Thind, D. Singh and A. Cecillia, *Nucl. Instruments Methods Phys. Res. Sect. B Beam Interact. with Mater. Atoms*, 2007, **260**, 613–618.

19 E. I. Kamitsos and G. D. Chryssikos, *Solid State Ionics*, 1998, **105**, 75–85.

20 Y. D. Yiannopoulos, G. D. Chryssikos and E. I. Kamitsos, *Phys. Chem. Glas.*, 2001, **42**, 164–172.

21 Manupriya, K. S. Thind, G. Sharma, V. Rajendran, K. Singh, A. V. G. Devi and S. Aravindan, *Phys. Status Solidi Appl. Mater. Sci.*, 2006, **203**, 2356–2364.

22 D. Saritha, Y. Markandeya, M. Salagram, M. Vithal, A. K. Singh and G. Bhikshamaiah, *J. Non. Cryst. Solids*, 2008, **354**, 5573–5579.

23 S. Baccaro and G. Sharma, *Nucl. Inst. Methods Phys. Res. B*, 2007, **260**, 613–618.

24 A. Egorysheva, V. Volodin and V. Skorikov, *Inorg. Mater.*, 2008, **44**, 1261–1265.

25 N. N. Ahlawat, P. Agamkar, N. Ahlawat, A. Agarwal, Monica and Rekha, *Adv. Mater. Lett.*, 2013, **4**, 71–73.

26 E. Nicolae, P. Pascuta, M. Pustan, D. R. Tamas-gavrea, L. Pop and I. Vida-simiti, *J. Non. Cryst. Solids*, 2015, **408**, 18–25.

27 B. Huang, Y. Zhou, F. Yang, L. Wu, Y. Qi and J. Li, *Opt. Mater. (Amst).*, 2016, **51**, 9–17.

28 S. Rolland, M. Tribet, P. Jollivet, C. Jégou, V. Broudic, C. Marques, H. Ooms and P. Toulhoat, *J. Nucl. Mater.*, 2013, **433**, 382–389.

29 A. Awang, S. K. Ghoshal, M. R. Sahar, R. Arifin and F. Nawaz, *J. Lumin.*, 2014, **149**, 138–143.

30 G. Senthil Murugan, *J. Non. Cryst. Solids*, 2001, **279**, 1–13.

31 K. Chrissafis and D. Bikiaris, *Thermochim. Acta*, 2011, **523**, 1–24.

32 H. Zeng, G. Chen, J. Qiu, X. Jiang and C. Zhu, *J. Non. Cryst. Solids*, 2008, **354**, 1155–1158.

33 S. Singla, O. P. Pandey and G. Sharma, *J. Non. Cryst. Solids*, 2019, **521**, 119481.

34 P. K. Jain, K. S. Lee, I. H. El-sayed and M. A. El-sayed, 2006, 7238–7248.

35 M. Peng, C. Zollfrank and L. Wondraczek, *J. Phys. Condens. Matter*, 2009, **21**, 285106.

36 M. Sheik-Bahae, A. A. Said, T. H. Wei, D. J. Hagan and E. W. Van Stryland, *IEEE J. Quantum*

Electron., 1990, **26**, 760–769.

37 T. Xu, F. Chen, X. Shen, S. Dai, Q. Nie and X. Wang, *Mater. Res. Bull.*, 2010, **45**, 1501–1505.

38 J. M. P. Almeida, D. S. Da Silva, L. R. P. Kassab, S. C. Zilio, C. R. Mendonça and L. De Boni, *Opt. Mater. (Amst).*, 2014, **36**, 829–832.

39 A. A. Scalisi, G. Compagnini, L. D’Urso and O. Puglisi, *Appl. Surf. Sci.*, 2004, **226**, 237–241.

40 X. H. Zhu, Q. Li, N. B. Ming and Z. Y. Meng, *Appl. Phys. Lett.*, 1997, **71**, 867–869.

41 Y. B. Saddeek and M. S. Gaafar, *Mater. Chem. Phys.*, 2009, **115**, 280–286.

42 G. Sharma, V. Rajendran, K. S. Thind, G. Singh and A. Singh, *Phys. B Phys. Condens. Matter*, 2009, **404**, 3371–3378.

43 S. B. Kolavekar, N. H. Ayachit, G. Jagannath, K. NagaKrishnakanth and S. Venugopal Rao, *Opt. Mater. (Amst).*, 2018, **83**, 34–42.

44 M. Parandamaiah, K. N. Kumar, S. Babu, S. V. Reddy and A. Pradesh, *Int . J. Eng. Res. Appl.*, 2015, **5**, 2248–9622.

45 A. Le Rouge, H. El Hamzaoui, B. Capoen, R. Bernard, G. Martinelli, C. Cassagne, G. Boudebs, M. Bouazaoui and L. Bigot, *Mater. Res. Express*, 2015, **2**, 1–10.

46 A. Jagannathan, R. Rajaramakrishna, K. M. Rajashekara, J. Gangareddy, V. Pattar K, V. R. S, E. B, J. Angadi V, J. Kaewkhao and S. Kothan, *J. Non. Cryst. Solids*, 2020, **538**, 120010.

47 J. F. Gomes, A. M. O. Lima, M. Sandrini, A. N. Medina, A. Steimacher, F. Pedrochi and M. J. Barboza, *Opt. Mater. (Amst).*, 2017, **66**, 211–219.

48 A. Tarafder, A. R. Molla, C. Dey and B. Karmakar, *J. Am. Ceram. Soc.*, 2013, **96**, 2424–2431.

49 I. Jlassi, H. Elhouichet and M. Ferid, *J. Mater. Sci.*, 2011, **46**, 806–812.

50 N. Mahendru, R. Bagga, K. Sharma, G. P. Kothiyal, M. Falconieri and G. Sharma, *J. Alloys Compd.*, 2014, **608**, 60–65.

51 J. Tauc and A. Menth, *J. Non. Cryst. Solids*, 1972, **8**–**10**, 569–585.

52 R. J. Amjad, M. R. Sahar, M. R. Dousti, S. K. Ghoshal and M. N. A. Jamaludin, *Opt. Express*, 2013, **21**, 14282.

53 J. E. Shelby, *Structures of glasses*, 2007.

54 M. Shapaan and F. M. Ebrahim, *Phys. B Phys. Condens. Matter*, 2010, **405**, 3217–3222.

55 S. Sindhu, S. Sanghi, A. Agarwal, V. P. Seth and N. Kishore, *Mater. Chem. Phys.*, 2005, **90**, 83–89.

56 K. Singh, *Solid State Ionics*, 1996, **93**, 147–158.

57 E. R. Shaaban, M. Shapaan and Y. B. Saddeek, *J. Phys. Condens. Matter*, 2008, **20**, 155108.

58 S. B. Mallur, T. Czarnecki, A. Adhikari and P. K. Babu, *Mater. Res. Bull.*, 2015, **68**, 27–34.

59 R. Bala, A. Agarwal, S. Sanghi and N. Singh, *Opt. Mater. (Amst).*, 2013, **36**, 352–356.

60 N. Berwal, N. Ahlawat, D. Mohan, A. Ohlan, R. Punia and N. Kishore, *Indian J. Phys.*, 2019, 1–10.

61 M. Veeramohan Rao, V. V. Ravi Kanth Kumar, N. Shihab and D. Narayana Rao, *Opt. Mater. (Amst).*, 2018, **84**, 178–183.

CHAPTER 6 RESULTS AND DISCUSSION-III

Overview

This chapter presents the importance of refractory material (SiO_2) in preventing the loss of AuNPs while preparing the glass. For this investigation, a set of bismuth borosilicate glasses with base composition $40Bi_2O_3$-$40B_2O_3$-$20SiO_2$ dispersed with 3×10^9 number of different size AuNPs are prepared using RTM. XRD revealed the amorphous nature of the synthesised glass. Presence of large number of AuNPs observed in FESEM micrographs indicate that SiO_2 effectively reduces their loss. The detected morphological changes are further supported by the thermal parameters obtained after performing DTA tests on glass powders. Prepared glass samples are characterized using UV-Vis spectroscopy to study its linear optical response whereas Z-scan measurements are carried out to expose nonlinear optical behaviour and optical quality for several applications.

6.1. Introduction

Direct incorporation of gold nanoparticles in glass has advantage over traditional methods where a gold salt is added to the precursor mixture. The gold nanoparticles are obtained with subsequent heat treatment, eventually inducing crystallization with associated scattering of light and hence resulting in reduced optical quality of material. Although, one issue faced with incorporation of as prepared nanoparticles is the reduction in concentration of gold nanoparticles that may occurs due to evaporation and oxidation during melting the batch containing nanoparticles at high temperature [1]. An effective strategy for better control on the concentration would be the use of refractory materials that protects the metallic nanoparticles form high temperature and improves their stability [2]. Among various known refractory materials, SiO_2 is widely used in the glassy system. Apart from its refractory behaviour, it is a good glass former whose presence in the glass enhances its optical efficiency. Table 6.1 displays the composition of borosilicate glass under investigation. Pictures of well-polished samples are shown in Fig. 6.1. All the results are discussed in light of effect of presence of SiO_2.

Table 6.1: Composition of the prepared glasses.

Sample label	Percentage Composition			Number of AuNPs	Size of AuNPs (nm)
	Bi_2O_3	B_2O_3	SiO_2		
BiBSi	40	40	20	-	-
BiBSi10	40	40	20	3×10^8	10
BiBSi40	40	40	20	3×10^8	40
BiBSi100	40	40	20	3×10^8	100

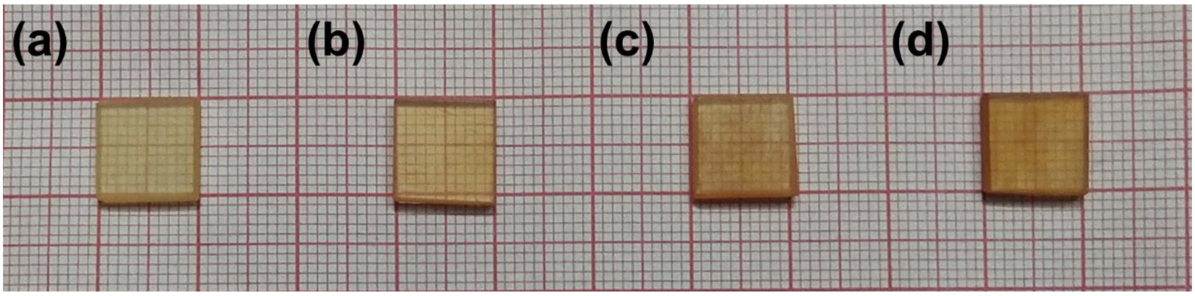

Figure 6.1: Picture of sample (a) BiBSi, (b) BiBSi10, (c) BiBSi40 and (d) BiBSi100 obtained after cutting and polishing.

6.2. Structural analysis

6.2.1. X-ray diffraction

The recorded diffraction spectra in 20° ≤ θ ≤ 80° range for bare and AuNPs dispersed bismuth borosilicate glass is shown in Fig. 6.2. Presence of broad diffuse scattering at lower angles (centred at 28° and 50°) indicates the phase separated amorphous nature of the prepared glass [3].

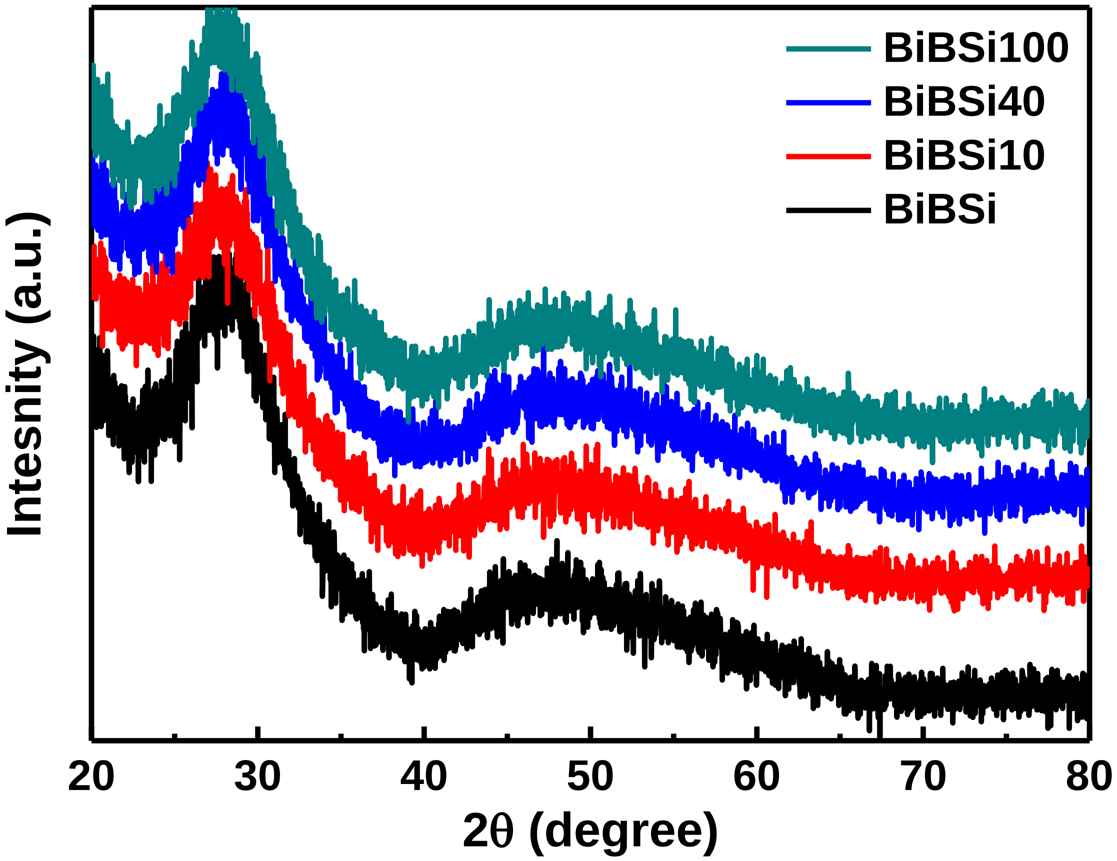

Figure 6.2: XRD pattern of bare and AuNPs dispersed bismuth borosilicate glasses.

6.2.2. Fourier Transform Infrared spectroscopy

Fig. 6.3 shows the obtained FTIR spectra of bare and AuNPs dispersed bismuth borosilicate glass in 400-1500 cm^{-1} range. All the glass samples show similar bands with subtle changes after the incorporation of AuNPs. Three bands centred at 420 cm^{-1}, 490 cm^{-1} and 570 cm^{-1} in the region 400-600 cm^{-1} appears due to stretching vibrations Bi-O-Bi linkage in BiO_6 units whereas the appearance of a strong band centred at 452 cm^{-1} in the same region can be attributed to the combination of Bi-O vibrations in BiO_6 and Si-O-Si bending vibration in SiO_4 tetrahedral units [4–6]. Another strong band centred at 694 cm^{-1} is assigned to bending vibrations of B-O-B units borate network [7,8]. Whereas, shoulder at 850 cm^{-1} represents the symmetric vibrations of Bi-O in BiO_3 units [9,10]. Two major bands centred at 930 cm^{-1} and 1310 cm^{-1} reveals the stretching vibrations of B-O-B in BO_4 and BO_3 units, respectively [7,11,12]. Further, superimposed effect of asymmetric vibrations of B-O linkage in BO_4 units and Si-O-Si linkage is observed at 1065 cm^{-1} [5,13]. Addition of AuNPs in the glass results in the appearance of a new shoulder at 1220 cm^{-1} that represents the B-O stretching vibrations in $(BO)^{3-}$ non-bridging units [9,14]. Peaks becomes more prominent due to enhanced intensity after the incorporation of AuNPs that directly confirms the formation of non-bridging oxygens inside the glassy matrix.

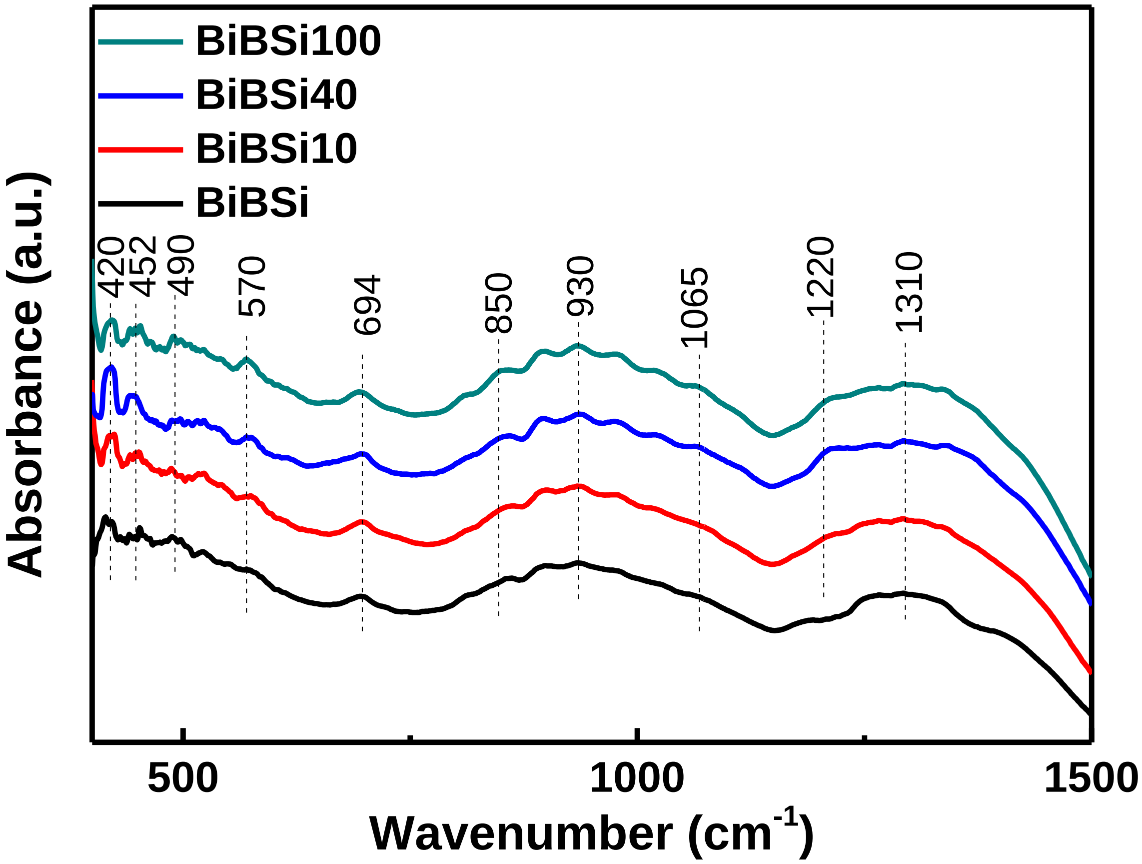

Figure 6.3: The infrared spectra of bismuth borosilicate glasses containing AuNPs.

6.3. Morphological studies

6.3.1. Field emission scanning electron microscopy

FESEM micrograph of prepared bismuth borosilicate glasses are shown in Fig 6.4. Fig 6.4 (a) shows the base glass matrix only while Fig 6.4 (b)-(d) confirms the existence of large number of distorted spherical shaped AuNPs inside the glass. The refractory property of SiO_2 protected the AuNPs from high temperature while melting the glass and prevented its loss by evaporation or oxidation. Whereas, these incorporated AuNPs gets coagulated inside the glass in order to reduce the surface stresses (Ostwald's ripening) and results in the formation of huge clusters. The average particle size calculated is 50 nm, 180 nm and 250 nm for BiBSi10, BiBSi40 and BiBSi100, respectively. The recorded EDS spectrum of BiBSi10 (Figure 6.4 (e)) confirms the existence of Bismuth, Silicon, Oxygen and Gold inside the prepared glass sample.

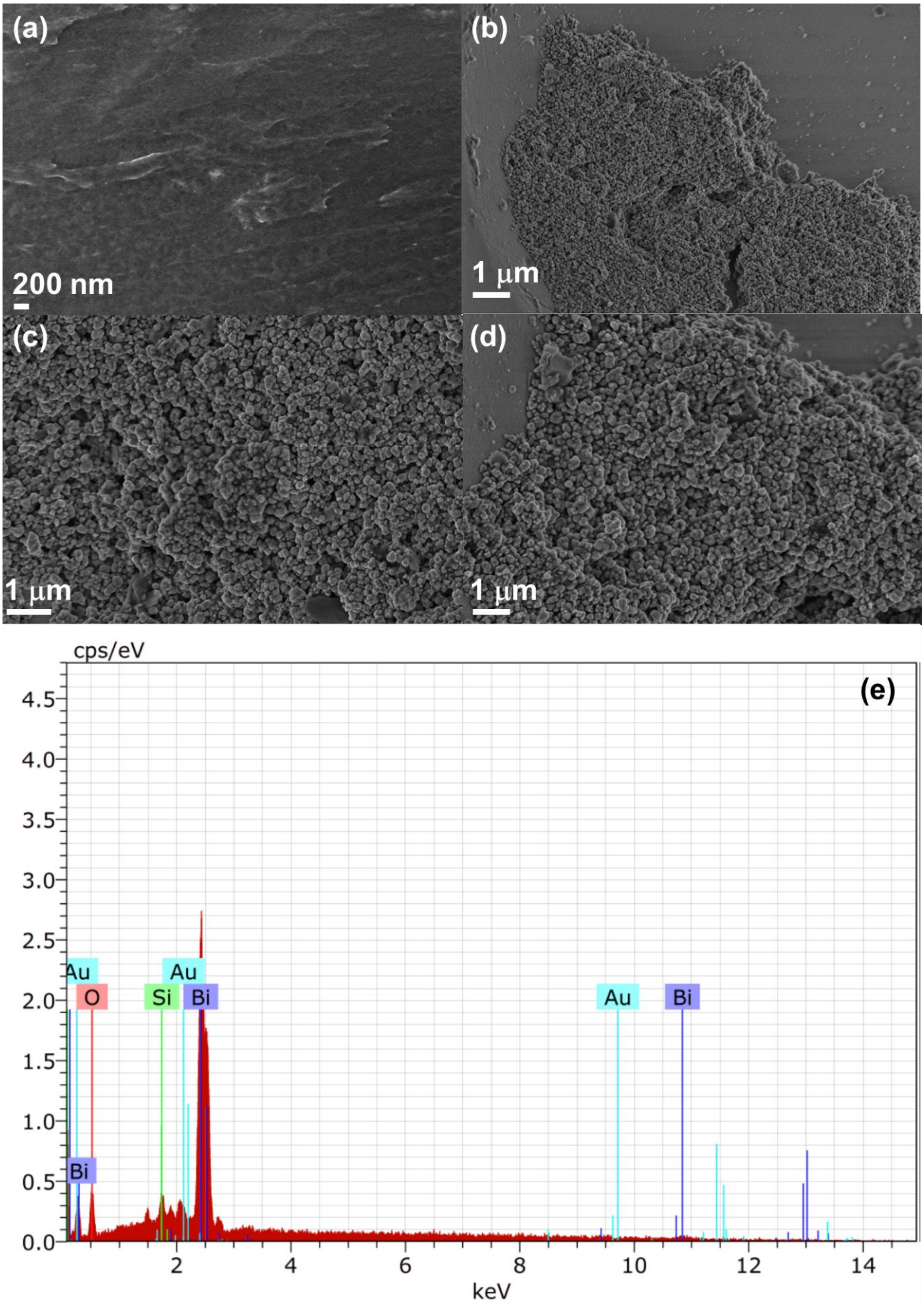

Figure 6.4: FESEM micrographs of (a) BiBSi, (b) BiBSi10, (c) BiBSi40 and (d) BiBSi100. Where (e) is the EDS spectrum of BiBSi10 that shows the presence of Different elements.

6.4. Physical properties of glass

Fig. 6.1 evidences the colour change from light yellow to dark orange with the progressive increase in size of incorporated AuNPs. This change in colour can be explained on the basis of increase in density discussed in forthcoming section.

6.4.1. Density measurements

Measured density values are reported in Table 6.2. The density of glass first decreases from 6.23 gcm^{-3} to 6.17 gcm^{-3} with the addition of 10 nm size AuNPs whereas with further increase in size of incorporated AuNPs, the density increases upto 6.27 gcm^{-3}. Incorporation of AuNPs results in the formation of non-bridging oxygen that decreases the density of glass. Whereas, particles with increased size occupies more space in the structure and compensates the effect of formation of non-bridging oxygen leading to increased density. This increased density further results in sample colour change.

Table 6.2: Measured physical, optical and thermal properties of prepared bismuth borosilicate glass samples.

Properties	BiBSi	BiBSi10	BiBSi40	BiBSi100
Physical properties				
Density, ρ (gcm^{-3}) ± 1%	6.23	6.17	6.22	6.27
Optical properties				
Optical band gap, E_o (eV)	3.06	3.03	3.01	3.00
Refractive index, n_o	2.38	2.38	2.39	2.40
Thermal Properties				
Glass transition temperature, T_g (°C)	391	387	379	375
Glass melting temperature, T_m (°C)	715	715	715	715

6.5. Thermal properties

6.5.1. Differential thermal analysis

Fig. 6.5 represents the DTA profile of bismuth borosilicate glass dispersed with AuNPs. Thermal parameters obtained after analysing the DTA curve are listed in Table 6.2. The lower glass transition temperature of bismuth borosilicate glass as compare to bismuth borate glass results in enhanced coagulation that can be seen from FESEM results. Observed decrease in glass transition temperature with the addition of AuNPs is attributed to the formation of non-bridging oxygens inside the glass which is in agreement with the obtained density results. Also, decreased glass transition temperature with the addition of AuNPs results in reduction of glass forming ability and stability. Whereas no change in glass melting temperature is observed.

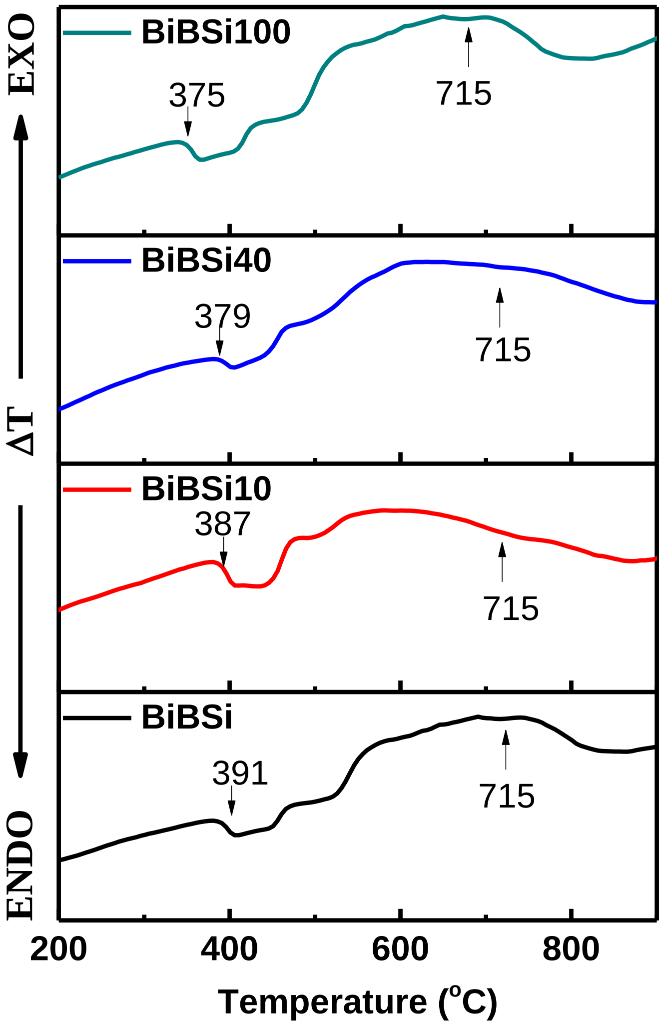

Figure 6.5: DTA profile of bare and AuNPs dispersed 40Bi_2O_3-40B_2O_3-20SiO_2 glasses.

6.6. Optical Properties

6.6.1. Uv-Vis-NIR spectroscopy

Measured transmission spectra in visible and near infrared region (200-800 nm) are exhibited in Fig. 6.6 (a), showing transparency in 200-400 nm for all the samples. Absorption and scattering of light associated with AuNPs results in fair decrease of percentage transmission from 71% for BiBSi to 45% for BiBSi100. Scattering efficiency increases with increase in particle size that results in decreased transmission with increase in size of AuNPs [15]. Presence of Bi active centres in the glass is evidenced by the existence of transmission dip around 465 nm [16].

Fig. 6.6 (b) displays the plot for $(\alpha h\nu)^{1/2}$ vs hν and the value of optical band gap obtained after extrapolating for $(\alpha h\nu)^{1/2} = 0$ are enlisted in Table 6.2. Formation of non-bridging oxygens revealed from FTIR, density and thermal analysis results in decrease of optical band gap from 3.06 eV to 3.00 eV with the addition of AuNPs.

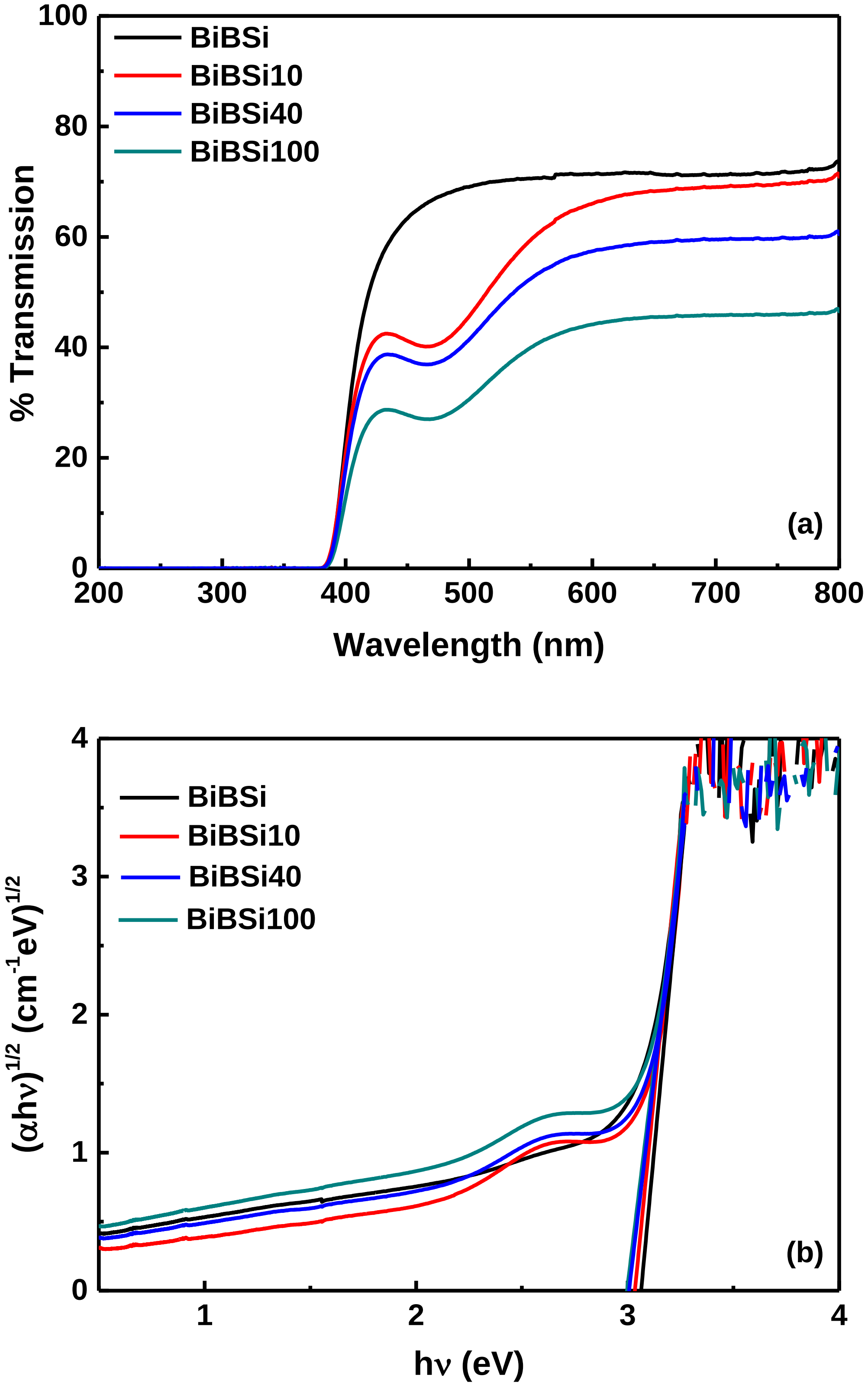

Figure 6.6: (a) Transmission spectra and (b) Tauc's plot for bare and AuNPs dispersed bismuth borosilicate glass samples.

6.6.2. Z-scan

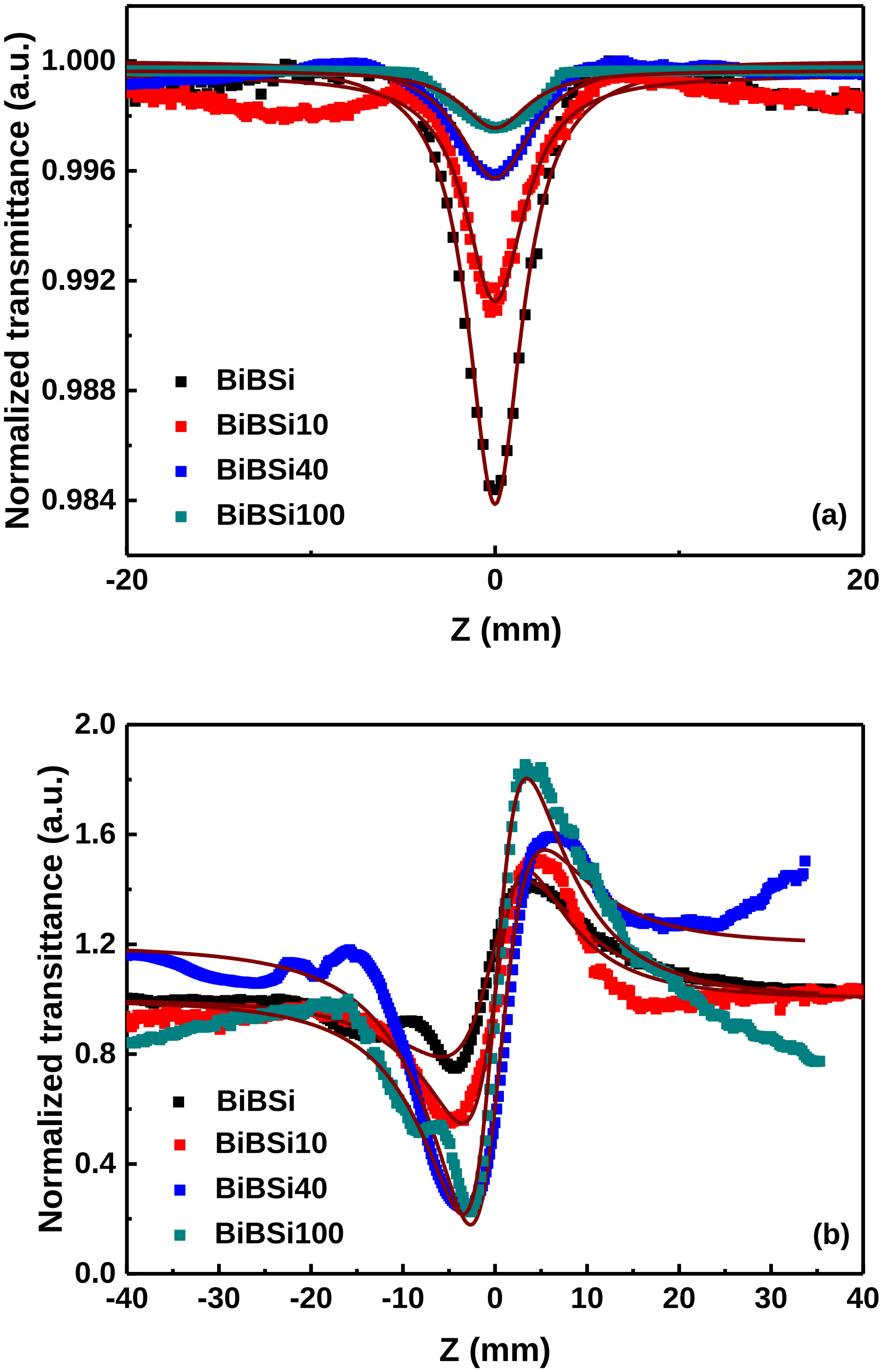

Figure 6.7: (a) Open aperture and (b) Closed aperture Z-scan curves taken at 800 nm. The solid square dots are the obtained experimental data whereas solid lines represents the theoretical fit.

Fig. 6.7 (a) and (b) displays the obtained OA and CA Z-scan data, respectively along with the theoretical fit. Observed decrease in transmission close to focal point in OA Z-scan evidences the existence of reverse saturable absorption (RSA) via two photon absorption (2PA) since all the samples satisfies the condition $0.5< h\nu/E_o<1$ [17]. Moreover, the observed prefocal valley followed by post focal dip in CA Z-scan data confirms the occurrence of self-defocusing phenomena leading to positive type of nonlinearity. Also, peak-valley distance in CA Z-scan fulfils the condition $\Delta z \sim 1.7z_o$, hence confirming the existence of pure electronic third-order nonlinearity [6]. The obtained OA and CA experimental Z-scan data is fitted using Eq. (3.7) and (3.8), respectively. The values of nonlinear absorption coefficient (β) and nonlinear refractive index (n_2) so obtained are presented in Table 6.3. Moreover, calculated values of nonlinear susceptibility (χ_3) and figure of merit (F, W, T) are included in Table 6.3.

The presence of highly polarizable oxide (Bi_2O_3) in the glass results in existence of sufficiently large value of nonlinear parameter whereas electronic transitions in corresponding cations (Bi^{3+}) induces 2PA. Decrease in nonlinear absorption coefficient absorption coefficient from 2.0×10^{-13} to 1.4×10^{-13} m/W with the addition of AuNPs is attributed to the suppression of electronic states by trapping of free electrons due to non-resonant excitation. This suppression increases with increase in size of AuNPs leading to decrease in 2PA coefficient upto 5.6×10^{-14} m/W. Moreover, the enhanced electric field due to surface plasmon resonances associated with AuNPs results in increased nonlinear refractive index from 2.5×10^{-12} to 4.8×10^{-12} m^2/W. This increase may also be attributed to the formation of non-bridging oxygens after the addition of AuNPs which are highly polarizable in nature [18].

Table 6.3. Nonlinear absorption coefficient (β), nonlinear refractive index (n_2), nonlinear susceptibility (χ_3) and figure of merits (F, W, T) obtained after fitting Z-scan data of bismuth borosilicate glass.

Sample	**β (m/W)**	**n_2 (m^2/W)**	**$\lvert\chi^{(3)}\rvert$ (esu)**	**F**	**W**	**T**
BiBSi	2.0×10^{-13}	1.7×10^{-18}	2.5×10^{-12}	5.4	>1	0.09
BiBSi10	1.4×10^{-13}	2.0×10^{-18}	2.9×10^{-12}	8.7	>1	0.06
BiBSi40	8.5×10^{-14}	2.9×10^{-18}	4.2×10^{-12}	21.2	>1	0.02
BiBSi100	5.6×10^{-14}	3.2×10^{-18}	4.8×10^{-12}	36.7	>1	0.01

References:

1 A. Le Rouge, H. El Hamzaoui, B. Capoen, R. Bernard, G. Martinelli, C. Cassagne, G. Boudebs, M. Bouazaoui and L. Bigot, *Mater. Res. Express*, 2015, **2**, 1–10.

2 S. Singla, O. P. Pandey and G. Sharma, *J. Non. Cryst. Solids*, 2019, **521**, 119481.

3 J. E. Shelby, *Structures of glasses*, 2007.

4 D. Saritha, Y. Markandeya, M. Salagram, M. Vithal, A. K. Singh and G. Bhikshamaiah, *J. Non. Cryst. Solids*, 2008, **354**, 5573–5579.

5 H. A. Saudi, H. A. Sallam and K. Abdullah, 2014, **2**, 20–24.

6 N. Berwal, N. Ahlawat, D. Mohan, A. Ohlan, R. Punia and N. Kishore, *Indian J. Phys.*, 2019, 1–10.

7 S. Song, Z. Wen and Y. Liu, *Mater. Lett.*, 2010, **64**, 1025–1027.

8 S. B. Kolavekar, N. H. Ayachit, G. Jagannath, K. NagaKrishnakanth and S. Venugopal Rao, *Opt. Mater. (Amst).*, 2018, **83**, 34–42.

9 X. Zhu, C. Mai and M. Li, *J. Non. Cryst. Solids*, 2014, **388**, 55–61.

10 K. Singh, *Solid State Ionics*, 1996, **93**, 147–158.

11 D. Möncke, D. Ehrt and E. I. Kamitsos, *Phys. Chem. Glas. Eur. J. Glas. Sci. Technol. Part B*, 2013, **54**, 42–51.

12 K. El-Egili, *Phys. B Condens. Matter*, 2003, **325**, 340–348.

13 A. V Egorysheva, V. D. Volodin and V. M. Skorikov, *Inorg. Mater.*, 2008, **44**, 1261–1265.

14 D. Möncke, D. Ehrt, C. P. E. Varsamis, E. I. Kamitsos and A. G. Kalampounias, *Glas. Technol. Eur. J. Glas. Sci. Technol. Part A*, 2006, **47**, 133–137.

15 P. K. Jain, K. S. Lee, I. H. El-sayed and M. A. El-sayed, 2006, 7238–7248.

16 M. Peng, C. Zollfrank and L. Wondraczek, *J. Phys. Condens. Matter*, 2009, **21**, 285106.

17 R. Bala, A. Agarwal, S. Sanghi and N. Singh, *Opt. Mater. (Amst).*, 2013, **36**, 352–356.

18 M. Veeramohan Rao, V. V. Ravi Kanth Kumar, N. Shihab and D. Narayana Rao, *Opt. Mater. (Amst).*, 2018, **84**, 178–183.

CHAPTER 7 RESULTS AND DISCUSSION-IV

Overview

This chapter reports the role of different stabilizers (Eu_2O_3, EuF_3 and KSCN) in stabilizing AuNPs embedded in Bismuth-Borosilicate glasses. The prepared nanocomposites are characterized by XRD, FTIR, FESEM, HRTEM, DTA, UV–Visible transmission spectroscopy and Z- scan. From FESEM, it has been observed that the morphology of AuNPs is highly dependent on the type of stabilizer used. Also HRTEM confirms the covering of AuNPs by stabilizer that prevents the coagulation of NPs. The localized surface plasmon resonance related transmission dip is observed around 585 nm for glass containing Eu_2O_3 as a stabilizer. The nonlinear refractive index and nonlinear absorption coefficient for the prepared glasses is obtained from CA and OA Z-scan measurements, respectively. All the Z-scan measurements have been carried out at input peak intensity of 14.38 GW/cm^2. Nonlinear optical studies with open aperture Z-Scan shows the switching between saturable absorption and two photon absorption as the laser intensity is increased. The existence of third order nonlinearity has been detected using closed aperture Z-scan in the prepared glasses.

7.1. Introduction

Evaporation and Ostwald ripening are the two main issues faced while incorporating the metallic gold nanoparticles during glass preparations. An effective solution to evaporation is the use of refractory material discussed in previous chapter in detail. Ostwald ripening is the phenomena in which the smaller metallic nanoparticles combine to form bigger ones in order to overcome the extra stresses on the surface and leads to loss of their identity [1]. Addition of rare earth elements and negatively charged species along with the nanoparticles could form a covering around them to prevent Ostwald's ripening [2]. Moreover, inclusion of metal NPs along with lanthanides in the glass matrix is interesting as they are found to improve the linear and nonlinear optical properties of glasses [3–5]. Local electric fields produced by surface plasmon resonances and the energy transfer between rare earth (RE) and metallic NPs in turn act on RE atoms and modify the luminescent properties [6,7]. As the localized surface plasmon resonance (LSPR) of NPs depend on the host material, size, shape and morphology of metal NPs, the luminescent properties can be modulated by LSPR mediation [8–10].

In the present study, Bismuth Borosilicate glasses are prepared using conventional melt quench technique in which AuNPs have been directly incorporated while mixing the raw materials. In order to achieve the required stability of AuNPs inside the glass, different stabilizers (Eu_2O_3, EuF_3 and KSCN) have been used. The composition of Au doped glass samples H–Eu_2O_3–Au, G-EuF_3-Au and J-KSCN-Au along with their corresponding undoped matrices H–Eu_2O_3, G-EuF_3 and J-KSCN, respectively, has been given in Table 7.1. The prefix H, G and J are used here just to label the sample. The pictures of samples obtained after cutting and polishing are displayed in Fig. 7.2.

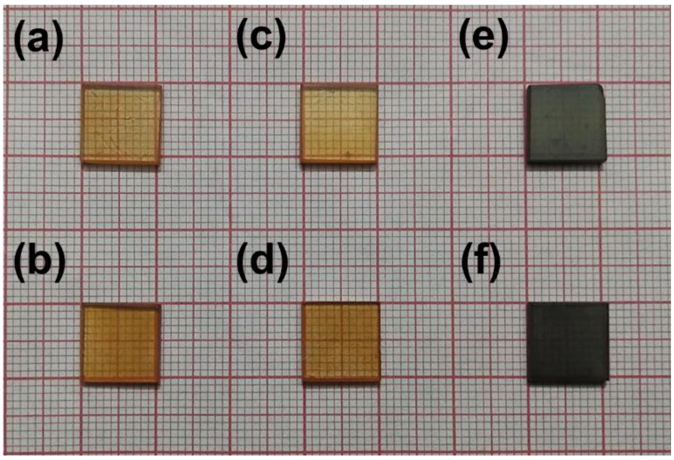

Figure 7.1: Pictures of well-polished (a) H-Eu_2O_3, (b) H-Eu_2O_3-Au, (c) G-EuF_3, (d) G-EuF_3-Au, (e) J-KSCN and (f) J-KSCN-Au glass samples.

Table 7.1: Composition of the prepared glasses.

Sample name	**Composition (mol %)**						**Number of AuNPs**
	Bi_2O_3	**B_2O_3**	**SiO_2**	**Eu_2O_3**	**EuF_3**	**KSCN**	
H-Eu_2O_3	39	40	20	1	-	-	-
H-Eu_2O_3-Au	39	40	20	1	-	-	3×10^9
G-EuF_3	39	40	20	-	1	-	-
G-EuF_3-Au	39	40	20	-	1	-	3×10^9
J-KSCN	39	40	20	-	-	1	-
J-KSCN-Au	39	40	20	-	-	1	3×10^9

7.2. Structural analysis

7.2.1. X-ray diffraction

XRD patterns of the prepared glass samples are represented in Fig. 7.2 and in all the cases, patterns are nearly same. It can be clearly seen that the plot contains two broad humps for H-Eu_2O_3, H-Eu_2O_3-Au, G-EuF_3, G-EuF_3-Au, J-KSCN and J-KSCN-Au between 30° and 50° without any crystallization peak. Absence of crystallization peaks confirm the amorphous nature of the glasses studied. No peak corresponding to AuNPs appears in the spectra of glasses containing gold since the concentration of gold is very low. Ghoshal *et al.* and Awang *et al.* reported similar observations in their earlier work [2,11].

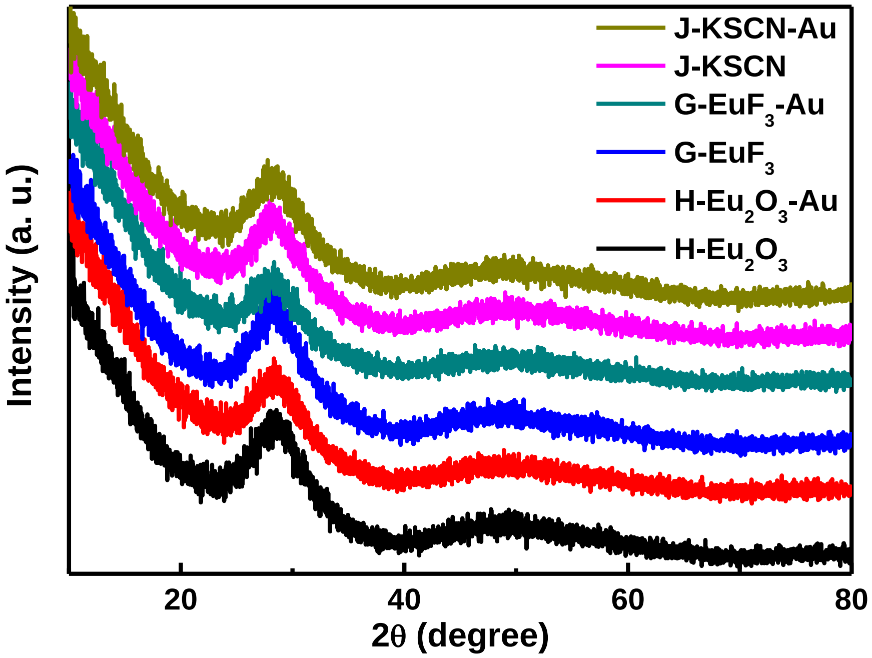

Figure 7.2: X-ray diffractogram of the prepared glass samples H-Eu_2O_3, H-Eu_2O_3-Au, G-EuF_3, G-EuF_3-Au, J-KSCN and J-KSCN-Au. Curves are shifted vertically for better visibility.

7.2.2. Fourier Transform Infrared spectroscopy

The FTIR spectra of undoped and doped Bismuth Borosilicate glass containing different stabilizers i.e. Eu_2O_3, EuF_3 and KSCN is shown in Fig. 7.3. The FTIR spectra of the glass under supervision have been recorded in the range of 400-4000 cm^{-1} and the active vibrational IR bands assigned to [BO_n, n = 3 and/or 4], [BiO_n, n =3 and 6] and [SiO_4] structural units, are located in the mid infrared region, i.e. in the spectral range 1600–400 cm^{-1} [12]. It is observed that the three prominent absorption bands in the region 600-800 cm^{-1}, 800-1200 cm^{-1} and 1200-1500 cm^{-1} are shown by all the glasses which is a characteristic feature of borate glass.

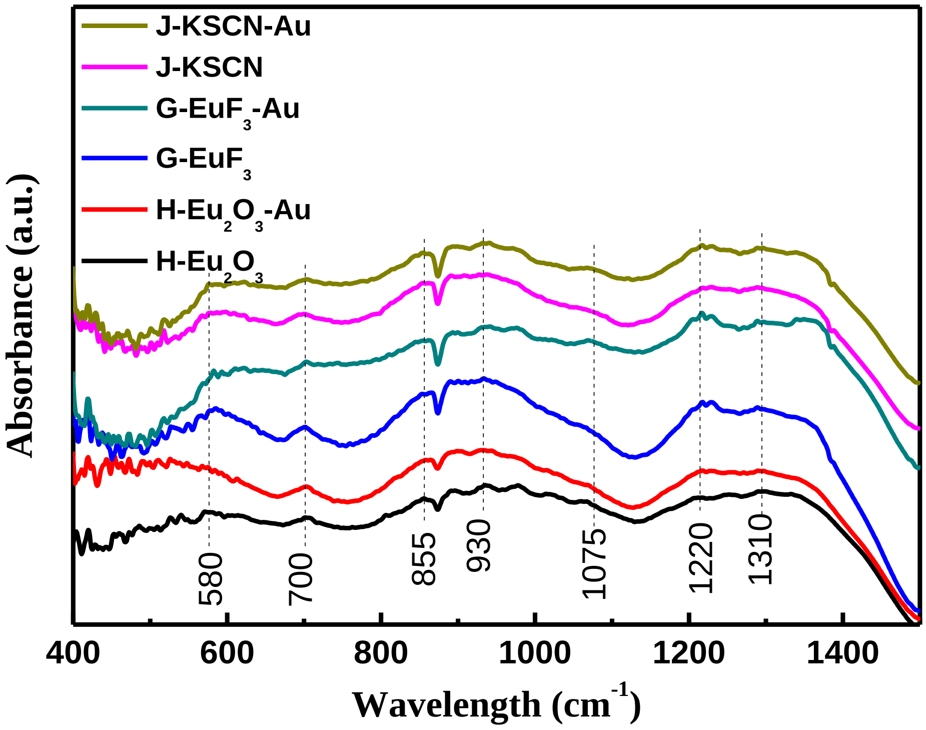

Figure 7.3: FTIR spectra of glass samples in the range of 400-1500 cm^{-1}.

For the prepared glass sample peak centered at 580 cm^{-1} in the region 400-600 cm^{-1} are attributed to the combined vibrations of vibration of Bi-O bonds in BiO_6 octahedral units and Si-O bonds in SiO_4 units [13,14]. The vibration of B-O-B in BO_3 triangles is confirmed by the presence of peak at 700 cm^{-1} [15–18] whereas the presence of clear peak at 930cm^{-1} confirms the B-O bond stretching of tetrahedral BO_4 units [14,15,19]. A shoulder appears at 855 cm^{-1} due to symmetric vibrations of Bi-O linkage in BiO_3 units. Moreover, a weak peak centred at 1075 cm^{-1} exists due to combined effect of asymmetric B-O band vibrations in BO_4 and Si-O-Si vibrations in silica network. Another broad band centred at 1310 cm^{-1} verifies the stretching vibrations of B-O units of trigonal BO_3 [17,20]. On comparison of structural changes for the glass with and without AuNPs, it is seen (Fig. 7.3) that no prominent change has been observed with the addition of AuNPs while the peak centred at 1225 cm^{-1} becomes more intense that confirms the formation of non-bridging oxygens inside the glass.

7.3. Morphological studies

7.3.1. Field emission scanning electron microscopy

The FESEM images of prepared glass samples having Eu_2O_3 as a stabilizer in it are shown in Fig. 7.4 (a) and (b) which show randomly distributed AuNP particles inside the glass [21]. The size of the AuNPs estimated from FESEM images is about 40 nm and the average particle density is 2 μm^{-2}. Fig. 7.4 (c) and (d) display the FESEM image of G-EuF_3 and G-EuF_3-Au samples in which few gold regions are seen. Moreover, FESEM image of glass J-KSCN-Au having KSCN as a stabilizer (Fig. 7.4 (e) and (f)) shows the presence of AuNPs of nearly 40 nm and having particle density 0.1 μm^{-2}. In both H-Eu_2O_3-Au and J-KSCN-Au, no clustering of AuNPs is observed which can be explained on the basis of encapsulation of AuNPs by Eu_2O_3 and KSCN that is further supported by HRTEM analysis discussed in the section below. The EDS spectrum of G-EuF_3-Au shown in Fig. 7.4 (g) confirms the presence of Bismuth, Silicon, Fluorine, Gold, Oxygen and Europium in the glass.

Luo *et al.* [22] reported that the bond dissociation energy of Eu-F and Eu-O is 544 and 473 KJ/mol, respectively and that of KSCN is 337 KJ/mol as reported by Basch *et* al. [23]. From the above mentioned data it is clear that the bond strength between Eu-F is strong and also the electron affinity of F is very high which does not favour the formation of Au-F. On the other hand, the Au-Au bonding occurs and leads to agglomeration inside the glass. The strong bonding and segregation of Eu-F can also be evidenced from Fig. 7.4 (c) where small black spots have been observed in the glass without AuNPs [24]. Unlike the Eu-F case, the low bond strength of Eu-O and KCN-S results in their bond breakage and O or S gets attached to Au. These attached O and S with Au prevents Ostwald ripening and hence reduces the coagulation.

7.3.2. High resolution transmission electron microscopy

In order to verify the presence of Eu_2O_3 around the NPs and to confirm the stabilizing properties of the same, HRTEM images have been taken for the sample H-Eu_2O_3-Au and shown in Fig 7.5. Fig. 7.5 (a) shows (TEM image taken at comparatively low resolution) that sample has nearly spherical shaped particles with average particle size of 40 nm and is in agreement with FESEM result. HRTEM image is represented in Fig. 7.5 (b) that shows a clear

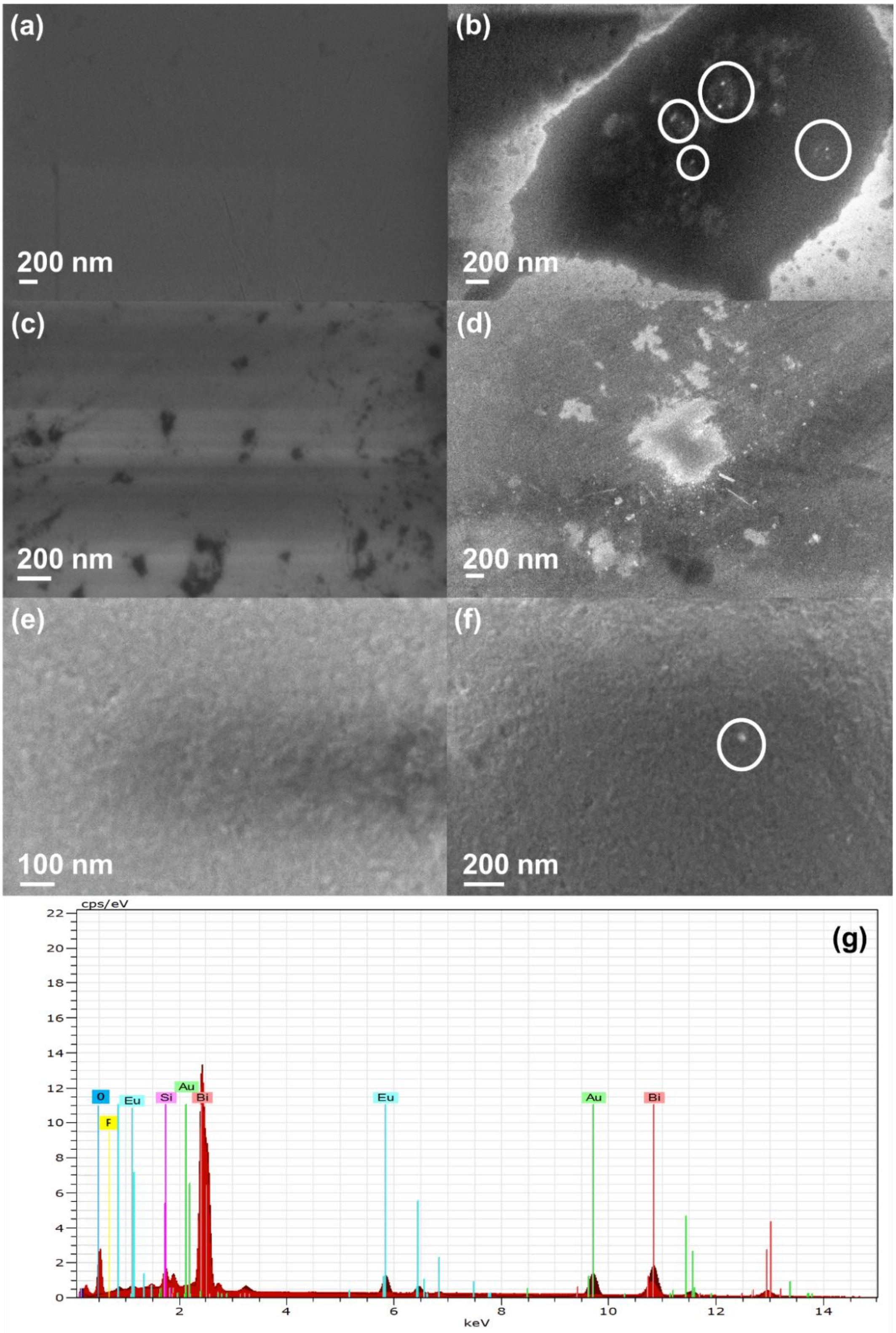

Figure 7.4: FESEM images of (a) H-Eu_2O_3 containing Eu_2O_3 without AuNPs, (b) H-Eu_2O_3-Au containing Eu_2O_3 with AuNPs, (c) G-EuF_3 containing EuF_3 without AuNPs, (d) G-EuF_3-Au containing EuF_3 with AuNPs, (e) J-KSCN containing KSCN without AuNPs and (f) J-KSCN-Au containing KSCN with AuNPs. The NPs are highlighted by circles. (g) EDS spectrum of G-EuF_3-Au showing presence of different elements in the glass.

light coloured boundary around the nanoparticle where the boundary is highlighted with green square box. Moreover, the measured inter-reticular spacing for AuNP (highlighted with red box) is 2.41 Å that progressively moves to 3.10 Å as we go to boundary of the particle. These lattice fringes correspond to (111) plane of cubic gold and (111) plane of Eu_2O_3 with reference to ICDD 00-004-0784 and 03-065-3182 respectively. Rouge *et. al.* [25] have also reported the similar results of presence of Zirconia around the gold.

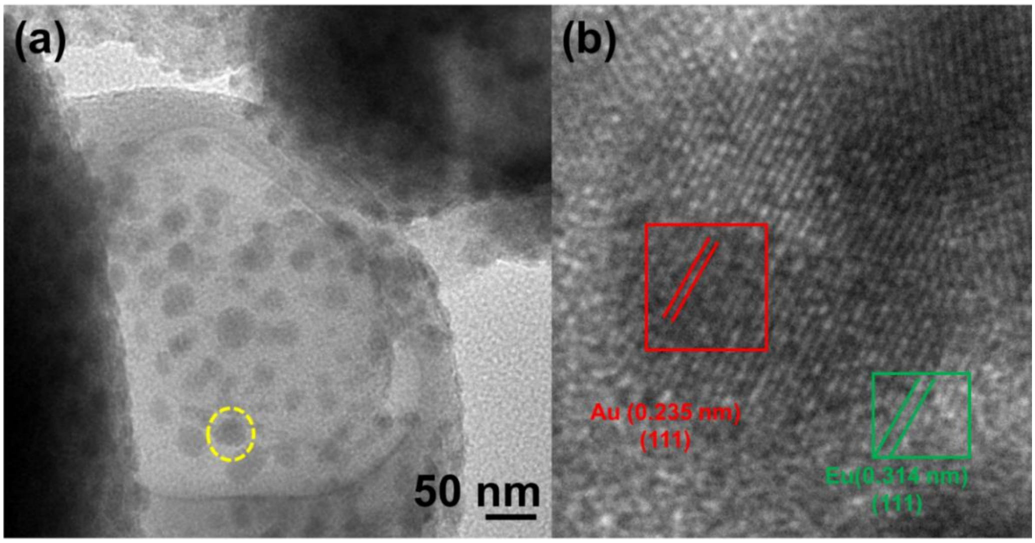

Figure 7.5: (a) represents the TEM image of H-Eu_2O_3-Au and (b) is the magnified view of marked region on (a). Red and green boxes are used to highlight the fringes of Au and Eu_2O_3.

7.4. Physical properties of glass

7.4.1. Density measurements

The measured density values for all the samples under investigation are given in Table 7.2. Slight decrease in density with the addition of AuNPs is observed with respect to glass without AuNPs for all three type of stabilizers. This decrease is attributed to the participation of AuNPs in structural modifications and the formation of non-bridging oxygens inside the glassy matrix.

Table 7.2: Measured physical, optical and thermal properties for the prepared glass samples containing different stabilizers.

Sample code	**ρ (cm^{-3})**	**E_o (eV)**	**n**	**Thermal parameters °C**				**$\Delta T = T_x - T_g$**	**K_w**
				T_g	**T_x**	**T_p**	**T_m**		
H-Eu_2O_3	7.00	2.93	2.42	399	547	557	610	148	0.24
H-Eu_2O_3-Au	6.97	2.92	2.42	399	555	565	610	156	0.26
G-EuF_3	6.98	2.94	2.41	396	557	573	603	161	0.27
G-EuF_3-Au	6.96	2.92	2.42	396	557	573	603	161	0.27
J-KSCN	6.92	2.90	2.42	396	548	557	603	152	0.25
J-KSCN-Au	6.83	2.86	2.44	396	552	561	603	156	0.26

7.5. Thermal properties

7.5.1. Differential thermal analysis

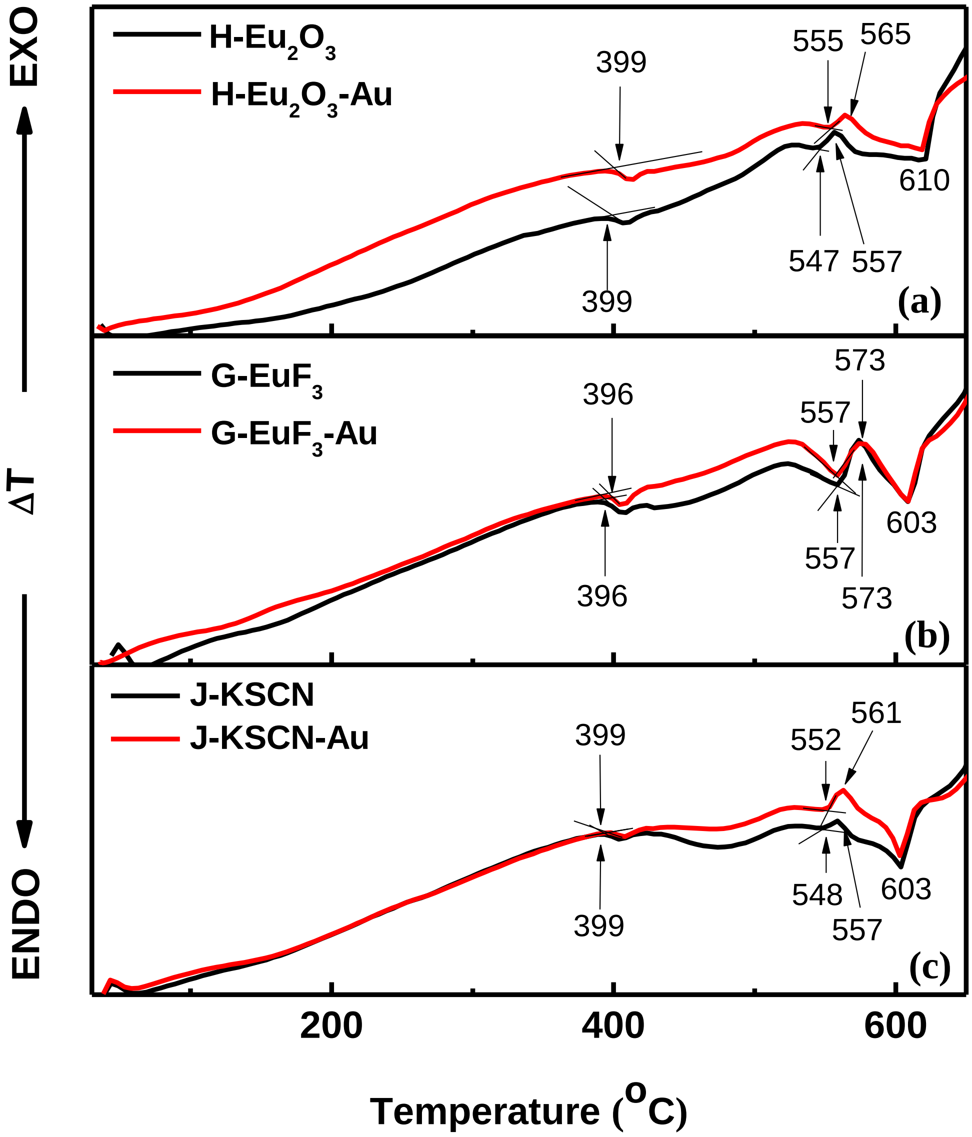

Figure 7.6: Shown are the thermographs for (a) H-Eu$_2$O$_3$ and H-Eu$_2$O$_3$-Au, (b) G-EuF$_3$ and G-EuF$_3$-Au and (c) J-KSCN and J-KSCN-Au taken in the temperature range of 30 ^{0}C to 600 ^{0}C.

Figs. 7.6 (a), (b) and (c) shows the DTA thermographs of the prepared glass samples containing Eu$_2$O$_3$, EuF$_3$ and KSCN, as stabilizers with and without AuNPs, respectively. The obtained values of glass transition temperature (T_g), crystallization onset temperature (T_x), crystallization peak temperature (T_p), glass melting temperature (T_m) and stability factor (ΔT) are given in Table. 7.2. Glass transition temperature (T_g) of the glasses containing AuNPs remains the same in comparison to their respective base glasses (Table. 7.2). The area under the crystallization peak increases with the addition of AuNPs in all samples. Moreover, the glasses with Eu_2O_3 and KSCN show increase in peak crystallization temperature (T_p) upon the addition of AuNPs whereas no change is observed for glasses doped with EuF_3. Lower T_g observed for sample containing EuF_3 supports the coagulation which is in agreement with FESEM results. The glass forming ability calculated using ΔT, is maximum for G-EuF_3 and least for H-Eu_2O_3. The higher value of ΔT (Table. 7.2) shows good glass forming ability of the prepared glass samples [2].

7.6. Optical Properties

7.6.1. Uv-Vis-NIR spectroscopy

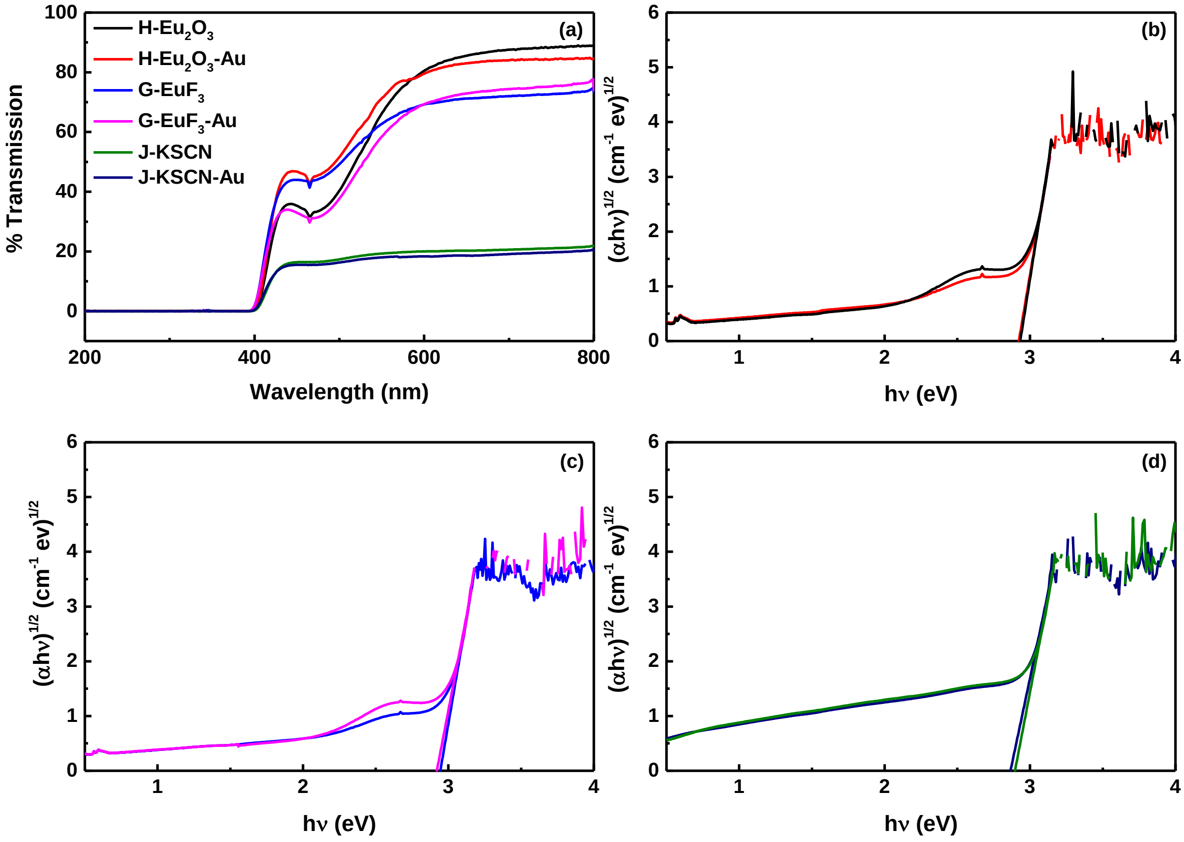

Figure 7.7: (a) Transmission spectra of prepared glass samples and Tauc's plot for (a) H-Eu_2O_3 and H-Eu_2O_3-Au, (b) G-EuF_3 and G-EuF_3-Au, and (c) J-KSCN and J-KSCN-Au.

UV-Visible absorption spectroscopy shows that the variation in absorption with the addition of AuNPs as compared to their respective base glass is negligibly small. A small absorption peak at about 585 nm for H-Eu_2O_3-Au is attributed to LSPR and the peak at 465 nm for all samples is related to the presence of Bi ions [24]. The LSPR peak in H-Eu_2O_3-Au (Fig. 7.7) is an evidence for the high stabilizing action of Eu_2O_3 among the three stabilisers used. No such LSPR peak has been observed in G-EuF_3-Au and J-KSCN-Au which confirms the absence or low concentration of AuNPs inside the prepared glasses, respectively.

Optical band gap obtained after extrapolation the Tauc's plot at $(\alpha h\nu)^{1/2} = 0$ as given in Table 7.2 shows a decrease with the incorporation of AuNPs. Formation of non-bridging oxygens after the incorporation of AuNPs results in the observed decrease.

7.6.2. Photoluminescence

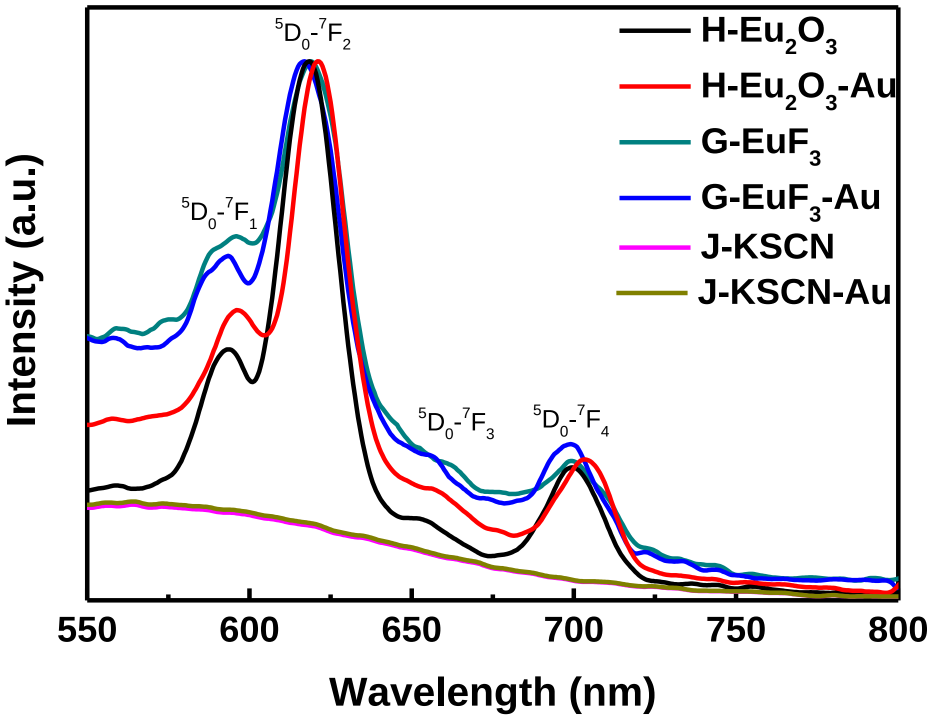

Figure 7.8: Visible emission spectra of all the glasses under excitation of 390 nm. Obtained spectra are normalized with respect to peak centred at 620 nm.

Fig. 7.8 represents the emission spectra recorded in the range of 550-800 nm for bare and AuNPs dispersed glass samples. All the samples were excited under 390 nm excitation wavelength using Xenon lamp. The luminescence spectra of the glasses containing Eu_2O_3 and EuF_3 consist of emission peaks in the region 570-700 nm. The major intense peaks are centred at 596, 620, 650 and 700 nm, corresponding to $^5D_0 \rightarrow$ $^7F_1$, $^7F_2$, $^7F_3$ and $^7F_4$ transitions of Eu^{3+} ions, respectively [26,27]. The most intense peak is found at 620 nm that correspond to electric-dipole (ED) transition. This transition is hypersensitive in nature and highly dependent on the local environment of Eu ions in the host matrix. The emission peaks corresponding to $^5D_0$-$^7F_{1,2,3,4}$ are not observed in the sample J-KSCN and J-KSCN-Au due to absence of rare earth (Eu) in the glasses. It is worth noting that sharper peaks were found for samples containing

Eu_2O_3 as compared to samples containing EuF_3. This may be due to the uniform distribution of stabilizer in the glass H-Eu_2O_3 [28]. These results are in strong agreement with the FESEM micrographs.

It is observed in Fig. 7.8 that the presence of AuNPs along with Eu_2O_3 results in enhanced emission intensity of glass H-Eu_2O_3-Au. More specifically, 2-fold enhancement in intensity of emission peaks for sample H-Eu_2O_3-Au is observed as compared to the H-Eu_2O_3 glass sample. This intensity enhancement is associated partially with the induced local field around the Eu^{3+} ions in the vicinity of AuNPs and the energy transfer among AuNPs and Eu^{3+} ions [29,30]. Fig. 7.9 represents the schematic luminescence mechanism observed in the synthesized glasses. Due to poor stabilizing effect of EuF_3, clustering of AuNPs is observed as shown in FESEM images of G-EuF_3-Au (Fig. 7.4 (d)). Therefore, no such luminescence enhancement is observed in G-EuF_3-Au even after the addition of AuNPs.

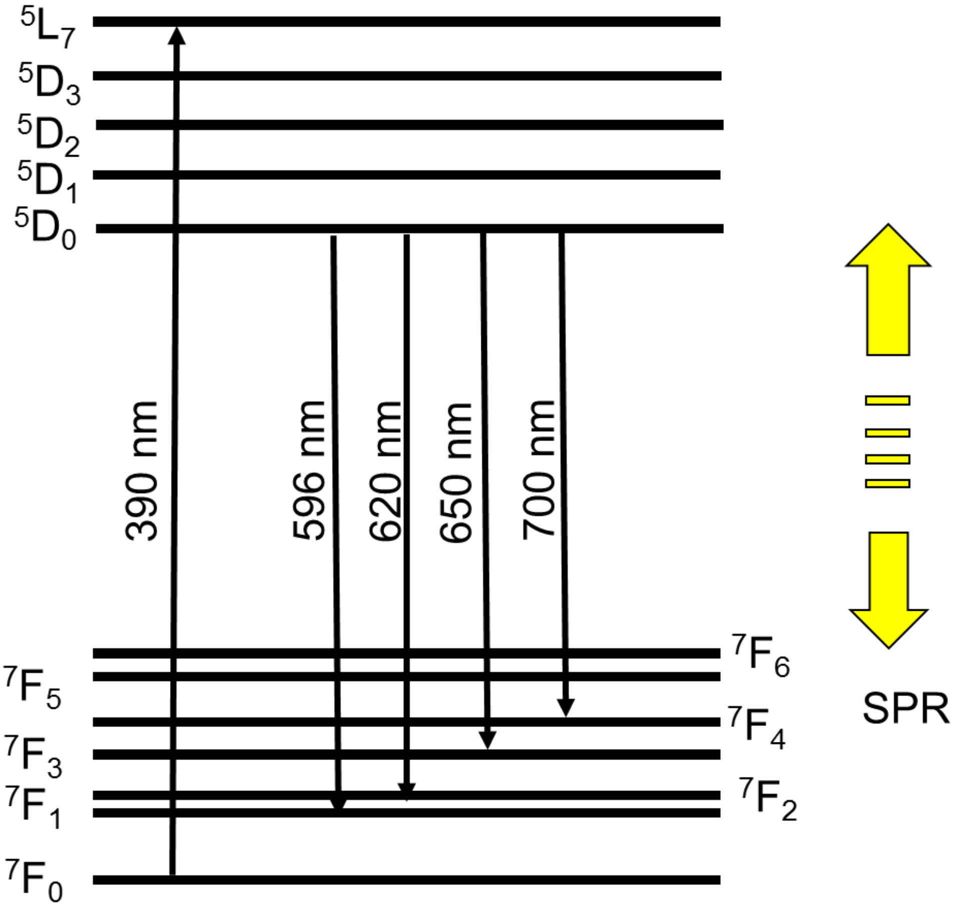

Figure 7.9: Energy level diagram of Eu^{3+} ions showing emission and excitation transitions.

7.6.3. Z-scan

The ultrafast response time and strong nonlinear optical properties associated with surface plasmon resonance of metal nanoparticle in glass makes them promising materials for photonic applications [31]. So studying their nonlinear properties is interesting.

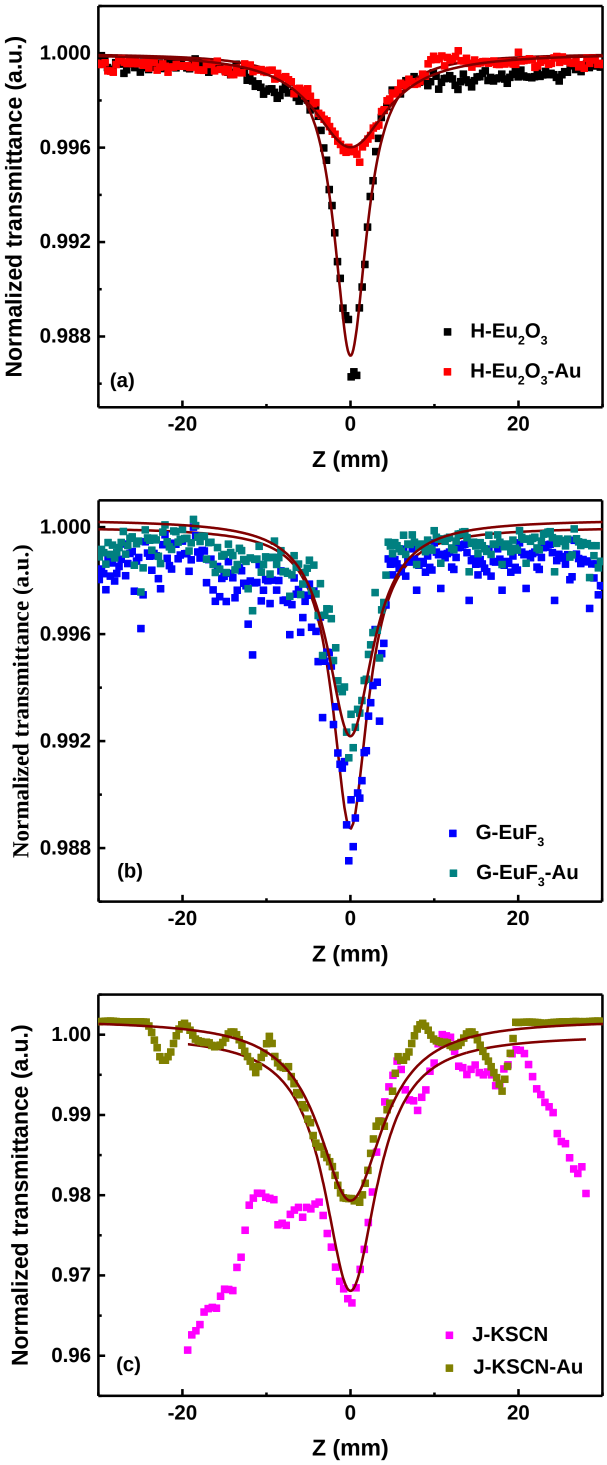

Figure 7.10: Z-scan OA data for (a) H-Eu_2O_3-Au, (b) G-EuF_3-Au and (c) J-KSCN-Au. Solid line and square dots represent theoretically fitted curve and experimental data, respectively.

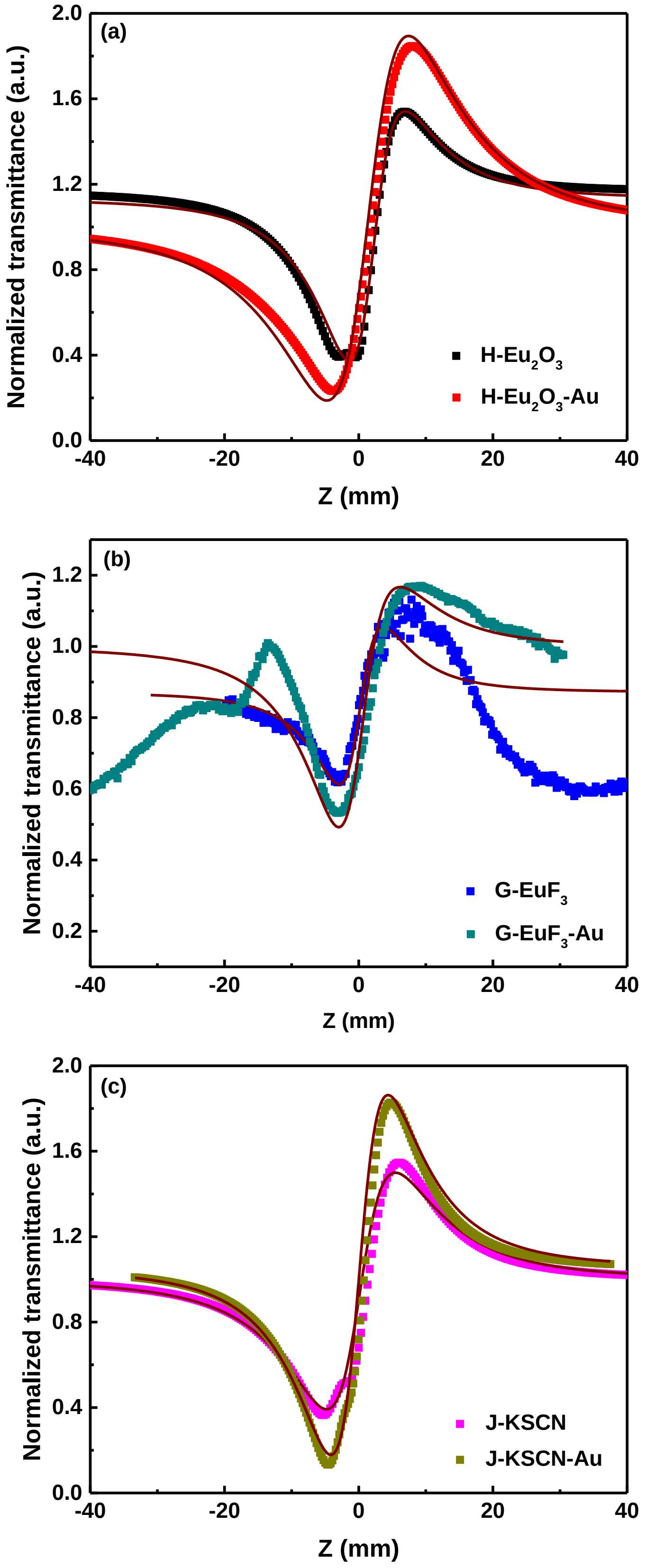

Figure 7.11: Z-scan CA data for (a) H-Eu_2O_3-Au, (b) G-EuF_3-Au and (c) J-KSCN-Au. Solid lines represent theoretical fits to the experimental data (square dots).

Figs. 7.10 (a), (b) and (c) shows the OA Z-scan signatures for AuNP dispersed glasses containing Eu_2O_3, EuF_3 and KSCN as stabilizers along with their corresponding base glass, respectively taken at input peak intensity 14.38 W/m^2. As the sample proceeds towards the focal point, pump intensity is increased and a gradual decrease in the transmittance is observed due to 2PA. Nonlinear absorption coefficient (β_{eff}) have been obtained by fitting the experimental OA Z-scan data using Eqn. (3.6). It can be clearly observed that the sample without AuNPs are also showing nonlinear absorption which is attributed to the presence of bismuth in the glass [32,33]. For both interband and intraband transitions in optical materials, the electron in the ground state absorbs one photon and gets to excited state. This process can result in SA when excited state saturates. On the other hand, when the electron in the ground state absorbs simultaneously two photons and is excited to the higher state, this process is called 2PA. At sufficiently lower input intensity, the optical limiting property of the glass can have contributions from SA whereas at higher input intensity the contribution is from 2PA [34]. Moreover, the experimental data fits well with Eq. (3.6) as shown in Fig. 9. The decrease in β_{eff} (Table. 7.3) value with the addition of AuNPs suggests that AuNPs are possibly contributing to the nonlinear absorption by forming non-bridging oxygens [35].

Figs. 7.11 (a), (b) and (c) display the CA Z-scan data (points) and fits (line) for AuNPs doped glasses containing Eu_2O_3, EuF_3 and KSCN as stabilizers, respectively along with their corresponding base glass. The fits are based on Eqn. (3.7) and the calculated values of third order refractive indices for all the samples are presented in Table 7.3. Based upon real and virtual states involved in the photo excitation, both resonant and non-resonant effects can contribute to the optical nonlinearity in inorganic glasses. The hyper-polarizability of the constituting materials present in the glass composition that leads to the existence of positive type of nonlinearity even in the undoped glass. Heavy metal ions, transition-metal ions, bridging and non-bridging oxygens fall into this category of constituents [36]. Further Zhu et. al. [36] demonstrated that the presence of heavy metal oxide in the glass composition results in high nonlinear refractive index due to unusual hyper-polarizability of non-bonding lone pair electrons of heavy metal ion and effective screening of outer electrons from the nucleus under the influence of applied optical electric field. Therefore, the observed high nonlinear refractive index of the undoped glass sample is attributed to the large hyper-polarizability of non-bonding lone pair electrons of both $Eu^{3+}$and Bi^{3+} or CN^- and Bi^{3+}. The CA profile at different input intensities shows "valley-peak" type of structure that approves the existence of self-focusing type of third order nonlinearity. The increase in nonlinearity has been observed for the samples

H-Eu_2O_3-Au and J-KSCN-Au (Table 7.3) which again supports the formation of non-bridging oxygens with the addition of AuNPs. Moreover, error in the fits can be seen from Fig. 7.10 and 7.11 that is attributed to the non-uniformity of the glass sample [37]. From the application point of view, synthesised glasses are promising materials for ultrafast optical switching in optical fibre communication system.

Table 7.3: The third-order nonlinear optical parameters of the glass at 800 nm.

Sample	**β (m/W)**	**n_2 (m^2/W)**	**$\lvert\chi^{(3)}\rvert$ (esu)**	**F**	**W**	**T**
H-Eu_2O_3	9.1×10^{-13}	3.3×10^{-18}	4.9×10^{-12}	2.2	>1	0.22
H-Eu_2O_3-Au	1.0×10^{-14}	4.7×10^{-18}	6.9×10^{-12}	293.7	>1	<0.001
G-EuF_3	2.7×10^{-14}	5.7×10^{-19}	8.3×10^{-13}	13.2	>1	0.04
G-EuF_3-Au	2.8×10^{-14}	2.9×10^{-18}	4.3×10^{-12}	64.7	>1	0.01
J-KSCN	6.4×10^{-13}	3.9×10^{-18}	5.7×10^{-12}	3.8	>1	0.13
J-KSCN-Au	6.7×10^{-13}	5.9×10^{-18}	8.9×10^{-12}	5.5	>1	0.09

References:

1 A. Simo, J. Polte, N. Pfander, U. Vainio, F. Emmerling and K. Rademann, *J. Am. Chem. Soc.*, 2012, **134**, 18824–18833.

2 S. K. Ghoshal, A. Awang, M. R. Sahar and R. Ari, *J. Lumin.*, 2015, **159**, 265–273.

3 L. R. P. Kassab, F. A. Bomfim, J. R. Martinelli, N. U. Wetter, J. J. Neto and C. B. De Araujo, *Appl. Phys. B Lasers Opt.*, 2009, **94**, 239–242.

4 T. Som and B. Karmakar, *J. Appl. Phys.*, 2009, **105**, 013102.

5 M. R. Dousti, M. R. Sahar, S. K. Ghoshal, R. J. Amjad and A. R. Samavati, *J. Mol. Struct.*, 2013, **1035**, 6–12.

6 S. K. Singh, N. K. Giri, D. K. Rai and S. B. Rai, *Solid State Sci.*, 2010, **12**, 1480–1483.

7 L. Reyes, P. Kassab, M. Eiji, C. Taveira, D. Mariano and J. Roberto, *Opt. Mater. (Amst).*, 2011, **33**, 1948–1951.

8 D. Mariano, L. Reyes, P. Kassab, S. R. Lüthi, C. B. De Araújo, S. L. Anderson, M. José and V. Bell, *Appl. Phys. Lett.*, 2007, **90**, 1–3.

9 C. B. De Araujo, D. Silvério, T. Alexandre, A. De Assumpção, L. Reyes, P. Kassab and D. Mariano, *Sci. World J.*, 2013, **385193**, 1–13.

10 Z. Pan, A. Ueda, R. A. Jr, A. Burger, R. Mu and S. H. Morgan, *J. Non. Cryst. Solids*, 2010, **356**, 1097–1101.

11 A. Awang, S. K. Ghoshal, M. R. Sahar, R. Arifin and F. Nawaz, *J. Lumin.*, 2014, **149**, 138–143.

12 R. Kaur, S. Singh and O. P. Pandey, *J. Mol. Struct.*, 2013, **1049**, 386–391.

13 D. Saritha, Y. Markandeya, M. Salagram, M. Vithal, A. K. Singh and G. Bhikshamaiah, *J. Non. Cryst. Solids*, 2008, **354**, 5573–5579.

14 Y. B. Saddeek and M. S. Gaafar, *Mater. Chem. Phys.*, 2009, **115**, 280–286.

15 D. Möncke, D. Ehrt and E. I. Kamitsos, *Phys. Chem. Glas. Eur. J. Glas. Sci. Technol. Part B*, 2013, **54**, 42–51.

16 D. Möncke, D. Ehrt, C. P. E. Varsamis, E. I. Kamitsos and A. G. Kalampounias, *Glas. Technol. Eur. J. Glas. Sci. Technol. Part A*, 2006, **47**, 133–137.

17 H. Doweidar and Y. B. Saddeek, *J. Non. Cryst. Solids*, 2009, **355**, 348–354.

18 Manupriya, K. S. Thind, G. Sharma, V. Rajendran, K. Singh, A. V. G. Devi and S. Aravindan, *Phys. Status Solidi Appl. Mater. Sci.*, 2006, **203**, 2356–2364.

19 S. Baccaro and G. Sharma, *Nucl. Inst. Methods Phys. Res. B*, 2007, **260**, 613–618.

20 A. V Egorysheva, V. D. Volodin and V. M. Skorikov, *Inorg. Mater.*, 2008, **44**, 1261–1265.

21 R. Bitar, G. Agez and M. Mitov, *Soft Matter*, 2011, **7**, 8198.

22 Y.-R. Luo and J. A. Kerr, *CRC Handb. Chem. Phys.*, 2012, **89**, 65–98.

23 H. Basch, *Inorganica Chim. Acta*, 1996, **252**, 265–279.

24 T. V. Bocharova, G. O. Karapetyan, A. M. Mironov, N. O. Tagil’tseva and O. V. Yanush, *Glas. Phys. Chem.*, 2005, **31**, 420–426.

25 A. Le Rouge, H. El Hamzaoui, B. Capoen, R. Bernard, G. Martinelli, C. Cassagne, G. Boudebs, M. Bouazaoui and L. Bigot, *Mater. Res. Express*, 2015, **2**, 1–10.

26 R. Priya and O. P. Pandey, *Vacuum*, 2018, **156**, 283–290.

27 R. Priya and O. P. Pandey, *J. Lumin.*, 2019, **212**, 342–353.

28 R. Bagga, V. Gopal, A. Goel, J. M. F. Ferreira, N. Pal, D. Paul, V. Contini, M. Falconieri and G. Sharma, *Opt. Mater. (Amst).*, 2013, **36**, 198–206.

29 L. R. P. Kassab, D. S. Da Silva, R. De Almeida and C. B. De Araújo, *Appl. Phys. Lett.*, 2009, **94**, 2007–2010.

30 R. de Almeida, D. M. da Silva, L. R. P. Kassab and C. B. de Araújo, *Opt. Commun.*, 2008, **281**, 108–112.

31 S. Qu, Y. Gao, X. Jiang, H. Zeng and Y. Song, *Opt. Commun.*, 2003, **224**, 321–327.

32 R. Xu, S. Zhao, K. Yang, G. Li, T. Li and L. Dechun, *Opt. Express*, 2018, **26**, 8542–8549.

33 X. Yang, W. Xiang, H. Zhao, H. Liu, X. Zhang and X. Liang, *J. Alloys Compd.*, 2011, **509**, 7283–7289.

34 R. Rajaramakrishna, S. Karuthedath, R. V Anavekar and H. Jain, *J. Non. Cryst. Solids*, 2012, **358**, 1667–1672.

35 S. B. Kolavekar, N. H. Ayachit, G. Jagannath, K. NagaKrishnakanth and S. Venugopal Rao, *Opt. Mater. (Amst).*, 2018, **83**, 34–42.

36 X. H. Zhu, Q. Li, N. B. Ming and Z. Y. Meng, *Appl. Phys. Lett.*, 1997, **71**, 867–869.

37 B. S. Kalanoor, L. Gouda, R. Gottesman, S. Tirosh, E. Haltzi, A. Zaban and Y. R. Tischler, *ACS Photonics*, 2016, **3**, 361–370.

CHAPTER 8 Conclusions and future scope

Overview

In this chapter, summary of results obtained from structural, morphological, physical, thermal and optical studies of AuNPs dispersed glasses are presented. The effect of various factors i.e. method of preparation, amount and size of AuNPs, matrix composition, presence of refractory material and stabilizer on optical efficiency of the glass is compared. At the end, suggestions for future work are given on the basis of results obtained.

8.1. Conclusions

Glasses containing metallic nanoparticles are promising candidates for several optical and data storage devices. Moreover, their exceptional thermal stability makes them highly suitable for fiber drawing and communication applications. Here, in the present work we explores mainly the linear and nonlinear optical behaviour of borate glasses ((x) B_2O_3-(100-x) B_2O_3 (x=30 mol %, 35 mol %, 40 mol %), 40Bi_2O_3-40B_2O_3-20SiO_2) dispersed with AuNPs. It has been observed that the optical behaviour of the glass is an intrinsic function of fabrication rout, amount and size of AuNPs, glass composition and stability of AuNPs. The major findings of the present study are as follows.

1. Among various methods (ion exchange, vapour deposition, laser irradiation, ion implantation, electrochemical deposition, sol-gel etc.) used for the production of metal nanoparticles dispersed glasses where post treatment is required, direct incorporation is an efficient and economical method. No subsequent heat treatment is required that reduces the chance of crystallization inside the glass and hence enhances the optical efficiency. The homogeneous distribution of AuNPs can be simply achieved by mixing it with the starting precursors prior to melt-quench (RTM) as compared to DCM and SM.
2. Initial set of experiments depicted the splitting of AuNPs into Au^0 atoms during melting resulting in the loss of NPs due to evaporation and oxidation. These Au^0 atoms further combined together to form coagulated AuNPs which were bigger in size as compared to initial NPs taken as ingredient. The transformation has also been represented in following equation;

$$AuNPs \xrightarrow{melting} Au^0\ atom \xrightarrow{annealing} AuNPs$$

Further, the enhanced coagulation and observed loss of AuNPs is controlled with the help of varying their size and concentration of initially added AuNPs.

3. Increase in Bi_2O_3 concentration from 30 to 40 mol% results in formation of non-bridging oxygens in the glass matrix and hence reduces the glass transition temperature. This reduced glass transition temperature supports the coagulation of Au^0 resulting to the formation of larger AuNPs.
4. Introduction of SiO_2 in glass matrix successfully reduced the loss of AuNPs while melting the glass. Presence of SiO_2 increased the particle density inside the glass with compromised clustering of AuNPs.
5. Among the three stabilizers (Eu_2O_3, EuF_3 and potassium thiocynate (KSCN)), Eu_2O_3 and KSCN effectively prevents clustering by forming a protective layer around the

nanoparticles. Whereas, addition of KSCN did not provide sufficient particle density inside the glassy matrix as compared to Eu_2O_3. While, EuF_3 exhibited higher degree of clustering of NPs as compared to other stabilising agents.

6. 2-fold enhancement in luminescence intensity is observed in the vicinity of AuNPs in glass containing Eu_2O_3. This enhancement is associated with the induced local field around the Eu^{3+} ions in the vicinity of AuNPs and the energy transfer among AuNPs and Eu^{3+} ions. No such luminescence enhancement is observed in glass containing EuF_3 even after the addition of AuNPs due to clustering of NPs.

7. Glasses containing homogeneously distributed AuNPs, shows high third order nonlinearity and low nonlinear absorption. This nonlinear behaviour of the glass further depends upon the amount and size of AuNPs. The hyper-polarizability of the Bi ions present in the glass composition led to the existence of high nonlinearity even in the undoped glasses that has further been increased with the increase in the amount and size of nanoparticles inside the glass. The increase in nonlinear refractive index with the addition of gold is attributed to the enhanced local electric field due to surface plasmon resonances. Whereas, the decrease in absorption in vicinity of AuNPs is a result of suppression of the electronic transitions in Bi ions. The order of $\chi^{(3)}$ value remains same for all the prepared glass samples that could be due to the presence of highly polarizable Bi ions and NBOs in the glass itself. Glasses containing AuNPs along with the stabilizers are found to show highest nonlinearity among all the prepared glasses. Table 8.1 summarises the obtained nonlinear parameters for the prepared glasses.

Table 8.1. Comparative data of nonlinear parameters obtained for different glass systems.

Sample	**β (m/W)**	**n_2 (m^2/W)**	**$\lvert\chi^{(3)}\rvert$ (esu)**	**F**	**W**	**T**
BiB	4.3×10^{-12}	9.2×10^{-19}	1.1×10^{-12}	0.13	>1	3.77
BiB8	0.9×10^{-12}	1.8×10^{-18}	2.0×10^{-12}	1.11	>1	0.44
BiB0	5.2×10^{-12}	1.0×10^{-18}	1.5×10^{-12}	0.13	>1	3.94
BiB10	3.8×10^{-12}	2.0×10^{-18}	2.9×10^{-12}	0.33	>1	1.52
BiB0’	7.8×10^{-12}	1.9×10^{-18}	2.7×10^{-12}	0.15	>1	3.35
BiB10’	4.8×10^{-12}	2.5×10^{-18}	3.7×10^{-12}	0.33	>1	1.50
BiBSi	2.0×10^{-13}	1.7×10^{-18}	2.5×10^{-12}	5.4	>1	0.09
BiBSi10	1.4×10^{-13}	2.0×10^{-18}	2.9×10^{-12}	8.7	>1	0.06
BiBSi40	8.5×10^{-14}	2.9×10^{-18}	4.2×10^{-12}	21.2	>1	0.02
BiBSi100	5.6×10^{-14}	3.2×10^{-18}	4.8×10^{-12}	36.7	>1	0.01
H-Eu_2O_3	9.1×10^{-13}	3.3×10^{-18}	4.9×10^{-12}	2.2	>1	0.22
H-Eu_2O_3-Au	1.0×10^{-14}	4.7×10^{-18}	6.9×10^{-12}	293.7	>1	<0.001
G-EuF_3	2.7×10^{-14}	5.7×10^{-19}	8.3×10^{-13}	13.2	>1	0.04
G-EuF_3-Au	2.8×10^{-14}	2.9×10^{-18}	4.3×10^{-12}	64.7	>1	0.01
J-KSCN	6.4×10^{-13}	3.9×10^{-18}	5.7×10^{-12}	3.8	>1	0.13
J-KSCN-Au	6.7×10^{-13}	5.9×10^{-18}	8.9×10^{-12}	5.5	>1	0.09

8.2. Future Scope

In the present work, homogeneous dispersion, control over size and stability of AuNPs in borate glasses is successfully achieved to enhance the non-linear optical behavior. If glasses containing metallic nanoparticles introduced in predefined patterns are available, they could be used in optics and material science for light manipulation–generation and control. Patterned glasses can be a lot of interest for both basic physics as well as applications. Apart from nonlinear behavior in non-resonant region, prepared glasses can be explored in resonant region for more real time applications. In addition, further study can be carried out on prepared glasses for application in terahertz optical devices exploiting the high refractive index of bismuth-borate and -borosilicate glass in conjunction with the refractive index control induced by AuNPs dispersion. Also, analyzing the behavior of AuNPs in a glass having larger Bi content or another dopant like lithium would be helpful in determining the effect of NBO's on nonlinear behavior. The amorphous nature of studied glass even after the addition of AuNPs makes them best choice for fiber drawing.